Charge transport and molecular diffusion within self-assembled nanostructures

by

Govinda Ghimire

B.S., Tribhuvan University, 2006
M.S., Tribhuvan University, 2008

AN ABSTRACT OF A DISSERTATION

submitted in partial fulfillment of the requirements for the degree

DOCTOR OF PHILOSOPHY

Department of Chemistry
College of Arts and Sciences

KANSAS STATE UNIVERSITY
Manhattan, Kansas

2019

Abstract

This dissertation describes charge transport behavior within redox-active block copolymer (BCP) microdomains and the diffusion behavior of charged dye molecules within self-assembled bolaamphiphilic organic nanotubes (ONTs) of different surface charge and inner diameters. In-depth understanding of the charge transport efficiency within redox-active microdomains in electrode-supported BCP thin films is crucial for their various electrochemical applications. Similarly, understanding of the diffusion behavior of differently charged dye molecules in ONTs will help design nanotubular materials better suited for drug-delivery and adsorbent applications.

In the former study, polystyrene-*block*-poly(2-(acryloyloxy) ethylferrocenecarboxylate) (PS-*b*-PAEFc) of different PAEFc volume fractions (f_{PAEFc}) was used as redox-active BCPs. The AFM images of PA-*b*-PAEFc thin films suggested that the morphology of PAEFc microdomains was dependent of the volume fraction. A series of electrochemical data revealed that thin films based on large f_{PAEFc}, which were expected to yield lamellar and cylindrical microdomains, afforded redox-active microdomains that extended from the underlying electrode to the film–solution interface. In addition, charge transport efficiency, which was represented by apparent diffusion coefficient, within the ferrocene-containing microdomains was similar irrespective of f_{PAEFc}, reflecting the similar concentration and dynamic properties of the redox-active moieties. Furthermore, the charge transport was observed in an acetonitrile solution but not in an ethanol solution, indicating that the thin films needed be swollen for redox-mediated charge propagation across the ferrocene moieties in the microdomains. Interestingly, the thin films rendered redox-active in the ethanol solution upon applying an oxidative potential in the acetonitrile solution, possibly due to the migration of electrolyte ions into the films, albeit with lower charge transport efficiency. The "activated" gold-supported PA-*b*-PAEFc thin films were applicable as

electrochemically responsive heterogenous catalysts for Michael addition reaction between a β-dicarbonyl compound and an enone in an ethanol solution. Importantly, the efficiency of the catalytic reaction could be regulated by the potential application, and its selectivity reflected the permeability of the reactants through the thin films.

In the latter study, the diffusion behavior of differently charged fluorescent molecules within individual ONTs was systematically measured using imaging fluorescence correlation spectroscopy (imaging FCS) at different pH and ionic strength conditions. The ONTs with the inner diameters of 10 or 20 nm, which were self-assembled from asymmetrical bolaamphiphiles, had glucose moieties on their outer surfaces, and amine or carboxyl groups on their inner surfaces. Imaging FCS could be used to measure the diffusion of dye molecules that interacted with nanotube inner surfaces. Indeed, diffusion coefficients of dye molecules within the ONTs were much smaller than those in an aqueous solution and were strongly controlled by electrostatic interactions with the amine or carboxyl groups on the inner surfaces as shown by the pH dependence of the diffusion coefficients. In contrast, effects of ionic strength were relatively minor, suggesting the involvement of non-coulombic interactions in the molecular diffusion. Importantly, imaging FCS data revealed that the diffusion coefficients were independent of ONT length, implying that the properties of the ONTs were uniform in terms of solute loading and release.

Charge transport and molecular diffusion within self-assembled nanostructures

by

Govinda Ghimire

B.S., Tribhuvan University, 2006
M.S., Tribhuvan University, 2008

A DISSERTATION

submitted in partial fulfillment of the requirements for the degree

DOCTOR OF PHILOSOPHY

Department of Chemistry
College of Arts and Sciences

KANSAS STATE UNIVERSITY
Manhattan, Kansas

2019

Approved by:

Major Professor
Dr. Takashi Ito

Copyright

Abstract

This dissertation describes charge transport behavior within redox-active block copolymer (BCP) microdomains and the diffusion behavior of charged dye molecules within self-assembled bolaamphiphilic organic nanotubes (ONTs) of different surface charge and inner diameters. In-depth understanding of the charge transport efficiency within redox-active microdomains in electrode-supported BCP thin films is crucial for their various electrochemical applications. Similarly, understanding of the diffusion behavior of differently charged dye molecules in ONTs will help design nanotubular materials better suited for drug-delivery and adsorbent applications.

In the former study, polystyrene-*block*-poly(2-(acryloyloxy) ethylferrocenecarboxylate) (PS-*b*-PAEFc) of different PAEFc volume fractions (f_{PAEFc}) was used as redox-active BCPs. The AFM images of PA-*b*-PAEFc thin films suggested that the morphology of PAEFc microdomains was dependent of the volume fraction. A series of electrochemical data revealed that thin films based on large f_{PAEFc}, which were expected to yield lamellar and cylindrical microdomains, afforded redox-active microdomains that extended from the underlying electrode to the film–solution interface. In addition, charge transport efficiency, which was represented by apparent diffusion coefficient, within the ferrocene-containing microdomains was similar irrespective of f_{PAEFc}, reflecting the similar concentration and dynamic properties of the redox-active moieties. Furthermore, the charge transport was observed in an acetonitrile solution but not in an ethanol solution, indicating that the thin films needed be swollen for redox-mediated charge propagation across the ferrocene moieties in the microdomains. Interestingly, the thin films rendered redox-active in the ethanol solution upon applying an oxidative potential in the acetonitrile solution, possibly due to the migration of electrolyte ions into the films, albeit with lower charge transport efficiency. The "activated" gold-supported PA-*b*-PAEFc thin films were applicable as

electrochemically responsive heterogenous catalysts for Michael addition reaction between a β-dicarbonyl compound and an enone in an ethanol solution. Importantly, the efficiency of the catalytic reaction could be regulated by the potential application, and its selectivity reflected the permeability of the reactants through the thin films.

In the latter study, the diffusion behavior of differently charged fluorescent molecules within individual ONTs was systematically measured using imaging fluorescence correlation spectroscopy (imaging FCS) at different pH and ionic strength conditions. The ONTs with the inner diameters of 10 or 20 nm, which were self-assembled from asymmetrical bolaamphiphiles, had glucose moieties on their outer surfaces, and amine or carboxyl groups on their inner surfaces. Imaging FCS could be used to measure the diffusion of dye molecules that interacted with nanotube inner surfaces. Indeed, diffusion coefficients of dye molecules within the ONTs were much smaller than those in an aqueous solution and were strongly controlled by electrostatic interactions with the amine or carboxyl groups on the inner surfaces as shown by the pH dependence of the diffusion coefficients. In contrast, effects of ionic strength were relatively minor, suggesting the involvement of non-coulombic interactions in the molecular diffusion. Importantly, imaging FCS data revealed that the diffusion coefficients were independent of ONT length, implying that the properties of the ONTs were uniform in terms of solute loading and release.

Table of Contents

List of Figures

List of Tables

Acknowledgements

To my major professor and Ph.D. adviser Dr. Takashi Ito, without his continuous guidance and encouragement, this would not be possible. His unbreakable enthusiasm and patience while mentoring me with the instrumentation, experiments and data analyses cannot be expressed in words. He was always there to correct me when I was wrong, work long hours to revise my drafts of presentations, seminar write-ups and publication manuscripts. Thank you for everything!

To Dr. Daniel A. Higgins for his precious guidance and suggestions during the microscopy experiments and data analyses. I feel obliged for getting an opportunity to use his microscopic assembly and software programs in his laboratory. I also thank him for troubleshooting the microscope at times when I was unable to do it.

I am very thankful to my Ph.D. committee members Drs. Bret Flanders, Tendai Gadzikwa and Jun Li for valuable suggestions during the preliminary exams and final defense. I also thank Dr. Behrooz Mirafzal for being my outside chair in the final defense presentation. I specially appreciate Dr. Li for his suggestion on reference electrode in my electrochemistry research in **Chapter 3**. I thank Dr. Flanders for his suggestions on electrochemistry and AFM experiments. I thank Dr. Gadzikwa for willing to be my committee member at a difficult time.

I would also thank Drs. Naohiro Kameta, Mitsutoshi Masuda and Yi Yi for letting me use the material they synthesized. Besides that, their suggestions and guidance during the relevant research and manuscript preparation were quite valuable. I thank Department of Chemistry and Nanoscale Characterization Facility, Indiana University for supporting the synthesis of PS-*b*-PAEFc. I can never stop thanking Ms. Shinobu Nagasaka for being a helpful lab-mate and preparing cover-slip dispersed ONT samples for me experiments in **Chapters 5** and **6**. Also, I

am very thankful to my research collaborators Dr. Lane A. Baker and Maksymilian A. Derylo for their preliminary data that initiated **Chapter 3**. I thank James Hilfiker at J.A. Woolam for his guidance with the analysis of spectroscopic ellipsometry data.

I had wonderful lab-mates as fellow friends in Ito and Higgins group. Dr. Khanh-Hoa Tran-Ba and Dr. Hao Xu were amazing senior lab-mates. I appreciate Dr. Tran-Ba for mentoring me with the usage and sample preparation for AFM and ellipsometry, and Dr. Xu for teaching me how to prepare dye doped ONT samples and use them on the wide-field microscope for the acquisition of imaging FCS data. Herman Coceancigh is greatly acknowledged for helping with the NMR data collection used in **Chapter 4**, for all your MS Excel tips and discussion about our research, programming, and soccer. Dol Raj Sapkota, Zeinab Harandizadeh and Judith Bautista were amazing friends. They were always there when I needed someone to talk to or ask a question.

I am also very thankful for the opportunity to work with undergraduate students. I thank Trevor Elwell-Cuddy for his help during the AFM measurements, and Roberto Espinoza, Rebecca Leuschen and Mikaela Moore for collecting data and running analyses used in **Chapter 5** and **6**.

I also thank Drs. Duy Hua and Man Zhang for their help with NMR measurements used in **Chapter 4**. I acknowledge U.S. Department of Energy for funding the research projects.

I express my solemn gratitude to all the staff members in the chemistry department. I greatly appreciate Michael Hinton, a terrific laboratory coordinator, for suggesting me during the times I was a TA for CHM 201. I thank Jim Hodgson, Ron Jackson and Tobe Eggers, awesome technicians, for their unwavering support when I needed some glassware blown or white-board repaired or potentiostat fixed. I must thank Mary Dooley for all her prompt suggestions whether

be it before I came to the US or be it afterwards. She was always so kind and supportive. I thank Kimberly Ross a lot for assigning me the seminar rooms when needed. They all will always be remembered.

Lastly, I would like to thank my family and friends for their unbreakable support and love. The Nepalese Students Community (NSA) at Manhattan, KS made this city a home far away from home. My wife Asim and daughter Anzie, their contribution in my studies cannot me measured or quantified. Everything I have achieved or learned in the last years would have been impossible without them. What I am today is because of them. Thank you both.

Dedication

To my proud parents Keshav and Lila, my loving wife Asim, and my daughter Anzie.

Acronyms and Definitions

AFM	Atomic force microscopy
ATRP	Atom transfer radical polymerization
BCP	Block copolymer
CC	Chronocoulometry
CCD	Charge coupled device
COOH-ONTs	Organic nanotubes with carboxylate surface group
CV	Cyclic voltammetry
DCLP	Dichroic long-pass
E2OC	Ethyl 2-oxocyclopentanecarboxylate
emCCD	Electron multiplying charge coupled device
ERHC	Electrochemically responsive heterogenous catalysts
EtOH	Ethanol
FCS	Fluorescence correlation spectroscopy
FRAP	Fluorescence recovery after photobleaching
FRET	Fluorescence resonance energy transfer
GCE	Glassy carbon electrode
GFP	Green fluorescent protein
GOx	Glucose oxidase
HPLC	High performance liquid chromatography
Imaging FCS	Imaging fluorescence correlation spectroscopy
MeCN	Methyl cyanide or Acetonitrile
MLM	Monolayer lipid membrane

MVK	Methyl vinyl ketone
$NaPF_6$	Sodium hexafluorophosphate
NH_2-ONTs	Organic nanotubes with amine surface group
NMR	Nuclear magnetic resonance
NR	Nile Red
ONT	Organic nanotubes
PAEFc	Poly(2-(acryloyloxy)ethyl ferrocenecarboxylate)
PB	Polybutadiene
PBS	Phosphate buffered saline
PDAMS	Poly[(4-diethylaminomethyl)styrene]
PDMS	Poly(dimethylsiloxane)
PFcMA	Poly(ferrocenyl methacrylate)
PFDMS	Poly(ferrocenyldimethylsilane
PFMMA	Poly(ferrocenyl methylmethacrylate)
PFS	Poly(ferrocenylsilane)
PGMA	Poly(glycidyl methacrylate)
PI	Polyisoprene
PMMA	Poly(methyl methacrylate)
PS	Polystyrene
PVEA	Poly(4-vinylbenzyl diethylamine)
PVFc	Polyvinyl ferrocene
RB	Rhodamine B
SAM	Self-assembled monolayers

SE	Spectroscopic ellipsometry
SEM	Scanning electron microscopy
SRB	Sulforhodamine B
$TBAPF_6$	Tetrabutylammonium hexafluorophosphate
TEM	Transmission electron microscopy
TGF	Transforming Growth Factor
TIRF	Total internal reflection fluorescence
TMS	Tetramethyl silane
trans-PBO	*trans*-4-Phenyl-3-buten-2-one
UV-Vis	Ultraviolet-visible
XRD	X-ray diffraction

Chapter 1 - Self-Assembled Nanostructures

We are all surrounded by living and non-living things. Non-living things are composed of metals, ceramics, biological materials, polymers, and composites. Biological materials are substances that originate from living bodies like plants or animals while things like metals, ceramics, and composites existed on earth since millions of years and have been modified for useful applications. Polymers on the other hand, can be both natural and laboratory synthesized. For example, rubber is a natural polymer which is harvested from trees as latex. It is modified and used for various applications like tires and tubes, which have been a crucial part of our daily lives. Similarly, polymers can be synthesized in the laboratory using some starting materials derived from petroleum oil. For example, polyethylene is a laboratory product that has applications ranging from bags and bottles to construction and electronics. Among the above-mentioned materials, we are more interested in some specific polymers and biomaterials because of their potential applications in science and technology.

1.1 Polymers

Polymers are formed by covalent combination of smaller units called monomers. So many polymeric materials have been produced and used so that our life today is difficult to imagine without them. Clothing, utensils, stationery, or automobiles, all use polymers in some way.[1] As reported in 2009, more than 260 million tons of plastics are produced each year world-wide.[2] Polymeric materials can be divided into sub-classes based on their structures, properties and functions. Homopolymers are made of single repeating monomers in the chain. A generic example of homopolymer is given in **Figure 1.1a**, which consists of similar repeating monomeric units.[3] Polyethylene is an example of homopolymer. The other class of polymer is known as copolymers, which are composed of multiple monomers. Examples of copolymers are

shown in **Figure 1.1b-c**, in which a statistic copolymer has a sequential pattern of monomeric units while a random copolymer does not have it. Another class of polymer is called block copolymer (BCP), in which multiple blocks of homopolymers are connected covalently like linear diblock and triblock copolymers as shown in **Figure 1.1d**. Polymers are also further classified based on their stability to heat, properties of electrical conductivity, crystallinity and redox properties. In relevance to this dissertation, we are more interested in redox polymers.

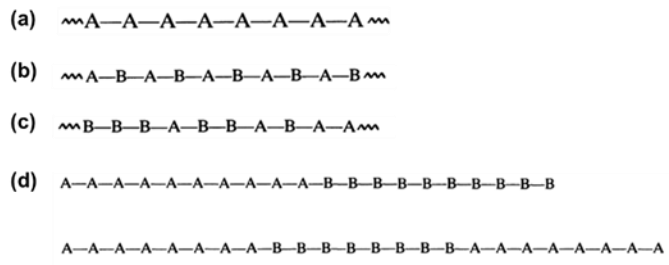

Figure 1.1. (a) Homopolymer, **(b)** statistical copolymer, **(c)** random copolymer, and **(d)** block copolymer. Reproduced with permission from reference (3). 2011, Copyright: CRC Press.

1.1 Redox Polymers[22]

The term "redox" process represents the oxidation and reduction processes of a molecule or an ion, which involve the loss and gain of one or more electrons, respectively. Polymers that are capable of losing or gaining electrons in response to external stimuli are referred to as redox polymers. Such reactions can take place anywhere in the polymer i.e. main chain or in the side groups, and this may be associated with other ionic, electrical, mechanical, optical, and chemical properties of the material.[4] Redox polymers are used for several applications like batteries, electrochromic devices, dye-sensitized solar cells, biofuel cells, biosensors, actuators and drug-delivery devices, as shown in **Figure 1.2**. These polymers can be homopolymers or copolymers, and they all have some advantages and dis-advantages. Applicability of all such redox polymers is determined by their electrochemical stability and their charge transport properties. These polymers are often deposited on electrodes as thin films to investigate the charge transport

properties. For example, electrodes modified homopolymer thin films like polyvinylferrocence (PVFc) afford apparent diffusion coefficient, D_{ap}, representing the charge transport efficiency, of 0.1 $\mu m^2/s$.[5,6] This D_{ap} value is three orders of magnitude smaller than that for freely diffusing redox species in solution. Interestingly these films showed much better electrochemical stability.[5,6] Redox homopolymers and random copolymers may possess some nanoscale structures within their films to trigger their functions. Unfortunately, sizes and morphologies of these nanostructures, if existed, are polydisperse and ununiform. In contrast, redox BCPs are expected to provide predictable or tunable uniform nanostructures of dimensions 5 – 100 nm. These nanostructures are self-assembled and can be controlled by adjusting the incompatibility or molecular weights of the monomer blocks.

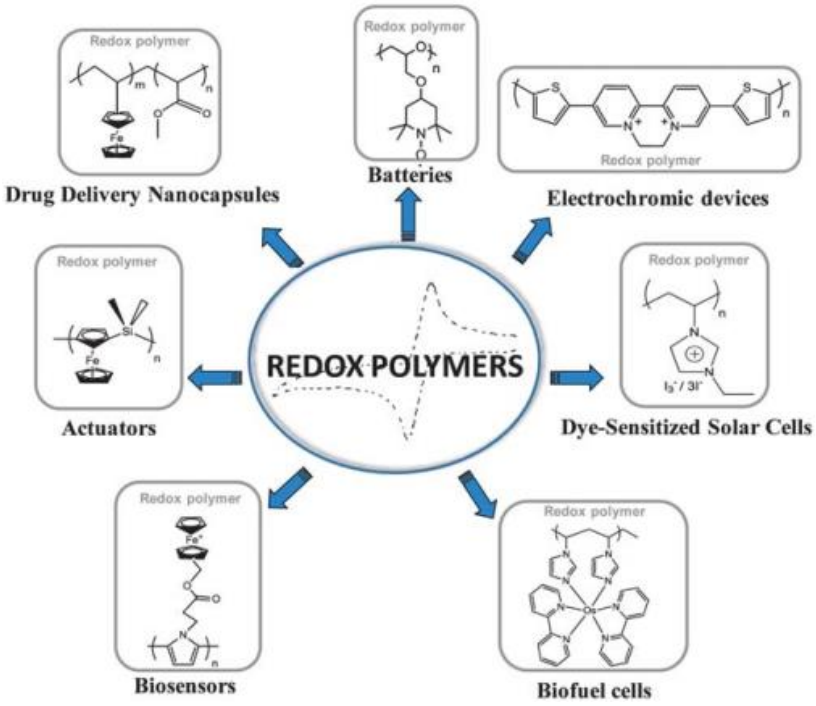

Figure 1.2. Chemical structures of redox polymers showing respective applications. Published with permission from reference (4). 2013, Copyright: Royal Society of Chemistry.

1.1.2 Microphase Separated Redox Block Copolymers (BCPs)

BCPs consist of two or more chemically different blocks of polymer chains that are bound covalently.[7] Based on the number of blocks they possess, they can be classified into di-block (two blocks), tri-block (three blocks) and so on. In addition, the variations of the structural arrangements lead to star-shaped or looped BCPs.[8] Furthermore, they may also be classified based on chemical properties manifested on the blocks, such as conjugated BCPs that possess conjugated groups in one or multiple blocks and redox BCPs containing redox active moieties in one or multiple blocks. Here, we focus on redox diblock copolymers with ferrocene moieties in the side chain.

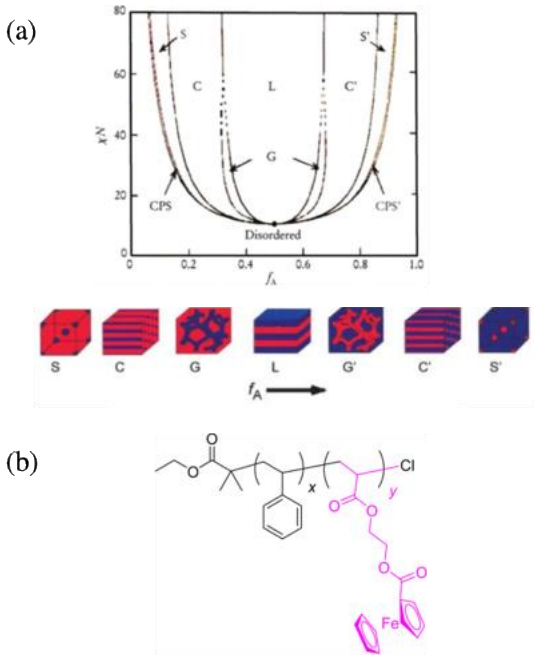

Figure 1.3. (a) Theoretical phase diagram of block copolymers as calculated from mean-field methods and resulting microdomain morphologies of a linear BCP: spheres (S, S'), cylinder (C, C'), gyroid (G, G') and lamellar (L). **(b)** Chemical structure of PS-*b*-PAEFc showing scaffold forming non-redox-active PS in black and redox-active PAEFc in pink. Adapted with permission from Ref (9) and (33). Copyright: 1999 American Institute of Physics, 2015 American Chemical Society.

Microphase separation of diblock copolymers leads to the formation of uniform periodic nanostructures (5 – 100 nm) that arises from the thermodynamic incompatibility of respective blocks. The resulting nanostructures are called microdomains, which are much smaller than

structures obtained via macrophase separation of oil and water in their mixture. Myriads of investigations were carried out on BCP microphase separation, and theories have been established to accurately predict experimental results. For a linear diblock copolymer, the morphology of microdomains under thermodynamic equilibrium can be lamellar (L), gyroid (G, G'), cylindrical (C, C') or spherical (S, S'), as depicted by a phase diagram shown in **Figure 1.3a**.[9,10] The phase diagram suggests that microdomain morphologies are dependent on the volume fraction of block A (f_A), polymerization degree (N) and chemical incompatibility represented by Flory-Huggins parameter (χ). Under favorable χN, a diblock copolymer with f_A of 0.1 – 0.2 affords spherical microdomains which are mostly buried inside the scaffold forming block, one with f_A of 0.3 – 0.4 gives cylindrical nanostructures, and one with f_A of 0.4 – 0.5 offers either gyroid or lamellar structures depending upon the level of χN parameters. The phase diagram provides a means to design diblock copolymers that afford desired microdomain morphologies suitable for target applications.

Microdomain morphologies in BCP thin films on planar substrates are widely studied. Uniformity of the dimensions and periodicity of microdomains can be improved upon annealing processes. Their thickness is often measured using spectroscopic ellipsometry and profilometry, and the nanoscale morphologies are observed using imaging techniques such as AFM, SEM and TEM. Chapters 3 and 4 in this dissertation discuss morphologies and electrochemical properties of gold-supported thin films of a redox BCP, polystyrene-*block*-poly(2-(acryloyloxy) ethylferrocenecarboxylate (PS-*b*-PAEFc, **Figure 1.3b**). PS-*b*-PAEFc has redox-active ferrocene moieties in the side chain. It is known that BCPs with redox moieties in the side chain often have higher glass transition temperature and less favorable for microphase separation. However,

several redox BCPs, including PS-*b*-PAEFc, exhibit microphase separation to give redox-active microdomains.[11-12]

Redox BCPs used for fabrication of electrode-supported thin films are summarized in **Figure 1.4**, where green and black colors indicate the redox-active and scaffold forming blocks, respectively.[22] Redox moieties in these BCPs can be covalently linked to the mainchain or sidechain and play a key role in charge transport across thin redox BCP films on the basis of electron hopping. Thin redox BCP films on electrodes could be used as precursors for fabrication of metal oxide nano-catalyst arrays and components in solid-state electronic devices.[13-17] Furthermore, these BCPs were used to prepare micelles or vesicles that could be applied as molecular carriers responsive to redox stimuli.[18,19]

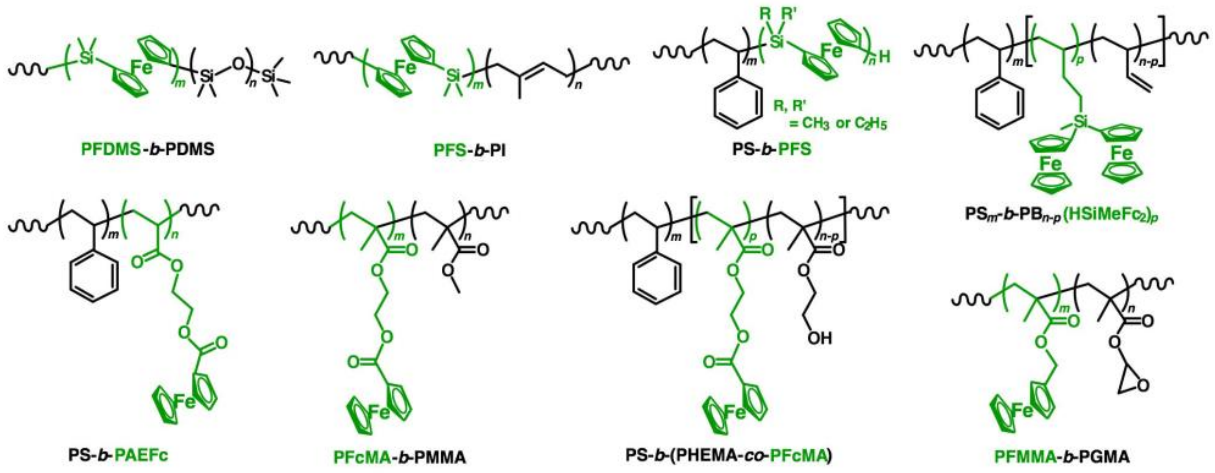

Figure 1.4 Molecular structures of different redox BCPs studied in literature. Green and black colors indicate redox-active and scaffold forming blocks, respectively. Produced by permission from reference (22). 2018, Copyright: Wiley Online Library.

1.1.3 Properties of PS-*b*-PAEFc

PS-*b*-PAEFc, which was used in this study, was synthesized by sequential atom transfer radical polymerization (ATRP) by Dr. Yi at Indiana University, Bloomington. The redox-active ferrocene moieties are in the side chain, and thus the main chain should not be cleaved upon their

redox reaction in contrast to BCPs comprising redox moieties in the main chains. PS-*b*-PAEFc with three PAEFc volume fractions (f_{PAEFc}) were synthesized: PS_{154}-*b*-$PAEFc_{51}$ (f_{PAEFc} = 0.47), PS_{154}-*b*-$PAEFc_{26}$ (f_{PAEFc} = 0.30) and PS_{154}-*b*-$PAEFc_{12}$ (f_{PAEFc} = 0.17). The densities of PS (ρ_{PS}) and PAEFc (ρ_{PAEFc}) were assumed to be equal to those of styrene and polyvinylferrocene (1.05 and 1.25 g/cm^3, respectively) for the calculation of f_{PAEFc}. According to the phase diagram of a diblock copolymer (Figure 1.3 (a)), PS-*b*-PAEFc with f_{PAEFc} = 0.47, 0.30 and 0.17 were expected to afford lamellar, cylindrical and spherical PAFEc microdomains, respectively.

1.1.4 Preparation of Electrode-Supported Redox BCP Thin Films

Redox homopolymers immobilized onto electrodes were applied as mediators for enzyme sensors and as electrocatalysts by taking advantage of their charge transport properties.[20,21] However, their films on the electrodes are sometimes unstable due to their detachment induced by their swelling/deswelling associated with the redox processes. Redox BCPs are expected to exhibit improved electrochemical stability owing to the presence of electrochemically inert block(s) that afford the scaffold of the redox-active microdomains. Electrode-supported thin films of redox BCPs are commonly prepared via spin-coating, electrodeposition and drop-casting.[22] In particular spin-coating has been very widely employed because film thickness can be controlled by acceleration speed, spin rate and time, and polymer concentration. Indeed, PS-*b*-PAEFc films used in Chapters 3 and 4 were prepared via spin-coating its toluene solution onto gold-coated silicon substrates. Their thickness was controlled by the concentration of PS-*b*-PAEFc in the range of 20-140 nm. The resulting thin films were characterized using spectroscopic ellipsometry and atomic force microscopy (AFM) prior to electrochemical measurements. Fast solvent evaporation during spin-coating might induce vertical orientation of microdomains reflecting solvent evaporation direction. When necessary, a further annealing

process based on solvent vapor treatment, heating or electric field application is conducted to improve the extent of the microdomain order and orientation.[23,24] Vertically-aligned microdomains that extend across the thin films are best suited for many applications.

1.1.5 Charge Transport within Electrode-Supported Redox BCP Films

To take advantage of redox BCP thin films reliably for applications like sensing or electrocatalysis, it's crucial to understand factors that affect charge transport efficiency through redox-active microdomains. As with redox homopolymer films, charge transport in redox BCP films is based on electron hopping – collisional electron self-exchange reaction between adjacent redox moieties in a redox microdomain. The efficiency of electron hopping is controlled by the concentration of redox moieties, which corresponds to distance between the redox centers, their dynamic properties, their electron transfer rate constant, and also the migration of counter ions from the bulk solution.[25-27] Charge transfer efficiency is assessed by measuring apparent diffusion coefficient (D_{ap}) using cyclic voltammetry (CV) or Chronocoulometry (CC). [28-31] In contrast to the diffusion coefficient of ferrocene molecules in solution (10^{-6} – 10^{-5} cm^2/s), while D_{ap} in polyvinylferrocene (PVFc) thin films is much smaller (10^{-10} – 10^{-9} cm^2/s) due to the restricted motion of the ferrocene moieties and the limited supply of counter ions. For example, D_{ap} was in the order of 10^{-12} cm^2/s in thin films of poly(ferrocenyldimethylsilane)-*block*-poly(dimethylsiloxane) (PFDMS-*b*-PDMS) with PFDMS volume fractions of 2.9 and 9.1%, which likely afforded spherical PFDMS microdomains.[30] This work reported the influences of solvent, but not redox-active microdomain morphology, on D_{ap}. Interestingly, redox BCP thin films were reported to exhibit higher D_{ap} than redox random copolymer films due to the microdomains that provide continuous electron transport pathways. Indeed, Sumi and Anson observed such behavior in thin films of poly[(4-diethylaminomethyl)styrene]-polystyrene-

poly[(4-diethylaminomethyl)styrene] triblock copolymers (PDAMS-PS-PDAM) that incorporated $Fe(CN)_6^{4-}$ in their cationic PDAMS block.[32] Chapters 3 and 4 will quantitatively discuss the effects of microdomain morphology and solvent on D_{ap} for PS-*b*-PAEFc with three different f_{PAEFc}.[33,34]

1.1.6 Applications of Electrode-Supported Redox BCP Films

Electrode-supported films of redox BCPs with uniform and periodic nanostructures have been explored for electrochemical sensing and synthesis, and as tunable functional materials. Faradaic currents from the redox microdomains are measured at the underlying electrode as signals in electrochemical sensing. The control of the potential of the underlying electrode provides a means to switch the oxidation/reduction state of the redox moieties, leading to the control of catalytic reaction and drug capture/release. Redox microdomains play key roles in these electrochemical applications, whereas their scaffolds based on the electrochemically inactive block improve the morphological stability of the films upon the electrochemical processes as compared with redox homopolymer films. These applications require redox-active microdomains with high charge transport efficiency. In addition, many applications need vertically-oriented microdomains with uniform sizes and uniform distribution.

Armada and coworkers were the first to employ redox BCPs for electrochemical enzyme sensors.[35] The BCPs were obtained by random functionalization of the poly(1,2-butadiene) segment of PS-*b*-PB with diferrocenylmethylsilane ($HSiMeFc_2$) units.[35] The authors used their thin films on Pt electrodes for electrochemical mediation in glucose sensors based on glucose oxidase (GOx), though they could not provide any evidences on the formation of microdomains in the films. Lee and coworkers studied the influence of microdomain morphology on the performance of GOx-based glucose sensors.[36] They drop-casted poly(ferrocenylsilane)-*block*-

polyisoprene (PFS-*b*-PI) thin films (100 nm) on carbon electrodes, followed by the crosslinking the PI microdomains with OsO_4 to enhance the stability of the polymer layer. Microdomain morphologies were tuned by adjusting the molecular weights of PFS/PI segments and casting solvent composition. It was found that microdomain morphology gives a significant influence on the sensor performance, as shown by the observation of a larger glucose oxidation current for bicontinuous microdomains in comparison to cylindrical and spherical microdomains.

Label-free electrochemical sensing is another important application of electrode-supported redox BCP films. Yuan et al. reported label-free electrochemical immunosensors based on poly(ferrocenyl methylmethacrylate)-*block*-poly(glycidyl methacrylate) (PFMMA-*b*-PGMA) brushes on gold electrodes.[37] The binding of target analyte TNF-α (tumor necrosis factor) to an antibody attached to the PGMA chain could be detected as a decrease in faradaic currents of ferrocene moieties in PFMMA. In another work by Kim et al., poly(ferrocenyl methacrylate)-*block*-poly(methyl methacrylate) (PFcMA-*b*-PMMA) brushes were used for a similar purpose.[38] Li and coworkers demonstrated a possibility to design label-free electrochemical sensors that could give electrochemical signals based on changes in linker flexibility.[31] They fabricated gold-supported nanoporous thin films from polystyrene-*block*-poly(methyl methacrylate) (PS-*b*-PMMA), and covalently decorated the nanopore surface with ferrocene moieties. They showed higher D_{ap} with increasing the length of an alkyl linker between ferrocene moiety and nanopore surface, which would control the flexibility of the ferrocene moieties. Subsequently, Li and Ito reported the reversible control of the charge propagation efficiency using an inclusion complex formation of ferrocene with *β*-cyclodextrin (*β*-CD) in the ferrocene-decorated, PS-*b*-PMMA-derived nanoporous films.[39] The repeatable reduction and recovery of faradaic currents were

observed by adjusting β-CD concentration and the addition of a competitive guest of β-CD, 1-adamantanol, to the solution, respectively.

Meanwhile, Eloi and coworkers showed electrochemically triggered adsorption of ferritin molecules onto cylindrical redox-active microdomains (20 nm in diameter) in electrode-supported polystyrene-*block*-poly(ferrocenylsilane) (PS-*b*-PFS) thin films.[40] Electrochemical quartz crystal microbalance (E-QCM) and AFM were employed to monitor changes in the mass and surface morphology associated with ferritin adsorption, respectively. It was found that electrochemical oxidation of the ferrocene moieties of the PFS microdomains could successfully trigger irreversible adsorption of biomolecules. Chapter 4 in this dissertation will discuss the application of gold-supported thin PS-*b*-PAEFc films as heterogeneous catalysts for Michael addition reaction.[34]

1.2 Biological Materials[46]

Nucleic acids, proteins, carbohydrates and lipids are biomolecules forming life. DNA and RNA, commonly called nucleic acids, are biopolymers that are responsible for genetic coding of every living organisms. They are composed of sugars, phosphates and nitrogenous base. Proteins are made up of amino acid residues and can be categorized into several types based on their functions. Some of them include antibodies, enzymes, and hormones. They are also responsible for storage (example: ferritin stores iron), transport (example: cytochromes transport electrons) and structural integrity (example: keratin) in any living organisms. Carbohydrates, which exist in the forms of sugar, starch and cellulose, are another class of biological materials that serve for energy production/storage or as the structural components of plant cells. More relevant to this dissertation are lipids that are amphiphilic biomolecules and are another source of energy in a living body. More importantly, lipids can self-assemble into cell membranes and vesicles.

Vesicles involve different functions such as transport of chemical species in biological systems, and thus are examined as drug delivery vehicles. Interestingly, tubular vesicles seem to be more promising for such applications than their spherical counterparts because of their sustained retention in blood plasma and slower release of chemicals from the hollow open ends.[41]

1.2.1 Organic Nanotubes (ONTs)

Hecht et al. categorize organic tubular materials into hollow helices, stacked rings, stacked rosettes, and monolayered lipid nanotubes as shown in **Figure 1.5**.[42] Organic nanotubes (ONTs) have gathered more attention due to potential biocompatibility, controllable terminal groups, uniform and tunable inner-diameters, and resemblance to carbon nanotubes.[43] Methods for their facile synthesis and large-scale production have been pursued. In addition, ONTs can encapsulate biomacromolecules, and water molecules in their inner cavity seem to have anomalous properties.

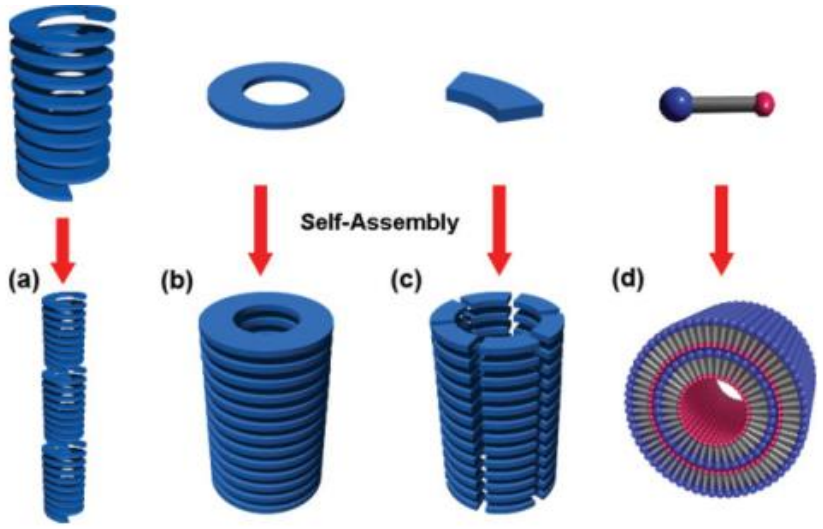

Figure 1.5. Self-assembled organic tubular architectures with open ends. **(a)** Aggregated helices from a hollow helix, **(b)** Stacked rings from a ring, **(c)** Stacked rosettes from a rosette, and **(d)** monolayer based LNT from an unsymmetrical bolaamphiphile. Reproduced with permission from reference (42). 2005, Copyright: Semantic Scholar.

ONTs are formed via self-assembly from individual organic molecules such as lipids, phospholipids and bolaamphiphiles as well as macromolecules. Nanotubular hollow features of these material are studied for applications such as controlled drug delivery, artificial chaperones, solar cells, nanocontainers, nanoreactors.[44-46] The credit for the discovery of ONTs based on artificial lipid molecules goes to Kunitake and Okahata: In 1977, they reported self-assembly of didodecyldimethylammonium bromide in water into spherical vesicles.[47] Subsequently, lipid nanotubes having relatively large inner (100-200 nm) and outer diameters (200-500 nm) with 50-200 μm in length were fabricated.[48] Later, Fuhrhop et al. successfully obtained lipid nanotubes with much smaller dimensions.[49] Since then, extensive studies have been carried out to explore possible functions of such self-assembled architectures.[50,46]

In comparison to lipid-based ONTs, bolaamphiphile-based ONTs are considered to be more suitable as drug delivery vehicles and adsorbents applications owing to their tunability of the inner and outer surface properties and their narrower pore size distribution.[48,51] Bolaamphiphiles can roll into layers to form ONTs of inner diameters 2-100 nm which is tunable by their chemical structure and arrangement.[52] Distinct inner and outer chemical compositions, which are defined by the asymmetric head groups of a bolaamphiphile, led to improved biocompatibility and target recognition by the outer surface, and to the control of the capture and release of encapsulated molecules. However, thorough understanding of detailed diffusion behavior of drug molecules inside the nanospace at different physiological conditions is important for future development of ONTs for various applications.

1.2.2 Self-Assembly of Asymmetrical Bolaamphiphiles

In general, the formation mechanisms of ONTs can be categorized to chiral self-assembly, scrolling of sheets, and packing directed self-assembly, as shown in **Figure 1.6**.[46] In chiral self-

assembly, amphiphilic molecules with few chiral centers, one head group and single or double tails forms helical ribbon intermediate based on anisotropic molecular interactions such as hydrogen bonding or π-π interactions, and ultimately offers ONTs.[46] On the other hand, a flat membrane formed from achiral molecules are energetically unfavorable, and thus spontaneously scrolls into an ONT to reduce the surface energy. In packing directed self-assembly, asymmetrical bolaamphiphiles form ONTs without the formation of any helical ribbon or flat membrane intermediates.[46]

Asymmetrical bolaamphiphiles have two distinct hydrophilic head groups separated by a hydrophobic spacer as shown in **Figure 1.7**. As mentioned earlier, a head group at the outer surface of a bolaamphiphile-based ONT can enhance biocompatibility and target recognition, while one inside controls molecular encapsulation and release. These head groups can be adjusted to attain desired functions of the ONTs. A critical packing parameter (*P*) defines the morphologies from packing directed self-assembly:[53]

$$P = \frac{v}{a_0} \text{ x } l_c \qquad \textbf{Equation 1}$$

where v is the volume of hydrophobic chain of the amphiphile, a_0 is the polar head surface area at the critical micelle concentration and l_c is the bolaamphiphile/amphiphile chain length.

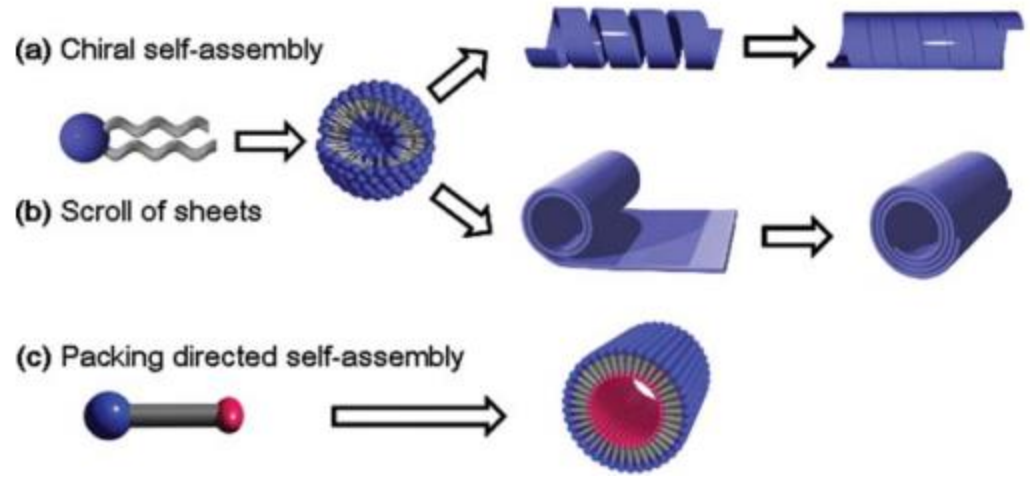

Figure 1.6 Formation mechanisms of organic nanotubes in general: **(a)** chiral self-assembly, **(b)** scrolling of sheets, and **(c)** packing directed self-assembly. Adapted with permission from reference (46). 2001, Copyright: Royal Society of Chemistry.

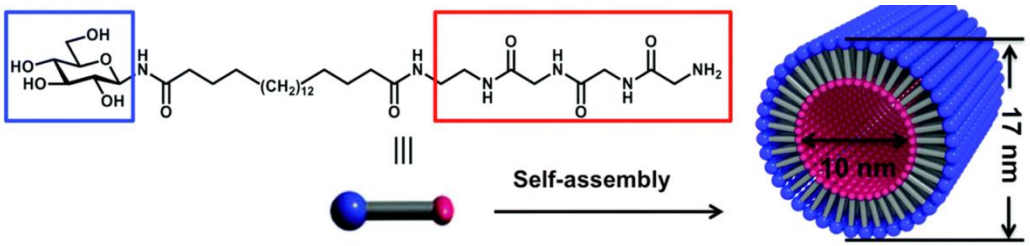

Figure 1.7 Precursor of the asymmetric bolaamphiphilic ONTs with amine and glucose as terminal head groups shown in blue and pink, also showing self-assembled nanotube with inner diameter 10 nm and wall thickness of 3.5 nm. Adapted with permission from reference (56). 2016 Copyright Royal Society of Chemistry.

The inner diameters of asymmetric ONTs formed by packing directed self-assembly (D_{inner}) can be easily tuned by adjusting the molecular shape and packing, as shown by the following equation:[46]

$$D_{\text{inner}} = 2A_{\text{s}}L/(A_{\text{s}} - A_{\text{l}}) \qquad \textbf{Equation 2}$$

where A_{s} and A_{l} are the cross-sectional areas of the smaller and larger head-groups, and L is the length of the molecule. The equation infers that D_{inner} is proportional to L, indicating the controllability of the inner diameter of an ONT by adjusting the length of the hydrophobic

spacer. In addition, solution conditions like pH, solvent composition and ionic strength may influence A_s and A_l, and thus their adjustment provide a means to attain the precise control of ONT diameters.[46] Rational modification of the precursor material and their packing can be optimized for further control of molecular encapsulation and release.

1.2.3 Molecular Encapsulation and Release with ONTs

Schnur et al. were the first to report molecular encapsulation and release with amphiphilic ONTs.[54] They showed the sustained release of transforming growth factor-β (TGF) from ONTs based on diacetylenic phospholipids.[54] Since then, there have been a myriad of investigations regarding encapsulation and release of proteins, DNA, drugs and dye molecules with various kinds of ONTs.[55,56] Effects of the loading concentration, size, and chemical properties (e.g., charge, hydrophobicity) of encapsulated species have been reported.[57-59] Such studies were mostly done for a batch of ONTs by spectroscopically monitoring the concentration of released species in solution. Higher loading concentration led to faster release rate due to larger concentration gradient between the inner solution of the ONTs and the solution. In addition, protein molecules with lower molecular weights showed faster release rates due to their higher diffusivity. For example, Meliander et al.[57] reported the faster release of myoglobin than albumin and thyroglobulin. Meanwhile, Banerjee and coworkers investigated the entrapment of insulin by peptide-based microtubules and showed pH dependence for both encapsulation and release:[60] The encapsulation was controlled by repulsive interactions between deprotonated insulin and carboxylate groups of microtubules. The release was restricted by strong hydrogen bonding between protonated insulin and microtubule inner surface at lower pH. These authors claimed that the microtubules could be used to retain and disperse insulin at gastric environment and in the intestines, respectively.

Kameta and coworkers visualized the dynamic encapsulation and nanofluidic behavior of QSY7-labelled ferritin using time-lapse fluorescence microscopy on the basis of fluorescence resonance energy transfer (FRET) with 4-fluoro-7-nitrobenzofurazan (NBD-F) tethered to the inner surface of bolaamphiphile-based ONTs (80 nm in inner diameter).[61] The fluorescence of the NBD-F disappeared at pH 6.8 due to the electrostatic encapsulation of the ferritin and subsequent quenching of donor dye. The encapsulation at pH 6.8 was further evidenced by TEM images. The importance of electrostatic interaction was supported by control experiments with QSY7-free ferritin at pH 6.8 and with QSY7-labeled ferritin at pH 9.0. They also investigated the effects of the inner surface charge of ONTs on the encapsulation of cationic starvation-induced DNA-binding protein (Dps) and anionic ferritin. ONTs with cationic surface groups could easily encapsulate ferritin, but not Dps. They further studied the effects of ONT inner diameter on DNA encapsulation. Double-stranded DNA could be accommodating to 80 nm diameter ONTs, but not 20-nm ONTs, reflecting its persistence length (50 nm). They did numerous studies to understand the roles of the diameter and inner/outer surface chemistry of ONTs in the encapsulation and release of various molecules.[62-64]

1.2.4 Molecular Diffusion inside ONTs

Molecular diffusion or adsorption inside ONTs are influenced by chemical and electrostatic interactions along with steric factors. Thus, it is very crucial to understand diffusion and adsorption behavior of encapsulated species within ONT for their efficient use. Guo et al. reported diffusion behavior of fluorescent dye molecules and peptides inside lipid-based ONTs using fluorescence recovery after photobleaching (FRAP) and fluorescence correlation spectroscopy (FCS).[65] They observed faster diffusion at the ends of a tube as compared to the middle region, which was explained by the lower packing density at the ends. They also showed

faster diffusion for species loaded at higher concentrations but did not clearly explain the diffusion behavior inside the ONTs. Kameta and coworkers measured the diffusion coefficient (D) of QSY-labeled ferritin within NBD-F-tethered ONTs.[61] The encapsulation and diffusion of the ferritin led to the quenching of NBD-F fluorescence, enabling the measurement of longitudinal diffusion distance of ferritin from the ONT openings. D was calculated from the square of diffusion distance (X^2) against time lapse (Δt) using an equation $(X^2) = 4D\Delta t$. The D inside 80 nm ONT was 7 $\mu m^2/s$, which was five times smaller than that in bulk solution. The authors attributed the slow diffusion to electrostatic interactions and higher viscosity of water in the nanospace regime, as Orwar et al. reported similar D for 30 nm fluorescent particles inside 200 nm-diameter phospholipid nanotubes.[66]

More recently, Xu et al. studied the effects of solution pH (6.4 – 8.4) and ionic strength on diffusion of anionic sulforhodamine B (SRB) within bolaamphiphile-based ONTs using imaging fluorescence correlation spectroscopy (imaging FCS).[56] In this study, ONTs having inner amine groups and inner diameters of 10 nm, which were synthesized by Dr. Kameta at National Institute of Advanced Industrial Science and Technology (AIST), Japan, were used. The diffusion was hindered by coulombic attraction with the inner surface charge and enhanced by the screening of the surface charge at higher ionic strength. D was in the order of 10^{-2} $\mu m^2/s$, which was much smaller than that in bulk solution. Subsequently, they investigated the local environments and diffusion behavior of solvatochromic Nile red (NR) and hydroxylated-Nile red (NR-OH) within the ONTs under ethanolic medium.[67] Less polar NR molecules were found to reside in less polar environments (dielectric constant = 3.45 – 3.91) than that for NR-OH molecules (dielectric constant ~ 4.19), and showed two-time higher D.

Chapters 5 and 6 will describe the extension of these studies using different dye molecules with different net charges and hydrophobicities, a wider pH range (3.4 – 8.4) and ONTs with different inner groups and diameters. The effects of ONT length on diffusion behavior were also shown. These thorough studies will give better insight into molecular diffusion in ONTs, and clarify the influences of coulombic, chemical and steric interactions on molecular encapsulation and release for their use as drug delivery vehicles in the bloodstream. These studies also demonstrated that imaging FCS is a very reliable and convenient tool to investigate the diffusion behavior of probe molecules along the ONTs.

1.3 References

(1) Namazi, H. Polymers in our daily life. *BioImpacts: BI*. **2017**, *7*, 73.

(2) Thompson, R.C.; Swan, S.H.; Moore, C.J.; Vom Saal, F.S. In Our Plastic Age. **2009**.

(3) Young, R.J.; Lovell, P.A. In Introduction to Polymers. *CRC press*. **2011.**

(4) Gracia, R.; Mecerreyes, D. Polymers with Redox Properties: Materials for Batteries, Biosensors and More. *Polymer Chemistry*. **2013**, *4*, 2206-2214.

(5) Peerce, P. J.; Bard, A. J. Polymer-Films on Electrodes Part III. Digital-Simulation Model for Cyclic Voltammetry of Electroactive Polymer Film and Electrochemistry of Poly(vinylferrocene) on Platinum. *J. Electroanal. Chem. Interfacial Electrochem*. **1980**, *114*, 89-115.

(6) Hunter, T. B.; Tyler, P. S.; Smyrl, W. H.; White, H. S. Impedance Analysis of Poly(vinylferrocene) Films. The Dependence of Diffusional Charge Transport and Exchange Current-Density on Polymer Oxidation-State. *J. Electrochem. Soc*. **1987**, 134, 2198-2204.

(7) Schacher, F.H.; Rupar, P.A.; Manners, I. Functional block copolymers: nanostructured materials with emerging applications. *Angewandte Chemie International Edition*. **2012**, *51*, 7898-7921.

(8) Hamley, I. W.The Physics of Block Copolymers. *Oxford University Press: Oxford*. **1998**, 432.

(9) Bates, F. S.; Fredrickson, G. H. Block Copolymers - Designer Soft Materials. *Phys. Today* **1999**, *52*, 32−38.

(10) Ito, T. Block Copolymer-Derived Monolithic Polymer Films and Membranes Comprising Self-Organized Cylindrical Nanopores for Chemical Sensing and Separations. *Chem. - Asian J.* **2014**, 9, 2708−2718.

(11) Hardy, C. G.; Zhang, J.; Yan, Y.; Ren, L.; Tang, C. Metallopolymers with Transition Metals in the Side-Chain by Living and Controlled Polymerization Techniques. *Prog. Polym. Sci*. **2014**, 39, 1742−1796.

(12) Pietschnig, R. Polymers with Pendant Ferrocenes. *Chem. Soc. Rev*. **2016**, *45*, 5216−5231.

(13) Durkee, D. A.; Eitouni, H. B.; Gomez, E. D.; Ellsworth, M. W.; Bell, A. T.; Balsara, N. P. Catalysts from Self-Assembled Organometallic Block Copolymers. *Adv. Mater*. **2005**, 17, 2003−2006.

(14) Zhou, J.; Whittell, G.R.; Manners, I. Metalloblock Copolymers: New Functional Nanomaterials. *Macromolecules.* **2014**, 47, 3529–3543.

(15) Li, B.; Sauve, G.; Iovu, M.C.; Jeffries-EL, M.; Zhang, R.; Cooper, J.; Santhanam, S.; Schultz, L.; Revelli, J.C.; Kusne, A.G.; Kowalewski, T.; Snyder, J.L.; Weiss, L.E.; Fedder, G.K.; McCullough, R.D.; Lambeth, D.N. Volatile Organic Compound Detection using Nanostructured Copolymers. *Nano Lett*. **2006**, 6, 1598–1602.

(16) Li, J. K.; Zou, S.; Rider, D. A.; Manners, I.; Walker, G. C. Differential Conductivity in Self-Assembled Nanodomains of a Diblock Copolymer Using Polystyrene-block-Poly(ferrocenylethylmethylsilane). *Adv. Mater*. **2008**, *20*, 1989–1993.

(17) Kumari, P.; Khawas, K.; Hazra, S.; Kuila, B. K. Poly(3-hexyl thiophene)-*b*-poly(N-isopropyl acrylamide): Synthesis and its Composition Dependent Structural, Solubility, Thermoresponsive, Electrochemical, and Electronic Properties *J. Polym. Sci. A: Polym. Chem.* **2016**, 54, 1785–1794.

(18) Plamper, F. A. Changing Polymer Solvation by Electrochemical Means: Basics and Applications. *Adv. Polym. Sci*. **2015**, *266*, 125–212.

(19) Yan, Y.; Zhang, J.; Ren, L.; Tang, C. Metal-Containing and Related Polymers for Biomedical Applications. *Chem. Soc. Rev.* **2016**, *45*, 5232–5263.

(20) Heller, A.; Feldman, B Electrochemical Glucose Sensors and their Applications in Diabetes Management. *Chem. Rev*. **2008**, *108*, 2482–2505.

(21) Yoshida, J.-I.; Kataoka, K.; Horcajada, R.; Nagaki, A. Modern Strategies in Electroorganic Synthesis. *Chem. Rev.* **2008**, *108*, 2265–2299.

(22) Ito, T.; Ghimire, G. Electrochemical Applications of Microphase-Separated Block Copolymer Thin Films. *ChemElectroChem*. **2018**, *5*, 2937-2953.

(23) Li, M.; Ober, C. K. Block Copolymer Patterns and Templates. *Mater. Today*. **2006**, *9*, 30–39.

(24) Lazzari, M.; De Rosa, C. In Block Copolymers in Nanoscience (Eds.: M. Lazzari, G. Liu, S. Lecommandoux), *Wiley GmbH & Co., Weinhelm*. **2006**, 191–231.

(25) Majda, M. In Molecular Design of Electrode Surfaces (Ed.: R. W. Murray), *John Wiley & Sons, New York*. **1992**, 159-206.

(26) Terrill, R. H.; Murray, R. W. In Molecular Electronics: A 'Chemistry for the21st Century' Monograph (Eds.: J. Jortner, M. Ratner), *Blackwell Science,Malden, MA.* **1997**, 215–239.

(27) Blauch, D. N.; Saveant, J.-M. Dynamics of Electron Hopping in Assemblies of Redox Centers. Percolation and Diffusion. *J. Am. Chem. Soc.* **1992**, *114*, 3323–3332.

(28) Oyama, N.; Anson, F. C. Factors Affecting the Electrochemical Responses of Metal Complexes at Pyrolytic Graphite Electrodes Coated with Films of Poly (4-Vinylpyridine). *J. Electrochem. Soc*. **1980**, *127*, 640–647.

(29) Bard, A. J.; Faulkner, L. R. Electrochemical Methods, Fundamentals and Applications, 3rd ed., *Wiley*, *New York*, **2001**.

(30) Chen, T.; Wang, L.; Jiang, G.; Wang, J. Dong, X.; Wang, X.; Zhou, J.; Wang, C.; Wang, W. Electrochemical Behavior of Poly(ferrocenyldimethylsilane-b-dimethylsiloxane) Films. *J. Phys. Chem. B*. **2005**, *109*, 4624–4630.

(31) Li, F.; Pandey, B.; Ito, T. Linker-Based Control of Electron Propagation through Ferrocene Moieties Covalently Anchored onto Insulator-Based Nanopores Derived from a Polystyrene–Poly(methylmethacrylate) Diblock Copolymer. *Langmuir*. **2012**, *28*, 16496–16500.

(32) Sumi, K.; Anson, F. C. Electron transfer to Anionic Reactants Incorporated within Polycationic Coatings on Glassy Carbon Electrodes. Comparison of Random and Block Copolymers. *J. Phys. Chem*. **1986**, 90, 3845–3850.

(33) Ghimire, G.; Yi, Y.; Derylo, M. A.; Baker, L. A.; Ito, T. Electron Propagation within Redox-Active Microdomains in thin Films of Ferrocene-Containing Diblock Copolymers. *Langmuir*. **2015**, *31*, 12307–12314.

(34) Ghimire, G.; Coceancigh, H.; Yi, Y.; Ito, T. Electrochemical Characterization and Catalytic Application of Gold-Supported Ferrocene-Containing Diblock Copolymer Thin Films in Ethanol Solution. *ACS Appl. Mater. Interfaces*. **2017**, 9, 2906–2913.

(35) Garcia, M. P.G.; Armada, J.; Losada, F.; Lopez-Villanueva, J.; Frey, H.; Alonso, B.; Casado, C. M. Electrochemical and Bioelectrocatalytical Properties of Novel Block-Copolymers Containing Interacting Ferrocenyl Units. *J. Organomet. Chem*. **2008**, *693*, 2803–2811.

(36) Lee, J.; Ahn, H.; Choi, I.; Boese, M.; Park, M. J. Enhanced Charge Transport in Enzyme-Wired Organometallic Block Copolymers for Bioenergy and Biosensors. *Macromolecules.* **2012**, *45*, 3121–3128.

(37) Yuan, L.; Wei, W.; Liu, S. Label-free Electrochemical Immunosensors Based on Surface-Initiated Atom Radical Polymerization. *Biosens. Bioelectron*. **2012**, 38, 79–85.

(38) Kim, B. Y.; Ratcliff, E. L.; Armstrong, N. R.; Kowalewski, T.; Pyun, J. Ferrocene Functional Polymer Brushes on Indium Tin Oxide via Surface-Initiated Atom Transfer Radical Polymerization. *Langmuir*. **2010**, 26, 2083–2092.

(39) Li, F.; Ito, T. Complexation-Induced Control of Electron Propagation based on Bounded Diffusion through Nanopore-Tethered Ferrocenes. *J. Am. Chem. Soc*. **2013**, *135*, 16260–16263.

(40) Eloi, J.-C.; Ward Jones, S. E.; Poor, V.; Okuda, M. Gwyther, J.; Schwarzacher, W. Electrochemically Triggered Selective Adsorption of Biotemplated Nanoparticles on Self-Assembled Organometallic Diblock Copolymer Thin Films. *Adv. Funct. Mater*. **2012**, *22*, 3273–3278.

(41) Geng, Y.A.N.; Dalhaimer, P.; Cai, S.; Tsai, R.; Tewari, M.; Minko, T.; Discher, D.E. Shape Effects of Filaments Versus Spherical Particles in Flow and Drug Delivery. *Nature nanotechnology*. **2007**, *2*, 249.

(42) Block, M.A.B.; Kaiser, C.; Khan, A.; Hecht, S. Discrete Organic Nanotubes Based on a Combination of Covalent and Non-Covalent Approaches. In *Functional Molecular Nanostructures.* **2005**, 89-150. Springer, Berlin, Heidelberg.

(43) Shimizu, T. Self-Assembled Lipid Nanotube Hosts: The Dimension Control for Encapsulation of Nanometer-Scale Guest Substances. *Journal of Polymer Science Part A: Polymer Chemistry*.**2006**, *44*, 5137-5152.

(44) Kameta, N. Soft Nanotube Hosts for Capsulation and Release of Molecules, Macromolecules, and Nanomaterials. *Journal of Inclusion Phenomena and Macrocyclic Chemistry*. **2014**, *79*, 22.

(45) Shimizu, T. Self-Assembled Organic Nanotubes: Toward Attoliter Chemistry. *Journal of Polymer Science Part A: Polymer Chemistry*. **2008**, *46*, 2601-2611.

(46) Kameta, N., Minamikawa, H. and Masuda, M., 2011. Supramolecular organic nanotubes: how to utilize the inner nanospace and the outer space. Soft Matter, 7(10), pp.4539-4561.

(47) Kunitake, T.; Okahata, Y. A Totally Synthetic Bilayer Membrane. *J. Am. Chem. Soc*. **1977**, 99, 3860−3861.

(48) Shimizu, T.; Kameta, N.; Ding, W.; Masuda, M. Supramolecular Self-Assembly into Biofunctional Soft Nanotubes: From Bilayers to Monolayers. *Langmuir*, **2016**, *32*, 12242-12264.

(49) Fuhrhop, J. H.; Koening, J. In Membranes and Molecular Assemblies: The Synkinetic Approach. (Ed: Stoddart, J. F). *The Royal Society of Chemistry*: *Cambridge.* **1994**.

(50) Shimizu, T.; Masuda, M.; Minamikawa, H. Supramolecular Nanotube Architectures Based on Amphiphilic Molecules. *Chem. Rev*. **2005**, *105*, 1401−1443.

(51) Shimizu, T. Self-Assembly of Discrete Organic Nanotubes. *Bull. Chem. Soc. Jpn*. **2018**, *91*, 623-668.

(52) Ghimire, G.; Espinoza, R.; Xu, H.; Nagasaka, S.; Kameta, N.; Masuda, M.; Higgins, D. A.; Ito, T. Diffusion Behavior of Differently Charged Molecules in Self-Assembled Organic Nanotubes Studied Using Imaging Fluorescence Correlation Spectroscopy. *Langmuir*. **2019**, *35*, 7783-7790.

(53 Shimizu T. In *Molecular-and Nano-tubes*. (Eds: Hayden, O.; Nielsch, K.) *Springer Science & Business Media*. **2011**.

(54) Schnur, J.M.; Price, R.; Rudolph, A.S. Biologically Engineered Microstructures: Controlled Release Applications. *Advances in Drug Delivery Systems.* **1994**, *6*, 3-13.

(55) Kameta, N.; Minamikawa, H.; Masuda, M.; Mizuno, G.; Shimizu, T. Controllable Biomolecule Release from Self-Assembled Organic Nanotubes with Asymmetric Surfaces: pH and Temperature Dependence. *Soft Matter*. **2008**, *4*, 1681-1687.

(56) Kameta, N.; Lee, S. J.; Masuda, M.; Shimizu, T. Biologically Responsive, Sustainable Release from Metallo-Drug Coordinated 1D Nanostructures. *J. Mater. Chem*. *B*. **2013**, *1*, 276-283.

(57) Xu, H.; Nagasaka, S.; Kameta, N.; Masuda, M.; Ito, T.; Higgins, D. A. Imaging Fluorescence Correlation Spectroscopy Studies of Dye Diffusion in Self-Assembled Organic Nanotubes. *Phys. Chem. Chem. Phys*. **2016**, *18*, 16766-16774.

(58) Meilander, N.J.; Yu, X.; Ziats, N.P.; Bellamkonda, R.V. Lipid-Based Microtubular Drug Delivery Vehicles. *Journal of Controlled Release*. **2001**, *71*, 141-152.

(59) Meilander, N.J.; Pasumarthy, M.K.; Kowalczyk, T.H.; Cooper, M.J.; Bellamkonda, R.V. Sustained Release of Plasmid DNA using Lipid Microtubules and Agarose Hydrogel. *Journal of Controlled Release*. **2003**, *88*, 321-331.

(60) Henricus, M.M.; Johnson, K.T.; Banerjee, I.A. Investigation of Insulin Loaded Self-Assembled Microtubules for Drug Release. *Bioconjugate chemistry*. **2008**, *19*, 2394-2400.

(61) Kameta, N.; Masuda, M.; Minamikawa, H.; Mishima, Y.; Yamashita, I.; Shimizu, T. Functionalizable Organic Nanochannels based on Lipid Nanotubes: Encapsulation and Nanofluidic Behavior of Biomacromolecules. *Chemistry of materials*. **2007**, *19*, 3553-3560.

(62) Ding, W.; Wada, M.; Minamikawa, H.; Kameta, N.; Masuda, M.; Shimizu, T. Cisplatin-Encapsulated Organic Nanotubes by Endo-Complexation in the Hollow Cylinder. *Chemical Communications*. **2012**, *48*, 8625-8627.

(63) Liu, N.; Higashi, K.; Kikuchi, J.; Ando, S.; Kameta, N.; Ding, W.; Masuda, M.; Shimizu, T.; Ueda, K.; Yamamoto, K.; Moribe, K. Molecular-Level Understanding of the Encapsulation and Dissolution of Poorly Water-Soluble Ibuprofen by Functionalized Organic Nanotubes using Solid-State NMR Spectroscopy. *The Journal of Physical Chemistry B*. **2016**, *120*, 4496-4507.

(64) Kameta, N.; Asakawa, M.; Masuda, M.; Shimizu, T. Self-Assembled Organic Nanotubes Embedding Hydrophobic Molecules within Solid Bilayer Membranes. *Soft Matter*. **2011**, 7, 85-90.

(65) Guo, L.; Chowdhury, P.; Fang, J.; Gai, F. Heterogeneous and Anomalous Diffusion Inside Lipid Tubules. *The journal of physical chemistry B*. **2007**, *111*, 14244-14249.

(66) Karlsson, R.; Karlsson, M.; Karlsson, A.; Cans, A.S.; Bergenholtz, J.; Åkerman, B.; Ewing, A.G.; Voinova, M.; Orwar, O. Moving-Wall-Driven Flows in Nanofluidic Systems. *Langmuir*. **2002**, *18*, 4186-4190.

(67) Xu, H.; Nagasaka, S.; Kameta, N.; Masuda, M.; Ito, T.; Higgins, D.A. Spectroscopic Imaging Studies of Nanoscale Polarity and Mass Transport Phenomena in Self-Assembled Organic Nanotubes. *Physical Chemistry Chemical Physics*. **2017**, *19*, 20040-20048.

Chapter 2 - Instrumental Methods used in the Research

This chapter will discuss the instrumental techniques employed in the research projects with both PS-*b*-PAEFc and ONTs. Spectroscopic ellipsometry was used to measure the thickness of thin PS-*b*-PAEFc films on gold-coated silicon substrates. Atomic force microscopy (AFM) was used to measure the surface morphologies of the thin films. Cyclic voltammetry (CV) and chronocoulometry (CC) were used for the electrochemical characterization of the thin films. UV-Vis absorption spectroscopy was used to determine the acid dissociation constant (pK_a) and octanol–water partition coefficient ($\log P_{oct}$) of each of three fluorescent dyes loaded to ONTs for imaging FCS experiments. TIRF-mode video microscopy was employed to acquire fluorescence video images of ONTs immobilized on a glass coverslip, which gave fluorescence time-transient data from individual ONTs for imaging FCS analysis.

2.1 Spectroscopic Ellipsometry (SE)[1]

The word ellipsometry comes from 'elliptically polarized light' which is defined as light composed of two plane-polarized waves of differing amplitudes or phase other than 90°. Spectroscopic ellipsometry is a very sensitive and non-destructive analytical technique that is used to assess the optical properties and thickness of a thin film on a substrate. It measured changes in optical parameters associated with the conversion of obliquely-incident, linearly-polarized light to elliptically polarized light as a result of reflection at interfaces (**Figure 2.1**). Electric vector (*E*) of the incident polarized light consists of two components that are parallel and perpendicular to the plane of incidence and are designated by Greek letters π and σ, respectively. When the light reflects off from the sample interfaces of different media, these two components undergo changes and can be related to ellipsometric parameters *viz.* amplitude ratio ($\tan\Psi$) of the

reflection coefficients and phase difference (Δ), which are the raw information collected by an ellipsometer. The relation is defined by the following equation:

$$\rho = \frac{\rho_\pi}{\rho_\sigma} = \tan(\Psi)e^{j\Delta} \qquad \textbf{Equation 2.1}$$

where ρ_π and ρ_σ are reflection coefficients of the light that are polarized parallel and perpendicular to the plane of incidence, ρ is the complex ratio, and j is a number. Psi (Ψ) and delta (Δ) collected by the instrument are plotted against wavelength and fitted to an appropriate model for the estimation of thickness (d) and refractive index (n).

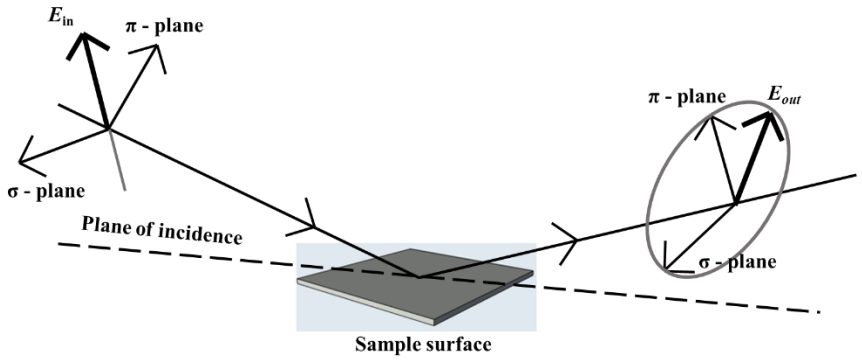

Figure 2.1 Illustration of light path in a spectroscopic ellipsometer. Figure adapted from reference 1. Reproduced with permission from reference 1. 2004, Copyright: Springer.

Optical components of a spectroscopic ellipsometer is given in **Figure 2.2**. Light emitted from a source (a laser or a lamp) passes through a linear polarizer (P) and compensator (C) before striking onto the sample of interest. It is then immediately reflected towards another polarizer and finally to a detector. Laser sources have intense power and ability to collimate but are monochromatic, and thus are not preferred light sources in ellipsometric measurements. Mostly used are Xenon lamps which can produce a broad range of wavelengths and suitable for the instrument. The purpose of a linear polarizer is to convert unpolarized light emitted from the Xenon lamp into linearly polarized light, where α_P represents rotational angle of the polarizer against the direction of π component of the electric vector. Similarly, a compensator alternates

the polarization state of the incoming light wave to adjust the retardation of the two perpendicular components of the electric vector. Light passing through the compensator then hits the sample surface where a portion of it is transmitted and the rest is reflected defined by Fresnel transmission (τ_π, τ_σ) and reflection (ρ_π, ρ_σ) coefficients. The reflected light then passes through another linear polarizer called analyzer and finally reaches the detector that can measure incoming light intensity and change of polarization.

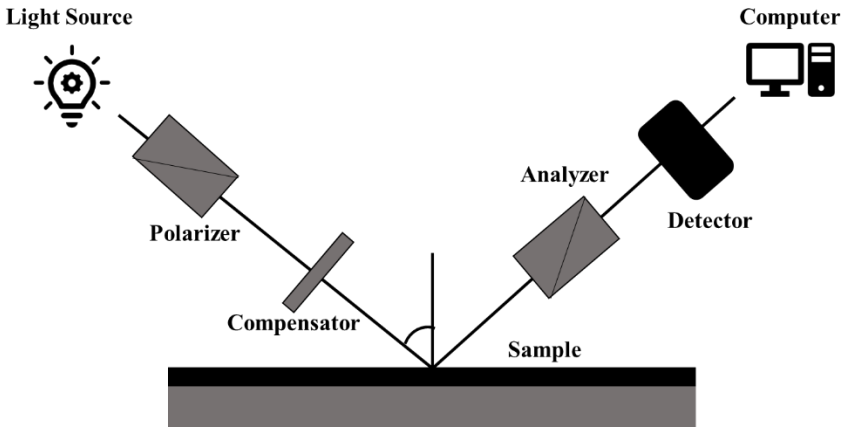

Figure 2.2 Schematic diagram showing components of a spectroscopic ellipsometer. Figure adapted with permission from reference 1. 2004, Copyright: Springer.

2.2 Atomic Force Microscopy (AFM)[2,3]

AFM utilizes attractive or repulsive forces between a sample surface and a nanoscale tip (< 10 nm) to create a 3D/2D surface topography image. It was first developed to overcome the drawbacks of scanning tunneling microscopy (STM) which could only image conducting or semi-conducting surfaces. Due to its ability to image any kinds of surfaces ranging from polymers to biological samples with a resolution up to a few angstroms, AFM has been a routine imaging technique in many laboratories today.

Basic instrumentation of an AFM is given in **Figure 2.3**. The tip is normally made of silicon or silicon nitride. However, the material may vary according to the need of spring

constant or resonance frequency. The tip used in AFM is supported by a flexible cantilever. When the tip approaches 0.2 to 10 nm to the sample, it experiences a force which is proportional to the cantilever deflection. According to Hooke's law:

$$F = -kx \qquad \textbf{Equation 2.2}$$

where F is the elastic force existing between the tip and the sample surface, k is spring constant and x is the deflection of the cantilever. Typical values of F are in the range of 10^{-6} – 10^{-9} N. Once the cantilever deflects, laser beam that strikes its back bounces to a position sensitive photodiode detector containing four quadrants. Position of the laser on the photodiode while the tip is scanning the sample surface is maintained by a process called a feedback loop using a voltage-controlled piezo stage.

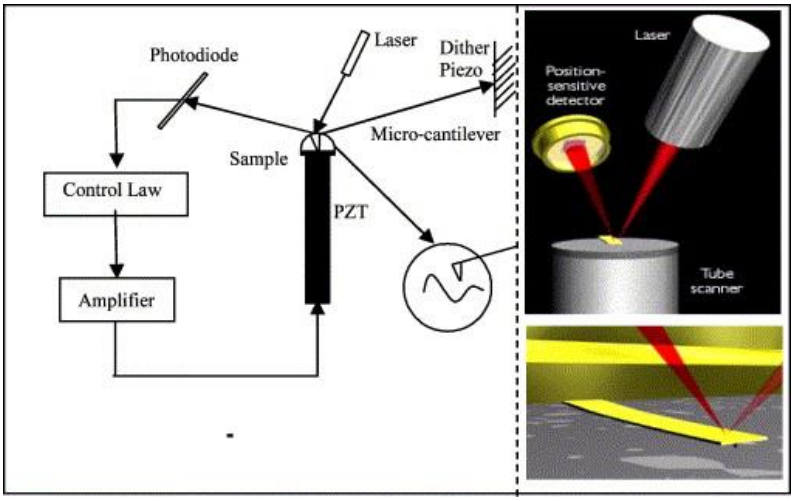

Figure 2.3 Major components of AFM. Reproduced with permission from reference 3. 2004, Copyright: Elsevier.

AFM is divided into three basic sub-categories based on how the tip and surface interact and the kind of force acting between them. In contact mode, the tip feels the surface of the sample at a contact position. Since the attractive forces caused by van der Waals interaction are very strong near the sample surfaces, the tip might be prone to snap into the surface resulting in

significant noise and drift. Tapping mode uses oscillating motion of the tip closer to its resonance frequency causing intermitted contact with the sample surface. Forces arising from van der Walls, electrostatic and dipole-dipole interactions may be associated in this mode causing the cantilever's oscillation amplitude change at a closer distance. Due to limited contact with the sample surface, this mode might be better in terms of noises or drift. This mode was used to obtain height and phase images for experiments in this dissertation. The height image reflects nanoscale surface topography, and the phase image give local information on surface compositional heterogeneity that reflects difference in chemical functional groups and material elasticity. Non-contact mode uses the oscillation of the cantilever above (<10 nm) the sample surface. This mode is free from tip degradation and may be preferred to contact and tapping mode, in that respect, but is usually applicable only in ultrahigh vacuum.

2.3 Cyclic Voltammetry (CV)[4,5]

Cyclic Voltammetry (CV) is a routinely used electrochemical technique that measures the current at an electrode at a cycle of fixed range of applied voltage in a static solution. A plot of current against potential provides qualitative and quantitative electrochemical information like oxidation/reduction, their reversibility, formal reduction potential, stoichiometry, and diffusion behavior of an analyte. A typical cyclic voltammogram with a triangular potential wave-form is shown in **Figure 2.4**. E_{pc}, E_{pa}, i_{pc} and i_{pa} represent cathodic peak potential, anodic peak potential, cathodic peak current and anodic peak current, respectively. CV experiments measure both faradaic (arising from redox reactions) and non-faradaic (arising from change in the distribution of ionic species within the electrical double layer near the working electrode) currents. A non-faradaic current is often subtracted to discuss redox processes on the electrode of interest.

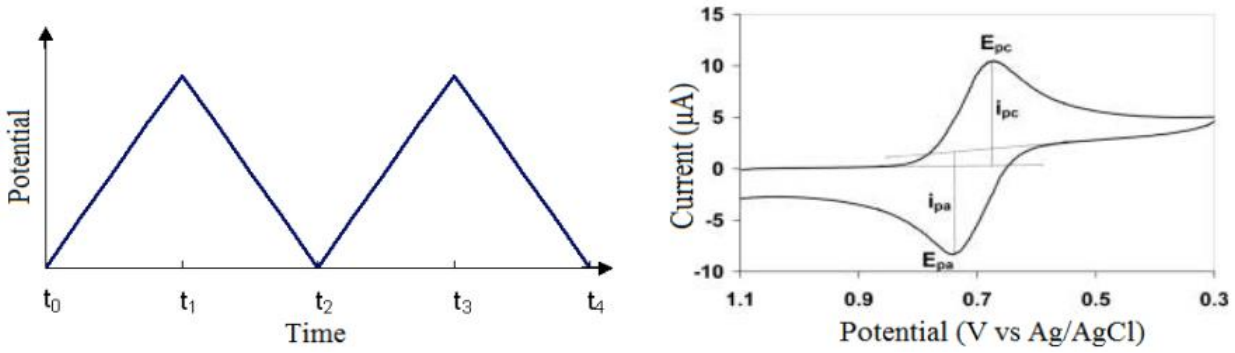

Figure 2.4 (a) Triangular potential waveform and **(b)** typical cyclic voltammogram. Reproduced with permission from reference 5. 2001, Copyright: Wiley.

CV measurements are usually carried out using a three-electrode cell based on working, reference and counter electrodes. A working electrode, which is often a disk electrode based on metal (Pt, Au) or carbon, is the electrode of interest where a current is measured as a result of potential application. A working electrode can be chemically modified to tailor the properties of the electrode, as gold electrodes were modified with thin PS-*b*-PAEFc films in Chapters 3 and 4. A reference electrode is a half-cell with a constant potential, and define a potential applied to the working electrode. A Ag/AgCl electrode is commonly used for CV measurements in aqueous solutions, and a Ag/Ag^+ reference electrode is used in non-aqueous solutions. Lastly, a counter electrode, which is usually based on Pt, is used to close the circuit so that current flows from/to the working electrode.

The shape of CV data, faradaic currents and redox potentials provide rich information on the electrode processes of interest. CV shape reflects the diffusive nature of the redox species and electrochemical reversibility of the reaction. Faradaic currents are controlled by the concentration and diffusion coefficient of redox species as well as the electrode area. Redox potentials give insight into the formal potential of redox species and the electrochemical reversibility of redox processes. They are also affected by potential sweep rate (v). For example,

if faradaic currents are controlled by the reversible electrode reaction of species adsorbed onto a working electrode, a peak current (i_p) is proportional to v as shown by the following equation:

$$i_p = n^2F^2A\Gamma_c v/RT \qquad \textbf{Equation 2.3}$$

where n is the number of electrons involved, F is the Faraday constant (96,485 C/mol), A is the electrode area, Γ_c is the electroactive surface coverage, R is the molar gas constant, and T is the temperature in Kelvin. In contrast, faradaic currents are controlled by reversible redox reactions of species that linearly diffuse from the solution, the difference between E_{pa} and E_{pc} is equal to $59/n$ mV, and i_p is proportional to the square root of scan-rate ($v^{1/2}$), as shown by the following equation:

$$i_p = (2.69 \times 10^5)n^{3/2}AD^{1/2}v^{1/2}C \qquad \textbf{Equation 2.4}$$

where D is the diffusion coefficient of the redox species and C is its concentration.

2.4 Chronocoulometry (CC)[4,5]

Chronocoulometry (CC) is another useful electrochemical technique in which electric charge (Q) is measured as a function of time (t) upon applying a fixed potential step from E_1 to E_2 as shown in **Figure 2.6**. It is used to determine electrode area, D of redox species, or its concentration. CC measurements are carried out using a three-electrode cell as with CV measurements. Prior to CC experiments, CV measurements are carried out to select appropriate E_1 and E_2: These potentials should be ≥ 120 mV more anodic and more cathodic than E_{pa} and E_{pc}, respectively, to ensure the complete oxidation and reduction of the redox species. Q is determined by the concentration of redox species that diffuse from the solution, the surface density of redox-active adsorbates (Γ), and capacitive charge (Q_{dl}), as shown in **Equation 2.5**:[5]

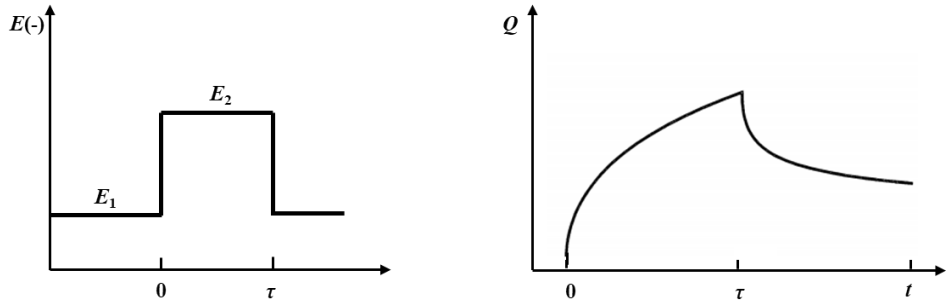

Figure 2.5 (a) Potential steps and **(b)** typical chronocoulogram. Reproduced with permission from reference 1. 2001, Copyright: Wiley.

$$Q = \frac{2nFAD_{ap}^{1/2}Ct^{1/2}}{\pi^{1/2}} + Q_{dl} + nFA\Gamma \qquad \textbf{Equation 2.5}$$

This equation indicates that the slope of a Q–$t^{1/2}$ plot can be used to determine D, if C and A are known. The y-intercept of the plot should afford the density of redox-active adsorbates if Q_{dl} can be estimated from CV data. In Chapters 3 and 4, D_{ap} values in PS-*b*-PAEFc films were determined using CC by estimating C of reactive ferrocene moieties from $Q_{a,max}$, which is Q obtained at long t, A and the ellipsometric thickness (d) of the dried film (*i.e.*, $C = Q_{a,max}/FAd$).

2.5 UV-Visible Absorption Spectroscopy[6]

Ultraviolet-visible (UV-visible) absorption spectroscopy is one of the simplest forms of spectroscopic methods that utilizes the absorption (or reflection) of UV and visible light (wavelength range: 200 – 900 nm) by liquid/solution, gaseous and solid samples. The energy of a UV-visible photon corresponds to those of the n-σ*, π-π* and n-π* transitions of valence electrons in molecular and ionic species. Since the energy required for electronic transition is specific to target species, this method is routinely used to determine the concentrations of ionic, organic and macromolecular species (C) from the absorbance (A) at a specific wavelength using the Beer-Lambert law (**Equation 2.6**):

$$A = abC \qquad \textbf{Equation 2.6}$$

$$A = \log(\frac{I_0}{I})$$ **Equation 2.7**

In these equations, *a* is the molar absorptivity of analyte species at the specific wavelength, *b* is the path-length of the light, and I_0 and I are the intensities of incident and transmitted beams, which are usually measured using blank and sample solutions. The instrumental components of a UV-Vis spectrophotometer are given in **Figure 2.6**. Light emitted from a source goes through a wavelength selector called monochromator, transmits through a sample, and then reaches the detector to measure the light intensity. A common light source includes a tungsten filament lamp, a deuterium arc lamp, and a xenon arc lamp. A monochromator normally consists of an entrance slit, a collimating lens, a grating or prism for dispersion, another lens to focus, and an exit slit. Cuvettes used for measurements of solution samples are made from various materials like plastic, glass, fused silica or quartz and should be appropriately chosen according to a wavelength range of interest. Photomultiplier tube is commonly used as a detector.

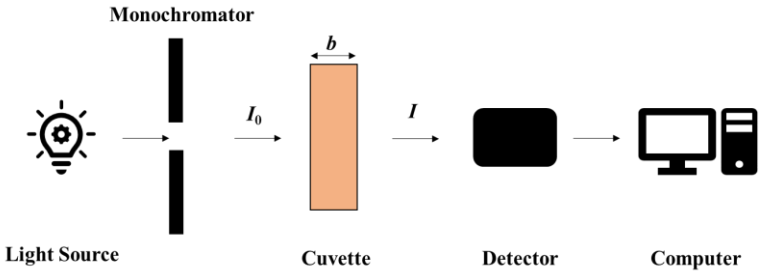

Figure 2.6 Components of a UV-Vis spectrophotometer. Figure adapted from reference 6. 2006, Copyright: Thomson Brooks/Cole.

2.6 Proton Nuclear Magnetic Resonance (^{1}H-NMR) Spectroscopy[7]

^{1}H-NMR spectroscopy is widely used in science for the structural determination of organic/inorganic compounds and biological materials like peptides or proteins in solutions and solids. Proton is a positively charged particle that can generate a magnetic field. The nuclear spins of protons undergo alignment with an externally-applied strong magnetic field, which are

otherwise random as shown in **Figure 2.7**. Difference in energy (ΔE) between the differently oriented spins (designated as α and β) depends linearly on the magnetic field (B_0), as shown in **Figure 2.8**. Upon irradiating a sample by radio frequency waves with the energy of ΔE, protons in the α spin state are promoted to β-spin state, followed by the relaxation to their original state by emitting the radio frequency waves. ΔE is given by the following equation:

$$\Delta E = \hbar\nu = h\frac{\gamma}{2\pi}B_0 \qquad \textbf{Equation 2.8}$$

where h is the Planck's constant, ν is the frequency of the radio frequency wave, γ is gyromagnetic ratio that depends on the magnetic moment of a nucleus, and B_0 is the magnetic field. For proton, value of γ is 2.675 x 10^8 $T^{-1}s^{-1}$.

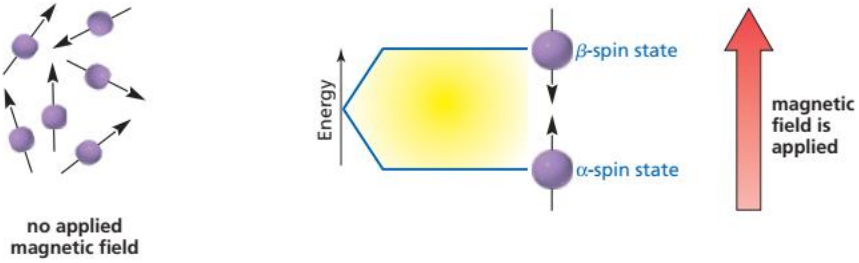

Figure 2.7 Showing random and aligned orientation of the nuclear spins in the absence and presence of external magnetic field. Figure reproduced with permission from reference 7.

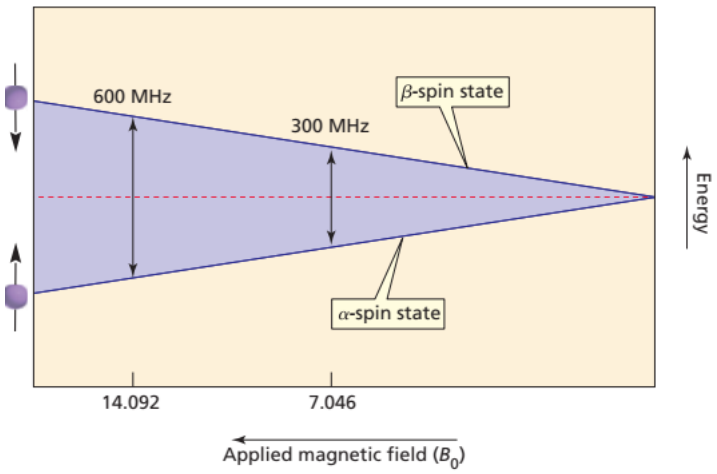

Figure 2.8. Showing the relation between magnetic field and the energy difference (ΔE). Figure reproduced with permission from reference 7.

In a ^{1}H-NMR spectrum, resonance frequencies of the protons are plotted against chemical shift (δ) in parts per million (ppm) with reference to tetramethyl silane (TMS). Chemical shift indicates the particular environment of a proton in the molecule. The presence of an electronegative atom in the molecule withdraws electrons away from the proton and causes what's known as a deshielding effect to have a resonance peak shift in the "downfield" direction. The integration of a resonance peak gives information about the number of chemically equivalent proton atoms. Also, neighboring proton atoms can affect the resonance peaks by splitting them according to n+1 rule. For example, a triplet peak is observed if a particular proton atom has two neighboring proton atoms. The structure of molecule can be determined from chemical shifts, integration and splitting of the peaks.

Basic components of a ^{1}H-NMR spectrometer consist of a powerful magnet with a slot to load a sample in a tube, a radio frequency generator, a detector and a computer. Basically, the sample in a tube is dissolved in an appropriate deuterated solvent.

2.7 Imaging Fluorescence Correlation Spectroscopy (Imaging FCS)[8,11]

Imaging FCS is a multiplexed version of fluorescence correlation spectroscopy (FCS) in which fluorescent time transients can simultaneously be collected at multiple locations in a selected region using a highly sensitive charge coupled device (CCD) detector. In FCS, time transient of fluorescent intensity from a tiny confocal volume defined by diffraction limited focus of the excitation laser is collected through a pin-hole by an avalanche photo detector or a photomultiplier tube. The time transient contains fluorescence intensity fluctuations caused by molecules entering and exiting the detection volume, and then is autocorrelated and fitted with an appropriate diffusion model to obtain diffusion coefficient (D). Although, FCS is an excellent technique that can measure D of fluorescent molecules with high temporal resolution, we get

information only from a single point, and thus one needs to scan the detection area to gain the distribution of local *D* in a wide region. To overcome this limited mapping capability of FCS, imaging FCS was introduced, albeit compromising some temporal resolution.

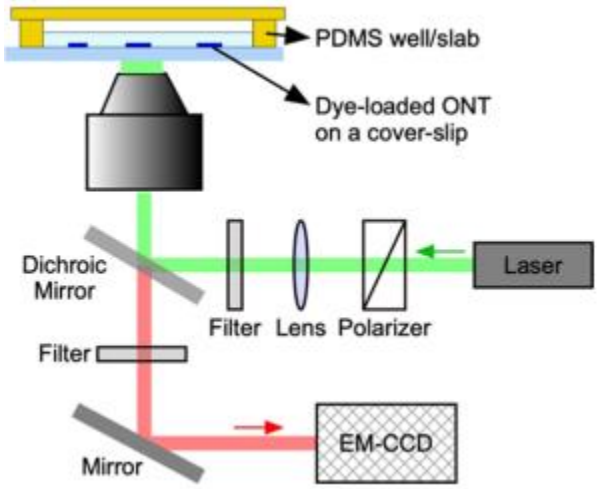

Figure 2.9 Microscopic setup for imaging FCS experiment. Reproduced with permission from reference 10. 2019, Copyright: American Chemical Society.

A typical microscopic set up for imaging FCS is shown in **Figure 2.9**. Laser light of an appropriate wavelength (λ) passes through several well-aligned optical components like polarizers, filters and lenses, reflected at a dichroic that passes longer wavelength light and reflects shorter wavelength light, and then go towards the objective. The laser light irradiated to a sample on a glass coverslip in an incident angle (θ) larger than the critical angle, causing total internal reflection creating a standing evanescent wave of penetration depth (d_p) ~100 nm, as defined by **Equation 2.8**:[7]

$$d_p = \frac{\lambda}{4\pi}\sqrt{n_g^2\, sin^2\theta - n_s^2} \qquad \textbf{Equation 2.8}$$

where n_s and n_g are refractive indices of sample medium and the glass coverslip. This wave excites the sample and an emitted fluorescence is collected through the objective, passes through

the dichroic and an emission filter, and finally goes to an electron multiplying CCD (emCCD) for acquiring fluorescence image at a high signal to noise ratio.

The fluorescence microscope used in this research employed green (514 nm) and blue (488 nm) lasers as light sources, dichroic long-pass (DCLP) mirrors of 555 and 505 nm, a total internal reflection fluorescence (TIRF) objective lens with a numerical aperture of 1.49, and emission bandpass filters (580/40 and 525/50 nm, which passes light with a wavelength range of 580 ± 20 and 525 ± 25 nm, respectively).

Time transient data collected from every pixel in a fluorescence image was autocorrelated to obtain an autocorrelation function, $C(\tau)$, using **Equation 2.9**:

$$C(\tau) = \frac{<i(t)i(t+\tau)>}{<i(t)>^2} - 1 \qquad \textbf{Equation 2.9}$$

where $i(t)$ is the fluorescence intensity at time t, $i(t + \tau)$ is the time transient shifted by a time lag of τ, and the brackets (<>) represent the time averaged values. Subsequently, the resulting autocorrelation function was fitted with a one-dimensional Fickian diffusion model, **Equation 2.10**, on a LabView built software to determine the local D of dye molecules in an ONT.

$$C(\tau) = \frac{A}{\sqrt{1+\frac{\tau D_{local}}{\sigma^2}}} \times \frac{\exp[k(T-\tau)]-1}{k(T-\tau)} \qquad \textbf{Equation 2.10}$$

In this equation, A is the amplitude of the autocorrelation decay, σ^2 is the squared radius of detection region (305 nm for SRB and RB, 288 nm for R123), k is bleaching decay rate constant calculated by fitting the background fluorescence, and T is the total length of the video. The radius of the detection region, σ, corresponds to the square root of the sum of squares of pixel size and microscopic resolution.

2.7 References

1. Tompkins, H.G.; Irene E.A. In Handbook of Ellipsometry. *William Andrew Publishing, Springer*. **2005**.

2. Higgins, D.A. In Chemical Microscopy Lecture Notes. *Kansas State University*. **2019**.

3. Jalili, N.; Laxminarayana, K. A. Review of Atomic Force Microscopy Imaging Systems: Application to Molecular Metrology and Biological Sciences. *Mechatronics*. **2004**, *14*, 907-945.

4. Ito, T.; Ghimire, G. Electrochemical Applications of Microphase-Separated Block Copolymer Thin Films. *ChemElectroChem*. **2018**, *5*, 2937-2953.

5. Bard, A. J.; Faulkner, L. R. In Electrochemical Methods, Fundamentals and Applications, 2nd ed. *Wiley: New York*. **2001**.

6. Skoog, D.A.; Holler, F.J.; Crouch, S.R. Principle of Instrumental Analysis, 6th Ed. *Thomson Brooks/Cole*. **2007**.

7. Bruice, P.Y. In Organic Chemistry, 4th edition. *Prentice Hall*. **2003**.

8. Kisley, L.; Landes, C. F. Molecular Approaches to Chromatography Using Single Molecule Spectroscopy. *Analytical Chemistry*. **2015**, *87*, 83-98

9. Xu, H.; Nagasaka, S.; Kameta, N.; Masuda, M.; Ito, T.; Higgins, D. A. Imaging Fluorescence Correlation Spectroscopy Studies of Dye Diffusion in Self-Assembled Organic Nanotubes. *Phys. Chem. Chem. Phys.* **2016**, *18*, 16766-16774.

10. Ghimire, G.; Espinoza, R.; Xu, H.; Nagasaka, S.; Kameta, N.; Masuda, M.; Higgins, D. A.; Ito, T. Diffusion Behavior of Differently Charged Molecules in Self-Assembled Organic Nanotubes Studied Using Imaging Fluorescence Correlation Spectroscopy. *Langmuir*. **2019,** 35, 7783-7790.

11. Bag, N.; Wohland, T. Imaging Fluorescence Fluctuation Spectroscopy: New Tools for Quantitative Bioimaging. *Annu. Rev. Phys. Chem*. **2014**, *65*, 225-248.

Chapter 3 - Title Electron Propagation within Redox-Active Microdomains in Thin Films of Ferrocene-Containing Diblock Copolymers

Reproduced with permission from The American Chemical Society.

Published as: G. Ghimire, Y. Yi, M. A. Derylo, L. A. Baker, T. Ito, *Langmuir* **2015**, *31*, 12307-12314.

Contribution of Authors

YY and LAB initiated the project, and TI directed the overall project. YY synthesized all the block copolymers including relevant ^{1}H-NMR and gel permeation chromatography characterizations. LAB and MAD collected preliminary AFM images and electrochemical data of the block copolymer thin films, which were not included in this chapter. GG prepared all the thin film samples on gold substrates and collected all the ellipsometric, AFM and electrochemical data of the samples. TI and GG analyzed the electrochemical data.

3.1 Introduction

Block copolymers with ferrocene-containing polymer fragments have recently attracted considerable attention for formation of iron-containing microdomains of controlled nanoscale morphologies via microphase separation.[1-3] As with other block copolymers,[4-6] morphologies and dimensions of the resulting microdomains can be tuned by adjusting the molecular weight and volume fraction of block copolymer.[1,7] The microdomains were utilized as precursors for fabrication of iron-containing inorganic nanostructures upon degradation of the organic components.[8-13] In addition, the redox properties of the ferrocene moieties enabled design of

micellar aggregates for redox-tunable molecular encapsulation.[14-16] Furthermore, ferrocene-containing microdomains in monolithic thin films provided nanoscale charge pathways[17,18] for electrochemical mediation in enzyme-based glucose sensors[18,19] and for redox-controlled capture of biomolecules.[20] Electrochemical mediator layers formed from ferrocene-containing block copolymers showed high mechanical stability reinforced by the redox-inactive frameworks,[19] as with block copolymer-based polyelectrolytes explored for lithium-ion batteries.[21,22]

To take full advantage of the charge transport properties of ferrocene-containing microdomains, knowledge of the influence of polymer architecture and microdomain morphology on electrochemical behavior is crucial. Charge transport within these microdomains is attributable to electron self-exchange (hopping) reactions between adjacent ferrocene moieties, similar to ferrocene-containing homopolymers such as poly(vinylferrocene).[23-25] Electrode-supported thin films of redox homopolymers have been utilized for electrocatalysis[26,27] and electrochemical mediation in enzyme sensors.[28] Electron propagation efficiency in such a redox homopolymer film has been extensively investigated using electrochemical methods such as cyclic voltammetry (CV) and chronocoulometry (CC), and was quantitatively discussed based on an apparent diffusion coefficient (D_{ap}).[23-25] D_{ap} in redox polymer films depends on the concentration, electron transfer properties and dynamic properties of the redox moieties, and on migration of counter ions.[29] D_{ap} in poly(vinylferrocene) films (*ca.* 0.01~ 0.1 $\mu m^2/s$ at room temperature)[30,31] was much smaller than the diffusion coefficient of ferrocene molecules (*ca.* 10^3 $\mu m^2/s$),[32] reflecting the restricted motion of the redox moieties covalently linked to polymer frameworks and/or their limited ion permeability.[30,31] With repetitive measurements, poly(vinylferrocene) films exhibited gradual changes in voltammogram due to enhanced swelling upon the oxidation of the ferrocene moieties.[33,34]

In contrast to redox homopolymers, to the best of our knowledge, there is only one prior report that quantified electron propagation within ferrocene-containing block copolymer films.[35] In the reported work, CV was used to investigate the electrochemical properties of poly(ferrocenyldimethylsilane)-*block*-poly(dimethylsiloxane) (PFDMS-*b*-PDMS) in 0.1 M $LiClO_4$ solutions.[35] D_{ap} values in thin films of two PFDMS-*b*-PDMS with different PFDMS volume fractions (2.9 and 9.1 mol% PFDMS) were estimated to be *ca*. 10^{-4} $\mu m^2/s$.[35] Unfortunately, thin films prepared had spherical PFDMS microdomains, which prevented detailed studies of the effect of microdomain morphology on electron propagation. Effects of microdomain morphology on electron propagation have been investigated for other block copolymers, such as polystyrene-*block*-poly(4-vinylbenzyl diethylamine) (PS-*b*-PVEA) films that electrostatically incorporated $Fe(CN)_6^{4-}$ into the cationic PVEA microdomains.[36] Larger D_{ap} was observed in the block copolymer thin films as compared with PS-*random*-PVEA thin films, possibly due to the enhanced partitioning of $Fe(CN)_6^{4-}$ into the microdomains.[36] Electrostatic preconcentration of redox-active species into block copolymer microdomains provided a basis for highly sensitive spectroelectrochemical detection.[37] However, films with electrostatically accumulated redox species are not ideal for many applications, because the stability of redox activity is limited due to the release of the redox moieties into electrolyte solution.

This chapter describes electrochemical behavior of redox-active microdomains of different morphologies in thin films of ferrocene-containing diblock copolymers. Polystyrene-*block*-poly(2-(acryloyloxy)ethyl ferrocenecarboxylate) (PS-*b*-PAEFc; **Figure 1.3b**) with different PAEFc volume fractions (f_{PAEFc} = 0.47, 0.30 and 0.17) was used to prepare thin films with controlled microdomain morphologies and ellipsometric film thicknesses (20-160 nm). Microdomain formation in thin films of PS-*b*-PAEFc was verified from surface morphologies

obtained using atomic force microscopy (AFM). The electrochemical behavior of PS-*b*-PAEFc films in acetonitrile solution, including the effects of f_{PAEFc} and film thickness on voltammetric behavior and D_{ap}, was systematically investigated using CV and CC. This study reveals factors that control electrochemical behavior of redox-active block copolymer microdomains and is relevant to future applications such as electrochemical mediation in enzyme sensors, electrocatalysis, and redox-controlled molecular deposition.

3.2 Experimental Procedures

3.2.1 Chemicals and Materials

2-(Acryloyloxy)ethyl ferrocenecarboxylate) (AEFc) was synthesized according to the literature.[38] Its ^{1}H-NMR spectrum is shown in **Figure 3.1**. Styrene (99.9%, Aldrich) was purified by passing through a silica column and distilled with CaH_2 under vacuum. Copper (I) bromide (CuBr; 99.999%, Aldrich), copper (I) chloride (CuCl; ≥99.99%, Aldrich), *N*,*N*,*N*′,*N*′,*N*″-pentamethyldiethylenetriamine (PMDETA; 99%, Aldrich), ethyl α-bromoisobutyrate (98%, Aldrich), ferrocene (98%, Aldrich), tetrabutylammonium hexafluorophosphate (≥ 99%, $TBAPF_6$, Aldrich), tetrahydrofuran (≥ 99.0%, Aldrich), methanol (≥ 99.6%, Aldrich), acetonitrile (anhydrous, Alfa Aesar), and toluene (HPLC grade, Acros) were used without further purification. Gold-coated silicon wafers, which were prepared by sputtering 10 nm of Ti followed by 200 nm of Au onto Si (100) wafers, were purchased from LGA Thin Films (Foster City, CA).

3.2.2 Synthesis of PS-*b*-PAEFc

(a) Atom transfer radical polymerization (ATRP) of styrene: Styrene (12.5 mL, 109 mmol), CuBr (62.4 mg, 0.44 mmol) and ethyl α-bromoisobutyrate (63.8 μL, 0.44 mmol) were charged into a 50 mL Schlenk flask sealed with a rubber septum. After three cycles of freeze-

pump-thaw, degassed PMDETA (181 μL, 0.87 mmol) was injected into the flask through the rubber septum via a microsyringe. The solution was kept stirring under nitrogen at room temperature for 2 min. Then the flask was placed into an oil bath preset at 110 °C. The polymerization was quenched after 4 h by immersing the flask into liquid nitrogen. A small amount of polymer solution was taken out to calculate monomer conversion with ^{1}H-NMR (Varian VXR-400 Spectrometer). The remaining solution was diluted with THF and passed through a basic alumina column to remove the copper complex. Polystyrene was isolated by precipitating the THF solution in methanol and dried under vacuum at 40 °C overnight. It was re-dissolved in THF and precipitated into methanol. After filtration, the polymer was dried under vacuum at 45 °C overnight. The polymerization degree of polystyrene was calculated from the monomer conversion as 154, which was consistent to the molecular weight (M_n = 16K, PDI = 1.1) measured by gel permeation chromatography (GPC).

(b) ATRP of AEFc for the synthesis of PS-*b*-PAEFc: Scheme showing synthesis of PS-*b*-PAEFc is given in **Figure 3.2.** Polystyrene macroinitiator (0.3 g, 0.02 mmol), AEFc (0.5 g, 1.5 mmol), CuCl (2 mg, 0.02 mmol) and toluene (2 mL) were charged into a 10 mL Schlenk flask sealed with a rubber septum. The flask was subjected to three cycles of freeze-pump-thaw. Then, degassed PMDETA (3 μL, 0.02 mmol) was added via a microsyringe. The flask was put into an oil bath preset at 90 °C. The polymerization was stopped at different times to get different polymerization degrees of AEFc. Then the viscous solution was diluted with THF and passed through a short alumina column to remove copper complex. PS-*b*-PAEFc was isolated by precipitating the THF solution in methanol and dried under vacuum at 40 °C overnight. The diblock copolymer was re-dissolved in THF and precipitated in methanol. The dissolution-precipitation process was repeated until no residual monomer was detected by ^{1}H-NMR. The

polymerization degree of AEFc was calculated from a ^{1}H-NMR spectrum (**Figure 3.3**) by comparing the integration ratios of the phenyl ring of styrene unit (5H) at 6.0 – 7.3 ppm and the cyclopentadiene protons adjacent to carbonyl (2H, *a* in **Figure 3.3**) at 4.8 ppm.

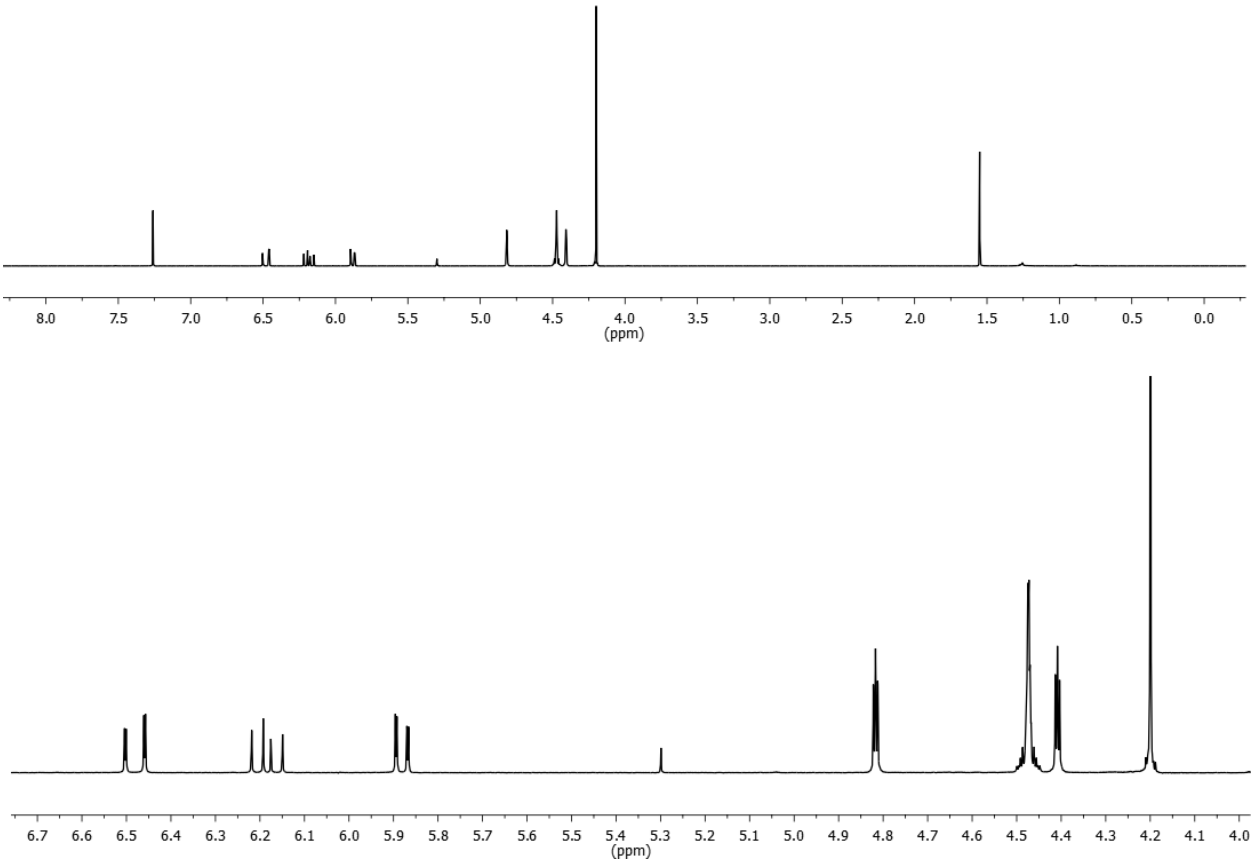

Figure 3.1 ^{1}H-NMR spectrum of AEFc in $CDCl_3$. The data was obtained by Dr. Yi. 2015, Copyright: American Chemical Society.

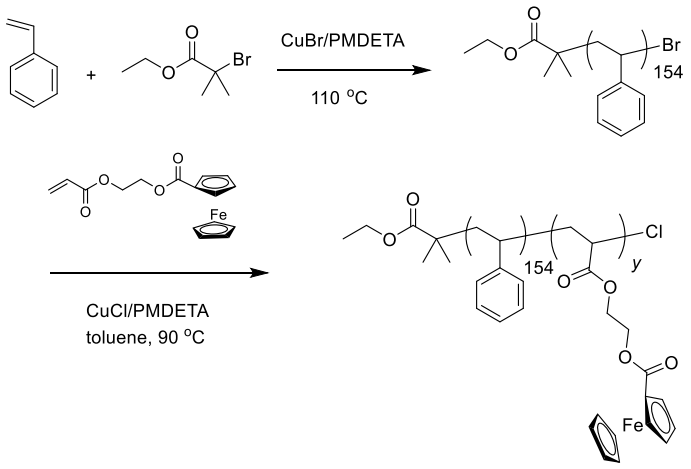

Figure 3.2 Synthetic scheme for PS-*b*-PAEFc. The length of the PAEFc chain was controlled by varying the polymerization time.

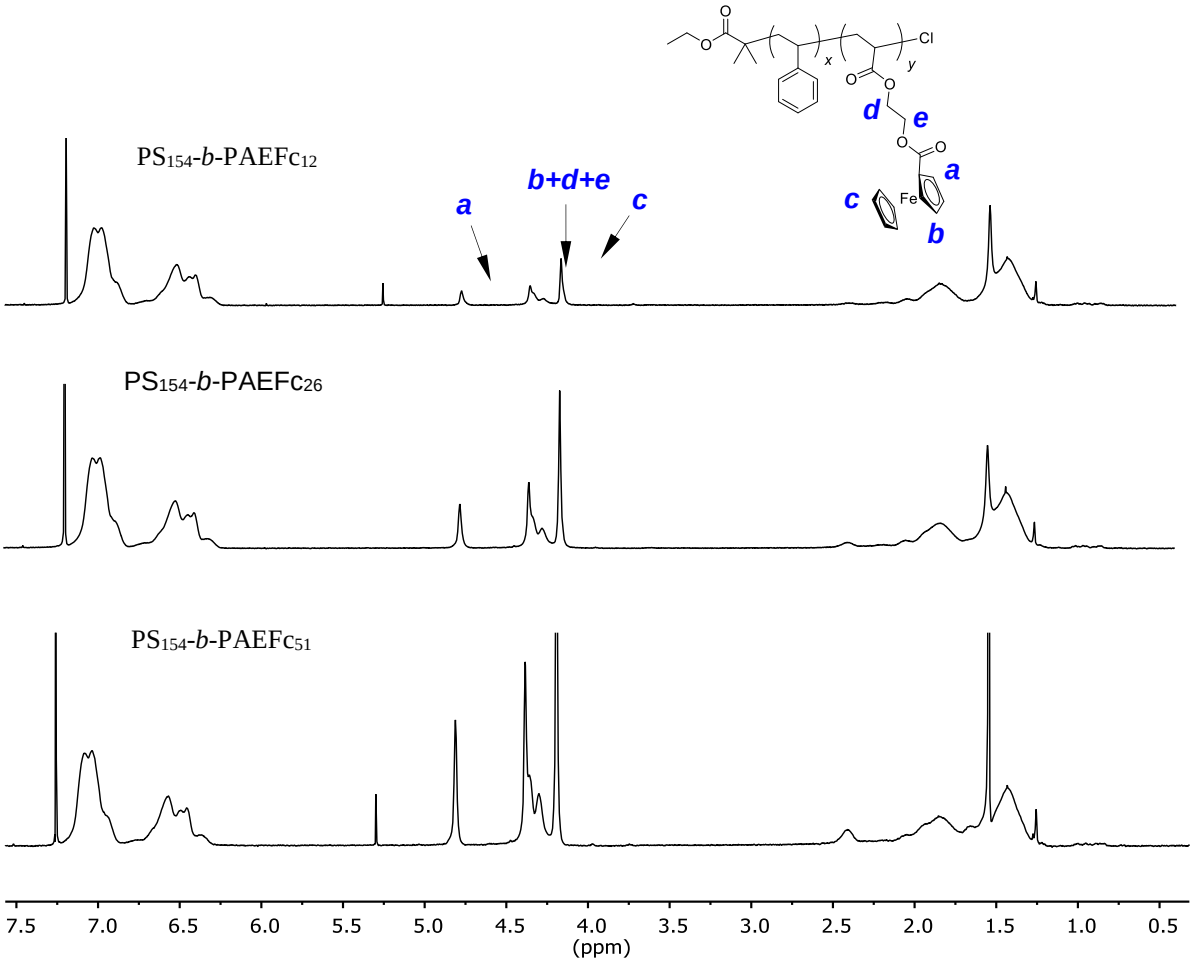

Figure 3.3 ^{1}H-NMR spectra of PS-*b*-PAEFc in $CDCl_3$. The data was collected by Dr. Yi. 2015, Copyright: American Chemical Society.

3.2.3 Preparation and Characterization of PS-*b*-PAEFc Films

Gold substrates were cleaned in a Novascan PSD-UVT UV-ozone system for 30 minutes. Thin films of PS-*b*-PAEFc were prepared on gold substrates via spin-coating (2000 rpm) from dilute toluene solution (0.5~2.5 wt%), followed by immediate drying under reduced pressure (*ca*. 75 torr) for 6-12 hours. The ellipsometric thicknesses of PS-*b*-PAEFc films were measured using a J. A. Woollam alpha-SE spectroscopic ellipsometer. AFM images (0.5 x 0.5 μm^2; 512 pixel x 512 pixel) of PS-*b*-PAEFc films were obtained by tapping/phase mode in air, using a Digital Instruments Multimode AFM with Nanoscope IIIa electronics. Tapping mode AFM probes from Aspire (cantilever length, 225 μm; force constant, 50 N/m; resonant frequency, 170 kHz) were cleaned in a Novascan PSD-UVT UV-ozone system to enhance the phase contrast.

3.2.4 Electrochemical Measurements

CV and CC measurements were performed in a CH Instruments model 700C electrochemical analyzer. Electrochemical measurements were carried out under an argon atmosphere in a three-electrode cell[39,40] with a Pt counter electrode and either a Ag/Ag^+ reference electrode (10 mM $AgNO_3$ and 0.1 M $TBAPF_6$ in acetonitrile) or a Ag wire quasi-reference electrode. A PS-*b*-PAEFc-coated gold substrate immobilized at the bottom of the cell with an O-ring (3.3 mm in radius) served as the working electrode. Cyclic voltammograms at different potential sweep rates (v = 0.01 ~ 1 V/s), followed by CC data, were recorded in acetonitrile with 0.1 M $TBAPF_6$ supporting electrolyte. CC was performed by applying potential steps from 0 to +0.6 V and then from +0.6 to 0 V (vs. Ag/Ag^+). The low and high potentials were sufficiently negative and positive with respect to the cathodic and anodic peak potentials, respectively. The potential of the reference electrode was frequently verified by measuring cyclic voltammograms of ferrocene (*ca*. 3 mM, in 0.1 M $TBAPF_6$ acetonitrile solution).

3.3 Results and Discussion

Previous studies of ferrocene-containing block copolymers focused on incorporation of redox centers in the polymer backbone.[1-3] However, the applicability of such main-chain block copolymers may be limited[41] because of cleavage reactions of the ferrocene-containing backbone.[42,43] With the advances in "living"/controlled radical polymerization, unprecedented polymers and block copolymers containing ferrocene in the side chain have been synthesized.[44] Here PS-*b*-PAEFc, with ferrocene moieties in the side chains (**Figure 1.3b**), was synthesized by sequential ATRP (see Experimental) and studied to circumvent cleavage of the main chain. The synthesis and electrochemical properties of PAEFc homopolymers[38] and PAEFc-grafted polymers[45,46] have been reported. However, there has been no report on the microphase separation and electrochemical characterization of PS-*b*-PAEFc. We first verified microphase separation in thin films of PS-*b*-PAEFc with AFM.

Figure 3.4 shows AFM height (left) and phase (right) images of PS-*b*-PAEFc films with smaller (21-36 nm) and larger (97-146 nm) ellipsometric thicknesses. Films of PS_{154}-*b*-$PAEFc_{51}$ and PS_{154}-*b*-$PAEFc_{26}$ (**Figure 3.4a-d**) exhibited nanoscale surface structures of relative uniform widths/diameters. Protruded regions in the height images, which exhibited larger phase changes in the corresponding phase images, were assigned to PAEFc microdomains, because it is apparent that in the phase images the PAEFc microdomains were dispersed in the continuous PS matrix. Furthermore, the PAEFc microdomains occupied larger area in films of PS_{154}-*b*-$PAEFc_{51}$ (**Figure 3.4a, b**) as compared with films of PS_{154}-*b*-$PAEFc_{26}$ (**Figure 3.4c, d**). The shapes of these regions at the thinner films (**Figure 3.4a, c**) suggested lamellar and cylindrical PAEFc microdomains in the films of PS_{154}-*b*-$PAEFc_{51}$ and PS_{154}-*b*-$PAEFc_{26}$, as expected from f_{PAEFc} (= 0.47 and 0.30; **Table 3.1**) and the well-established phase diagram of diblock copolymers.[4-6] The

width of the lamellar microdomains (*ca*. 30 nm) was larger than the diameter of the cylindrical microdomains (*ca*. 20 nm), reflecting the longer PAEFc chains in PS_{154}-*b*-$PAEFc_{51}$. These PAEFc microdomains were oriented vertically, which was possibly induced by the nanoscale roughness of the sputter-coated gold susbtrate[47] and/or by solvent evaporation after spin-coating.[5] In contrast, microdomains were not obvious on the surface of the PS_{154}-*b*-$PAEFc_{12}$ films (**Figure 3.4e,f**), likely because the polymer (f_{PAEFc} = 0.17) afforded spherical microdomains that were buried inside the PS matrix.

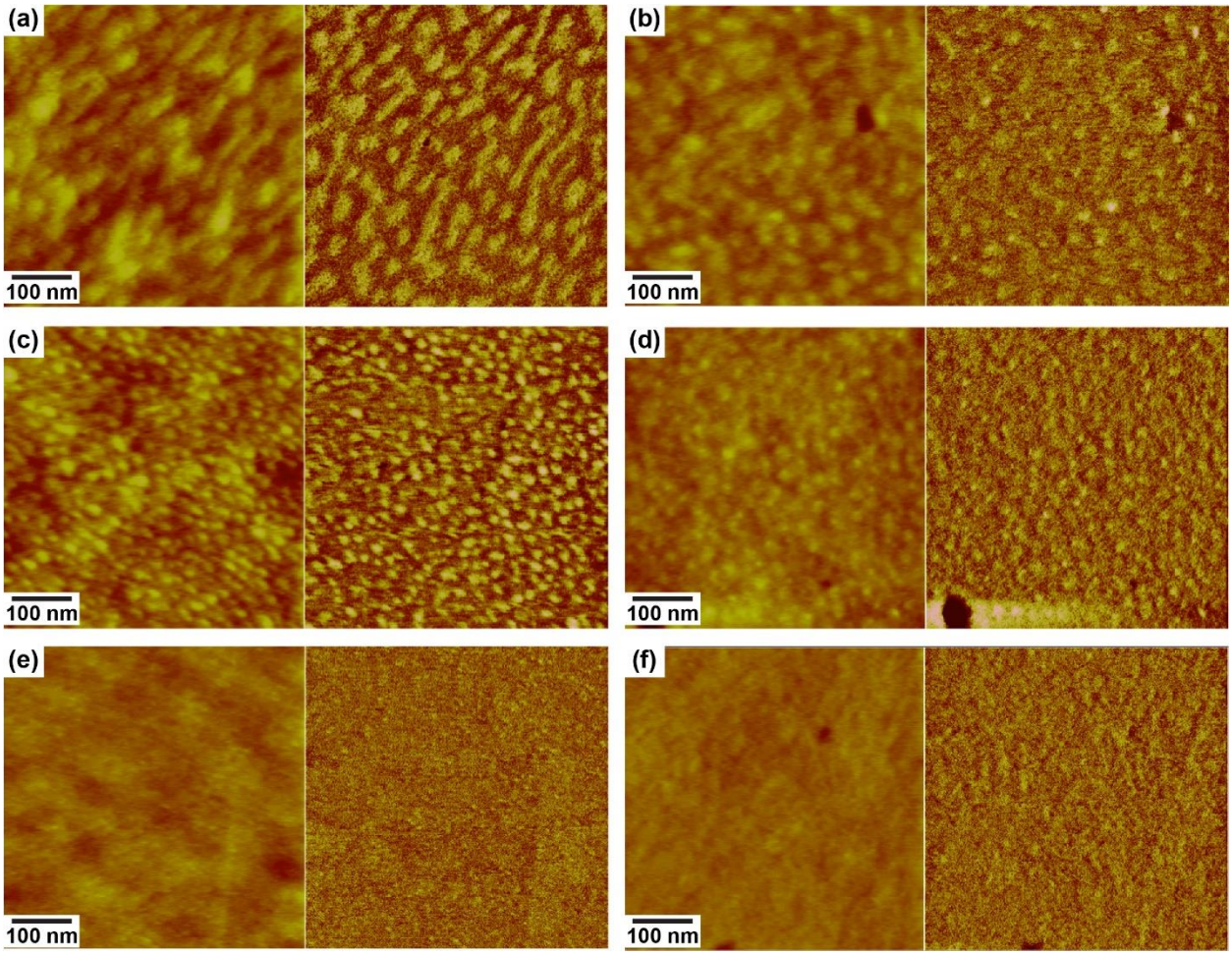

Figure 3.4 AFM height (left, Δz = 10 nm) and phase (right) images (0.5 x 0.5 μm^2) of thin films of **(a)** PS_{154}-*b*-$PAEFc_{51}$ (21 nm thick), **(b)** PS_{154}-*b*-$PAEFc_{51}$ (97 nm thick), **(c)** PS_{154}-*b*-$PAEFc_{26}$ (29 nm thick), **(d)** PS_{154}-*b*-$PAEFc_{26}$ (136 nm thick), **(e)** PS_{154}-*b*-$PAEFc_{12}$ (36 nm thick) and **(f)** PS_{154}-*b*-$PAEFc_{12}$ (146 nm thick) on planar gold substrates. The average and standard deviation

of 22 microdomain widths obtained from two separate images are **(a)** 31 ± 7 (nm), **(b)** 27 ± 7 (nm), **(c)** 22 ± 4 (nm) and **(d)** 20 ± 4 (nm). 2015, Copyright: American Chemical Society.

Figure 3.5 shows the scan-rate dependence of cyclic voltammograms of thinner (23-25 nm) and thicker (91-117 nm) PS-*b*-PAEFc films measured in 0.1 M $TBAPF_6$/acetonitrile. Faradaic peak currents measured at the thinner films were larger with increasing f_{PAEFc} (**Figure 3.5a, c, e**), as qualitatively expected from the electrode reactions of ferrocene moieties in the PAEFc microdomains. PAEFc microdomains provided similar redox environment for ferrocene moieties, as indicated by the similar redox potential ($E^0 \approx +0.29$ V vs. Fc^+/Fc, **Table 3.1**) regardless of f_{PAEFc} and film thickness (**Figure 3.6a**). For PS_{154}-*b*-$PAEFc_{51}$ and PS_{154}-*b*-$PAEFc_{26}$, the larger faradaic peak currents were observed at the thicker films (**Figure 3.5a, b** and **Figure 3.5c, d**). The thinner films exhibited voltammograms of surface-confined species, as indicated by the CV peak separation ($\Delta E_p = E_{p,anodic} - E_{p,cathodic}$) smaller than 58 mV at slower v (**Figure 3.5a, c**) and by the slopes of log i_p–log v plots close to 1 over the entire v range shown in **Figure 3.6b** (black open circles and red open squares).[32] ΔE_p was larger at the faster v, probably due to the slow electron transfer kinetics at the electrode-film interface and/or between adjacent ferrocene moieties. Thicker films (**Figure 3.5b, d**) afforded diffusion-controlled voltammograms at faster v, as shown by the transition of the slopes of the log i_p–log v plots from 1 to 0.5 at $v \geq 0.2$ V/s (black filled circles and red filled squares in **Figure 3.6b**). The transition was observed in the range of 0.1 ~ 0.5 V/s and tended to be at the slower v for the thicker films. The latter observation suggests that electron propagation took place through ferrocene moieties closer to the electrode at the short timescale and proceeded in a percolative manner. In contrast, the faradaic peak currents were independent of thickness for the films of PS_{154}-*b*-$PAEFc_{12}$ (**Figure 3.5e, f**), implying that electron propagation in these films occurred only in PAEFc microdomains directly contacted to the electrode. Indeed, the PS_{154}-*b*-$PAEFc_{12}$ films exhibited

voltammograms of surface-confined species, as indicated by the slopes of log i_p–log v plots close to 1 (blue open and filled triangles in **Figure 3.6b**). Similar voltammograms were observed at indium tin oxide electrodes grafted by ferrocene-containing diblock copolymer brushes via surface-initiated ATRP.[48]

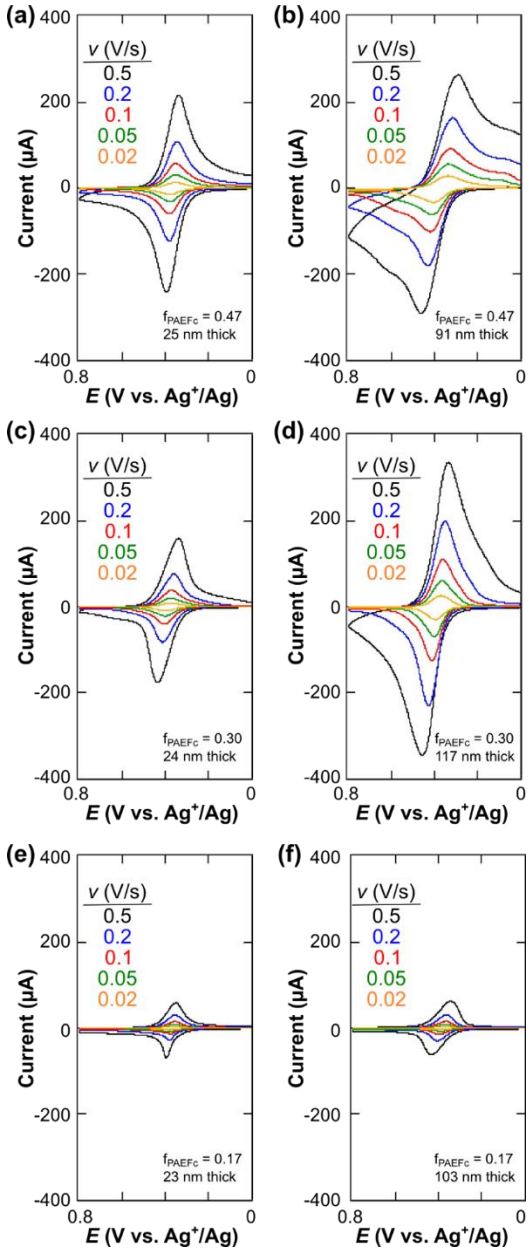

Figure 3.5 Cyclic voltammograms measured in 0.1 M $TBAPF_6$/acetonitrile at different v for thin films of **(a, b)** PS_{154}-*b*-$PAEFc_{51}$, **(c,d)** PS_{154}-*b*-$PAEFc_{26}$ and **(e,f)** PS_{154}-*b*-$PAEFc_{12}$. The ellipsometric thickness of each film was **(a)** 25 nm, **(b)** 91 nm, **(c)** 24 nm, **(d)** 117 nm, **(e)** 23 nm and **(f)** 103 nm. Note that potential was plotted with respect to a Ag^+/Ag reference electrode

(E(Ag^+/Ag) = -0.089 ± 0.006 V vs. Fc^+/Fc; N = 16). 2015, Copyright: American Chemical Society.

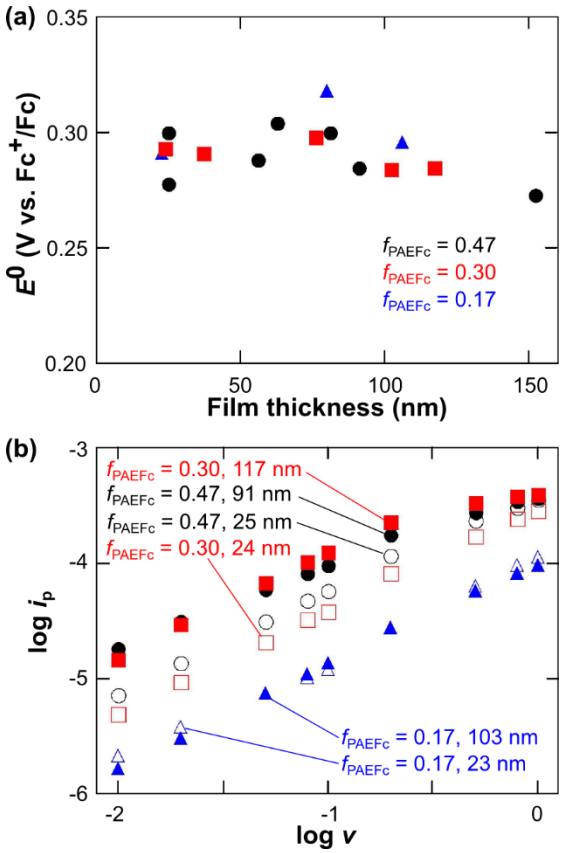

Figure 3.6 (a) Effects of film thickness on E_0 (V vs. Fc^+/Fc) obtained from the anodic and cathodic peak potentials of cyclic voltammograms (v = 0.1 V/s) in 0.1 M $TBAPF_6$/acetonitrile. **(b)** Plots of log i_p vs. log v (i_p: anodic peak current) obtained from the thin PS-*b*-PAEFc films in **Figure 3.5**. Data for PS_{154}-*b*-$PAEFc_{51}$, PS_{154}-*b*-$PAEFc_{26}$ and PS_{154}-*b*-$PAEFc_{12}$ are shown in black circles, red squares and blue triangles, respectively. 2015, Copyright: American Chemical Society.

Table 3.1. E_0 and D_{ap} Obtained for Gold-Supported PS-*b*-PAEFc Films in 0.1 M $TBAPF_6$/acetonitrile.

Polymer	f_{PAEFc}[a]	E^0 (V vs. Fc^+/Fc)[b]	D_{ap} ($\mu m^2/s$)[c]
PS_{154}-*b*-$PAEFc_{51}$	0.47	0.290 ± 0.012 (N = 7)	(1.89 ± 1.35) x 10^{-3} (N = 6)
PS_{154}-*b*-$PAEFc_{26}$	0.30	0.290 ± 0.006 (N = 5)	(1.85 ± 1.67) x 10^{-3} (N = 7)
PS_{154}-*b*-$PAEFc_{12}$	0.17	0.302 ± 0.014 (N = 3)	–[d]

[a] Calculated from ρ_{PS} = 1.05 (g/cm^3) and ρ_{PAEFc} = 1.25 (g/cm^3). The latter was estimated from the density of polyvinylferrocene.[52] [b] Average ± standard deviation for the second or third sweep (v = 0.1 V/s) that was measured at PS-*b*-PAEFc films (23-160 nm thick) using a Ag^+/Ag reference electrode. The number of samples examined is shown in parenthesis. [c] Average ± standard deviation obtained from CC data for PS-*b*-PAEFc films with thicknesses of ≥ 50 nm at t = 0.1 ~ 0.15 sec. The number of samples examined is shown in parenthesis. [d] Not calculated because diffusion-controlled voltammograms were not observed regardless of film thickness.

Of note, voltammograms of the 91-nm thick film of PS_{154}-*b*-$PAEFc_{51}$ (**Figure 3.5b**) showed additional anodic and cathodic shoulders around +0.6 V and +0.1 V, respectively. Shoulders corresponding to them were less significant at the 117-nm thick film of PS_{154}-*b*-$PAEFc_{26}$ (**Figure 3.5d**) and were not observed at the 103-nm thick film of PS_{154}-*b*-$PAEFc_{12}$ (**Figure 3.5f**). These shoulders were attributable to the swelling of the PAEFc microdomains enhanced by the oxidation of the ferrocene moieties, as described previously for poly(vinylferrocene) films.[30] These observations indicate that PAEFc microdomains of PS-*b*-PAEFc with smaller fPAEFc were more stable against solvent-induced swelling due to the presence of redox-inert PS frameworks. Similar stability improvement was shown in polyelectrolytes of solid-state lithium-ion batteries based on block copolymers composed of ion-conductive and mechanically stabilizing components.[21,22]

CC was employed to quantify the fraction of active ferrocene moieties and D_{ap} within PAEFc microdomains. **Figure 3.7** shows typical CC data measured at PS-*b*-PAEFc films of different f_{PAEFc} and thicknesses. Maximum anodic charge ($Q_{a,max}$) was larger for the thicker films of PS_{154}-*b*- $PAEFc_{51}$ (**Figure 3.7a**) and PS_{154}-*b*-$PAEFc_{26}$ (**Figure 3.7b**) than ≈ 25 nm thick films, whereas $Q_{a,max}$ was independent of film thickness for PS_{154}-*b*-$PAEFc_{12}$ (**Figure 3.7c**). These trends could be clearly found from the relationship between $Q_{a,max}$ and film thickness, as summarized in **Figure 3.8a**. Importantly, not all the ferrocene moieties were redox-active. Experimental charges ($Q_{a,max}$, individual points) were smaller than theoretical charges (Q_{theo},

solid line) calculated from the total number of ferrocene moieties in the films. Deviation of $Q_{a,max}$ from Q_{theo} was smaller for thinner films, which supports the assertation that higher ratios of PAEFc microdomains could electrically communicate with the electrode in the thinner films. The thickness-independent $Q_{a,max}$ for PS_{154}-*b*-$PAEFc_{12}$ (blue triangles in **Figure 3.8a**) was consistent to the observation of thickness independent voltammograms as shown in **Figure 3.5e,f**.

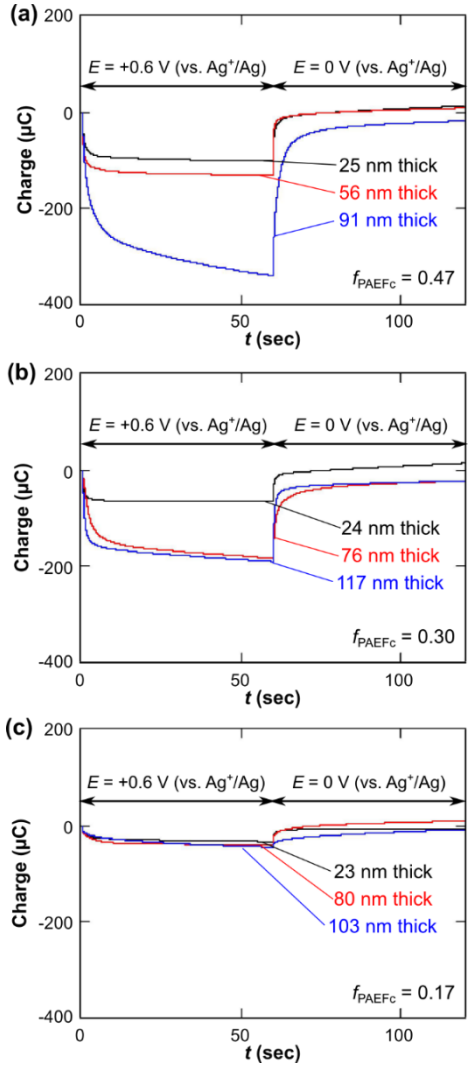

Figure 3.7 CC data measured in 0.1 M $TBAPF_6$/acetonitrile of thin films of different thicknesses for **(a)** PS_{154}-*b*-$PAEFc_{51}$, **(b)** PS_{154}-*b*-$PAEFc_{26}$, and **(c)** PS_{154}-*b*-$PAEFc_{12}$. The applied electrode potential was 0 V (vs. Ag^+/Ag) at t (s) < 0, +0.6 V (vs. Ag^+/Ag) at 0 ≤ t (s) < 60, and 0 V (vs. Ag^+/Ag) at 60 ≤ t (s) ≤ 120. 2015, Copyright: American Chemical Society.

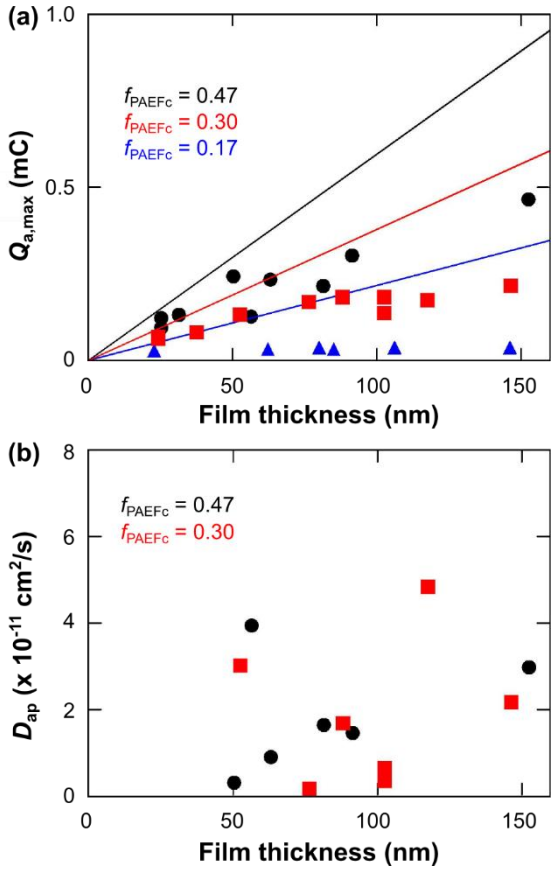

Figure 3.8 Effects of film thickness on **(a)** $Q_{a,max}$ and **(b)** D_{ap} measured from CC data in 0.1 M $TBAPF_6$/acetonitrile. Data for PS_{154}-*b*-$PAEFc_{51}$, PS_{154}-*b*-$PAEFc_{26}$ and PS_{154}-*b*-$PAEFc_{12}$ are shown in black circles, red squares and blue triangles, respectively. In **(a)**, the solid lines indicate anodic charges that should be obtained when all the ferrocene moieties in the films are oxidized (Q_{theo}). 2015, Copyright: American Chemical Society.

These electrochemical results could be reasonably explained by the models shown in **Scheme 3.1**. Electrons could propagate only through PAEFc microdomains that could electrically communicate with the underlying electrode.[48] Lamella and cylindrical PAEFc microdomains in PS_{154}-*b*-$PAEFc_{51}$ and PS_{154}-*b*-$PAEFc_{26}$ films could extend from the electrode surface to the film-solution interface (**Scheme 3.1a**), leading to the observation of the thickness-dependent increases in $Q_{a,max}$ (**Figure 3.8a**). However, the ratio of the microdomains penetrating across a film decreased as film thickness increased due to the absence of a strong external driving force required for vertical microdomain alignment.[5,47,49] This resulted in a larger

deviation between $Q_{a,max}$ and Q_{theo} at the thicker films (*vide supra*). On the other hand, spherical PAEFc microdomains in PS_{154}-*b*-$PAEFc_{12}$ films were electrically isolated and could not exchange electrons with adjacent microdomains (**Scheme 3.1b**). As a result, only PAEFc microdomains in direct contact with the electrode could be involved in the electrode reaction, giving the thickness-independent $Q_{a,max}$ (**Figure 3.8a**). The counter anions required for the oxidation of buried PAEFc microdomains could migrate through the PS matrix swollen by acetonitrile.[50]

Scheme 3.1. Estimated Microdomain Morphologies in the Thicker PS-*b*-PAEFc Films. 2015, Copyright: American Chemical Society.

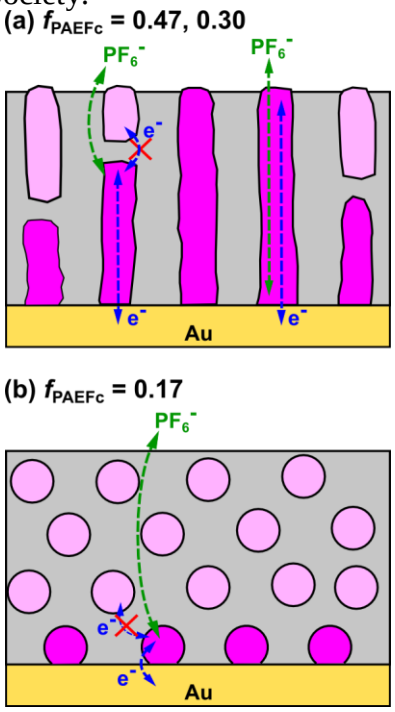

D_{ap} for the oxidation of PAEFc microdomains was determined from the CC data[51] by the following **Equation 2.5**.[32] D_{ap} was determined from the slope of a Q–$t^{1/2}$ plot for relatively thick PS_{154}-*b*-$PAEFc_{51}$ and PS_{154}-*b*-$PAEFc_{26}$ films ($\geq$ 50 nm) at a timescale (i.e., t = 0.1 ~ 0.15 s) that gives diffusion-controlled voltammograms with negligible influence of the capacitive charge. As

summarized in **Table 3.1**, D_{ap} was similar for PS_{154}-*b*-$PAEFc_{51}$ and PS_{154}-*b*-$PAEFc_{26}$. The fairly small D_{ap} ($\approx 2 \times 10^{-3}$ $\mu m^2/s$) reflected inefficient electron self-exchange reaction within the PAEFc microdomains and/or limited counter ion migration through the acetonitrile-swollen microdomains. For measurements here, the use of the ellipsometric thickness of dried films as *d* could lead to the underestimation of D_{ap} because the actual films used for electrochemical measurements should be thicker due to the acetonitrile-induced swelling (*vide supra*). However, even with this caveat, there was no clear thickness dependence of D_{ap} (**Figure 8b**). These results reflect the similarity in the composition of PAEFc microdomains regardless of film thickness and f_{PAEFc}.

3.4 Conclusion

This study revealed the electrochemical properties of ferrocene-containing microdomains of thin PS-*b*-PAEFc films in 0.1 M $TBAPF_6$/acetonitrile. Electron propagation across ferrocene moieties in the PAEFc microdomains took place via electron hopping accompanied with counter ion migration through the solvent-swollen films, as with ferrocene-containing homopolymer films. The spherical PAEFc microdomains formed from PS_{154}-*b*-$PAEFc_{12}$ were buried within PS matrix, and thus may not be suitable for applications based on their redox properties. In contrast, there were lamellar and cylindrical PAEFc microdomains formed in the thin films of PS_{154}-*b*-$PAEFc_{51}$ and PS_{154}-*b*-$PAEFc_{26}$ that penetrated across the films. No clear dependence of microdomain morphology and film thickness on D_{ap} was observed, likely because the concentration, electron transfer properties and dynamic properties of the ferrocene moieties were similar in these microdomains. Considering the higher stability against solvent-induced swelling due to the redox-inert PS matrix, cylindrical PAEFc microdomains will be better suited for electrochemical applications. However, the PS-*b*-PAEFc films prepared in this study exhibited a

decrease in the ratio of penetrating microdomains with increasing film thickness. For the future applications, the vertical orientation of cylindrical microdomains needs to be improved, for example via solvent vapor annealing,[5] to maximize the activity of the redox-active microdomains.

3.5 References

(1) Rider, D. A.; Manners, I. Synthesis, Self-Assembly, and Applications of Polyferrocenylsilane Block Copolymers. *Polym. Rev.* **2007**, *47*, 165-195.

(2) Ramanathan, M.; Tseng, Y.C.; Ariga, K.; Darling, S. B. Emerging Trends in Metal Containing Block Copolymers: Synthesis, Self-Assembly, and Nanomanufacturing Applications. *J. Mater. Chem. C* **2013**, *1*, 2080-2091.

(3) Zhou, J.; Whittell, G. R.; Manners, I. Metalloblock Copolymers: New Functional Nanomaterials. *Macromolecules* **2014**, *47*, 3529-3543.

(4) Bates, F. S.; Fredrickson, G. H. Block Copolymers - Designer Soft Materials. *Phys. Today* **1999**, *52* (2), 32-38.

(5) Sinturel, C.; Vayer, M.; Morris, M.; Hillmyer, M. A. Solvent Vapor Annealing of Block Polymer Thin Films. *Macromolecules* **2013**, *46*, 5399-5415.

(6) Ito, T. Block Copolymer-Derived Monolithic Polymer Films and Membranes Comprising Self-Organized Cylindrical Nanopores for Chemical Sensing and Separations. *Chem.–Asian J.* **2014**, *9*, 2708-2718.

(7) Lammertink, R. G. H.; Hempenius, M. A.; Thomas, E. L.; Vancso, G. J. Periodic Organic–Organometallic Microdomain Structures in Poly(styrene-*block*-ferrocenyldimethylsilane)

Copolymers and Blends with Corresponding Homopolymers. *J. Polym. Sci. Part B: Polym. Phys.* **1999**, *37*, 1009-1021.

(8) Temple, K.; Kulbaba, K.; Power-Billard, K. N.; Manners, I.; Leach, K. A.; Xu, T.; Russell, T. P.; Hawker, C. J. Spontaneous Vertical Ordering and Pyrolytic Formation of Nanoscopic Ceramic Patterns from Poly(styrene-*b*-ferrocenylsilane). *Adv. Mater.* **2003**, *15*, 297-300.

(9) Lastella, S.; Jung, Y. J.; Yang, H.; Vajtai, R.; Ajayan, P. M.; Ryu, C. Y.; Rider, D. A.; Manners, I. Density Control of Single-Walled Carbon Nanotubes Using Patterned Iron Nanoparticle Catalysts Derived from Phase-Separated Thin Films of a Polyferrocene Block Copolymer. *J. Mater. Chem.* **2004**, *14*, 1791-1794.

(10) Hinderling, C.; Keles, Y.; Stockli, T.; Knapp, H. F.; de los Arcos, T.; Oelhafen, P.; Korczagin, I.; Hempenius, M. A.; Vancso, G. J.; Pugin, R.; Heinzelmann, H. Organometallic Block Copolymers as Catalyst Precursors for Templated Carbon Nanotube Growth. *Adv. Mater.* **2004**, *16*, 876-879.

(11) Lu, J. Q.; Kopley, T. E.; Moll, N.; Roitman, D.; Chamberlin, D.; Fu, Q.; Liu, J.; Russell, T. P.; Rider, D. A.; Manners, I.; Winnik, M. A. High-Quality Single-Walled Carbon Nanotubes with Small Diameter, Controlled Density, and Ordered Locations Using a Polyferrocenylsilane Block Copolymer Catalyst Precursor. *Chem. Mater.* **2005**, *17*, 2227-2231.

(12) Rider, D. A.; Liu, K.; Eloi, J.-C.; Vanderark, L.; Yang, L.; Wang, J.-Y.; Grozea, D.; Lu, Z.-H.; Russell, T. P.; Manners, I. Nanostructured Magnetic Thin Films from Organometallic Block Copolymers: Pyrolysis of Self-Assembled Polystyrene-*block*-poly(ferrocenylethylmethylsilane). *ACS Nano* **2008**, *2*, 263-270.

(13) Hardy, C. G.; Ren, L.; Ma, S.; Tang, C. Self-Assembly of Well-Defined Ferrocene Triblock Copolymers and Their Template Synthesis of Ordered Iron Oxide Nanoparticles. *Chem. Commun.* **2013**, *49*, 4373-4375.

(14) Rider, D. A.; Winnik, M. A.; Manners, I. Redox-Controlled Micellization of Organometallic Block Copolymers. *Chem. Commun.* **2007**, 4483-4485.

(15) Eloi, J.-C.; Rider, D. A.; Cambridge, G.; Whittell, G. R.; Winnik, M. A.; Manners, I. Stimulus-Responsive Self-Assembly: Reversible, Redox-Controlled Micellization of Polyferrocenylsilane Diblock Copolymers. *J. Am. Chem. Soc.* **2011**, *133*, 8903-8913.

(16) Power-Billard, K. N.; Spontak, R. J.; Manners, I. Redox-Active Organometallic Vesicles: Aqueous Self-Assembly of a Diblock Copolymer with a Hydrophilic Polyferrocenylsilane Polyelectrolyte Block. *Angew. Chem. Int. Ed.* **2004**, *43*, 1260-1264.

(17) Li, J. K.; Zou, S.; Rider, D. A.; Manners, I.; Walker, G. C. Differential Conductivity in Self-Assembled Nanodomains of a Diblock Copolymer Using Polystyrene-*block*-Poly(ferrocenylethylmethylsilane). *Adv. Mater.* **2008**, *20*, 1989-1993.

(18) Lee, J.; Ahn, H.; Choi, I.; Boese, M.; Park, M. J. Enhanced Charge Transport in Enzyme-Wired Organometallic Block Copolymers for Bioenergy and Biosensors. *Macromolecules* **2012**, *45*, 3121-3128.

(19) Armada, M.P.G.; Losada, J.; Lopez-Villanueva, F. J.; Frey, H.; Alonso, B.; Casado, C. M. Electrochemical and Bioelectrocatalytical Properties of Novel Block-Copolymers Containing Interacting Ferrocenyl Units. *J. Organomet. Chem.* **2008**, *693*, 2803-2811.

(20) Eloi, J.-C.; Ward Jones, S. E.; Poor, V.; Okuda, M.; Gwyther, J.; Schwarzacher, W. Electrochemically Triggered Selective Adsorption of Biotemplated Nanoparticles on Self-

Assembled Organometallic Diblock Copolymer Thin Films. *Adv. Funct. Mater.* **2012**, *22*, 3273-3278.

(21) Gray, F. M.; MacCallum, J. R.; Vincent, C. A.; Giles, J. R. M. Novel Polymer Electrolytes Based on ABA Block Copolymers. *Macromolecules* **1988**, *21*, 392-397.

(22) Soo, P. P.; Huang, B.; Jang, Y.-I.; Chiang, Y.-M.; Sadoway, D. R.; Mayes, A. M. Rubbery Block Copolymer Electrolytes for Solid-State Rechargeable Lithium Batteries. *J. Electrochem. Soc.* **1999**, *146*, 32-37.

(23) Murray, R. W. Polymer Modification of Electrodes. *Annu. Rev. Mater. Sci.* **1984**, *14*, 145-169.

(24) Majda, M.: Dynamics of Electron Transport in Polymeric Assemblies of Redox Centers. In *Molecular Design of Electrode Surfaces*; Murray, R. W., Ed.; John Wiley & Sons: New York, 1992; pp 159-206.

(25) Terrill, R. H.; Murray, R. W.: Electron Hopping Transport in Electrochemically Active, Molecular Mixed Valent Materials. In *Molecular Electronics: A 'Chemistry for the 21st Century' Monograph*; Jortner, J., Ratner, M., Eds.; Blackwell Science: Malden, MA, 1997; pp 215-239.

(26) Andrieux, C. P.; Saveant, J.-M.: Catalysis at Redox Polymer Coated Electrodes. In *Molecular Design of Electrode Surfaces*; Murray, R. W., Ed.; John Wiley & Sons: New York, 1992; pp 207-270.

(27) Mao, X.; Tian, W.; Wu, J.; Rutledge, G. C.; Hatton, T. A. Electrochemically Responsive Heterogeneous Catalysis for Controlling Reaction Kinetics. *J. Am. Chem. Soc.* **2015**, *137*, 1348-1355.

(28) Wilson, G. S.; Hu, Y. Enzyme Based Biosensors for in Vivo Measurements. *Chem. Rev.* **2000**, *100*, 2693-2704.

(29) Blauch, D. N.; Saveant, J.-M. Dynamics of Electron Hopping in Assemblies of Redox Centers. Percolation and Diffusion. *J. Am. Chem. Soc.* **1992**, *114*, 3323-3332.

(30) Peerce, P. J.; Bard, A. J. Polymer-Films on Electrodes Part III. Digital-Simulation Model for Cyclic Voltammetry of Electroactive Polymer Film and Electrochemistry of Poly(vinylferrocene) on Platinum. *J. Electroanal. Chem.* **1980**, *114*, 89-115.

(31) Hunter, T. B.; Tyler, P. S.; Smyrl, W. H.; White, H. S. Impedance Analysis of Poly(vinylferrocene) Films. The Dependence of Diffusional Charge Transport and Exchange Current-Density on Polymer Oxidation-State. *J. Electrochem. Soc.* **1987**, *134*, 2198-2204.

(32) Bard, A. J.; Faulkner, L. R.: *Electrochemical Methods, Fundamentals and Applications*; Second Edition ed.; Wiley: New York, 2001.

(33) Daum, P.; Murray, R. W. Charge-Transfer Diffusion Rates and Activity Relationships during Oxidation and Reduction of Plasma-Polymerized Vinylferrocene Films. *J. Phys. Chem.* **1981**, *85*, 389-396.

(34) Varineau, P. T.; Buttry, D. A. Applications of the Quartz Crystal Microbalance to Electrochemistry. Measurement of Ion and Solvent Populations in Thin Films of Poly(vinylferrocene) as Functions of Redox State. *J. Phys. Chem.* **1987**, *91*, 1292-1295.

(35) Chen, T.; Wang, L.; Jiang, G.; Wang, J.; Dong, X.; Wang, X.; Zhou, J.; Wang, C.; Wang, W. Electrochemical Behavior of Poly(ferrocenyldimethylsilane-*b*-dimethylsiloxane) Films. *J. Phys. Chem. B* **2005**, *109*, 4624-4630.

(36) Sumi, K.; Anson, F. C. Electron-Transfer to Anionic Reactants Incorporated within Polycationic Coatings on Glassy-Carbon Electrodes. Comparison of Random and Block Copolymers. *J. Phys. Chem.* **1986**, *90*, 3845-3850.

(37) Pantelic, N.; Andria, S. E.; Heineman, W. R.; Seliskar, C. J. Characterization of Partially Sulfonated Polystyrene-block-poly(ethylene-ran-butylene)-block-polystyrene Thin Films for Spectroelectrochemical Sensing. *Anal. Chem.* **2009**, *81*, 6756-6764.

(38) Hardy, C. G.; Ren, L.; Tamboue, T. C.; Tang, C. Side-Chain Ferrocene-Containing (Meth)acrylate Polymers: Synthesis and Properties. *J. Polym. Sci. Part A: Polym. Chem.* **2011**, *49*, 1409-1420.

(39) Li, F.; Pandey, B.; Ito, T. Linker-Based Control of Electron Propagation through Ferrocene Moieties Covalently Anchored onto Insulator-Based Nanopores Derived from a Polystyrene-Poly(methylmethacrylate) Diblock Copolymer. *Langmuir* **2012**, *28*, 16496-16500.

(40) Li, F.; Ito, T. Complexation-Induced Control of Electron Propagation Based on Bounded Diffusion through Nanopore-Tethered Ferrocenes. *J. Am. Chem. Soc.* **2013**, *135*, 16260-16263.

(41) Gallei, M. The Renaissance of Side-Chain Ferrocene-Containing Polymers: Scope and Limitations of Vinylferrocene and Ferrocenyl Methacrylates. *Macromol. Chem. Phys.* **2014**, *215*, 699-704.

(42) Cyr, P. W.; Tzolov, M.; Manners, I.; Sargent, E. H. Photooxidation and Photoconductivity of Polyferrocenylsilane Thin Films. *Macromol. Chem. Phys.* **2003**, *204*, 915-921.

(43) Giannotti, M. I.; Lv, H.; Ma, Y.; Steenvoorden, M. P.; Overweg, A. R.; Roerdink, M.; Hempenius, M. A.; Vancso, G. J. Stimulus Responsive Poly(ferrocenylsilanes): Redox Chemistry of Iron in the Main Chain. *J. Inorg. Organomet. Polym. Mater.* **2005**, *15*, 527-540.

(44) Hardy, C. G.; Zhang, J.; Yan, Y.; Ren, L.; Tang, C. Metallopolymers with Transition Metals in the Side-Chain by Living and Controlled Polymerization Techniques. *Prog. Polym. Sci.* **2014**, *39*, 1742-1796.

(45) Feng, C.; Shen, Z.; Yang, D.; Li, Y.; Hu, J.; Lu, G.; Huang, X. Synthesis of Well-Defined Amphiphilic Graft Copolymer Bearing Poly(2-acryloyloxyethyl ferrocenecarboxylate) Side Chains via Successive SET-LRP and ATRP. *J. Polym. Sci. Part A: Polym. Chem.* **2009**, *47*, 4346-4357.

(46) Zhai, S.; Shang, J.; Yang, D.; Wang, S.; Hu, J.; Lu, G.; Huang, X. Successive SET-LRP and ATRP Synthesis of Ferrocene-Based PPEGMEA-*g*-PAEFC Well-Defined Amphiphilic Graft Copolymer. *J. Polym. Sci. Part A: Polym. Chem.* **2012**, *50*, 811-820.

(47) Maire, H. C.; Ibrahim, S.; Li, Y.; Ito, T. Effects of Substrate Roughness on the Orientation of Cylindrical Domains in Thin Films of a Polystyrene-Poly(Methylmethacrylate) Diblock Copolymer Studied Using Atomic Force Microscopy and Cyclic Voltammetry. *Polymer* **2009**, *50*, 2273-2280.

(48) Kim, B. Y.; Ratcliff, E. L.; Armstrong, N. R.; Kowalewski, T.; Pyun, J. Ferrocene Functional Polymer Brushes on Indium Tin Oxide via Surface-Initiated Atom Transfer Radical Polymerization. *Langmuir* **2010**, *26*, 2083-2092.

(49) Huang, E.; Russell, T. P.; Harrison, C.; Chaikin, P. M.; Register, R. A.; Hawker, C. J.; Mays, J. Using Surface Active Random Copolymers to Control the Domain Orientation in Diblock Copolymer Thin Films. *Macromolecules* **1998**, *31*, 7641-7650.

(50) Bridges, T. E.; Uibel, R. H.; Harris, J. M. Measuring Diffusion of Molecules into Individual Polymer Particles by Confocal Raman Microscopy. *Anal. Chem.* **2006**, *78*, 2121-2129.

(51) Oyama, N.; Anson, F. C. Factors Affecting the Electrochemical Responses of Metal-Complexes at Pyrolytic-Graphite Electrodes Coated with Films of Poly(4-Vinylpyridine). *J. Electrochem. Soc.* **1980**, *127*, 640-647.

(52) Ju, H.; Leech, D. Electrochemistry of Poly(vinylferrocene) Formed by Direct Electrochemical Reduction at a Glassy Carbon Electrode. *J. Chem. Soc. Faraday Trans.* **1997**, *93*, 1371-1375.

Chapter 4 - Electrochemical Characterization and Catalytic Application of Gold-Supported Ferrocene-Containing Diblock Copolymer Thin Films in Ethanol Solution

Reproduced with permission from American Chemical Society.

Published as: G. Ghimire, H. Coceancigh, Y. Yi, T. Ito, *ACS Appl. Mater. Interfaces* **2017**, *9*, 2906-2913.

Contribution of Authors

This is an extension of Chapter 3. TI designed and guided the overall project. YY synthesized all the block copolymers. GG collected all the ellipsometry, AFM and electrochemical data. GG analyzed the ellipsometry and AFM data, and GG and TI analyzed the electrochemical data. HC collected ^{1}H-NMR data for the samples collected by GG, and HC and TI analyzed the NMR data.

4.1 Introduction

Block copolymers with a ferrocene-containing segment have recently received remarkable attention, because they can form self-organized, redox-active microdomains in their monolithic films,[1-6] as with other block copolymers.[7-9] Block copolymers with ferrocene moieties incorporated into the polymer backbone have shown to form microdomains with sizes and morphologies predictable from the block molecular weights and compatibility.[1-3] Block copolymers with ferrocene moieties in the side chain have also exhibited microphase separation in spite of their high glass transition temperatures.[4-6,10-12] The ferrocene-containing nanostructures provide charge transport pathways based on collisional electron self-exchange

reactions (electron hopping) between adjacent ferrocene moieties.[13-17] These microdomains are surrounded by redox-inactive scaffolds, and thus possess higher stability in electrochemical applications as compared with ferrocene-based homopolymer films.[14,17] Based on these properties, electrode-supported monolithic films of ferrocene-containing block copolymers have been explored for electrochemical mediation in electrochemical enzyme sensors[14,15] and electrochemically-controlled biomolecule capture.[16]

For these applications, ferrocene-containing microdomains need to have high charge transport efficiency. The charge transport efficiency of redox moieties in a redox polymer film has been quantitatively assessed from an apparent diffusion coefficient (D_{ap}) that is often measured using chronocoulometry (CC).[18] D_{ap} is controlled by the concentration, electron transfer and dynamic properties of the redox moieties,[19] as revealed through a number of electrochemical studies of various electrode-supported redox homopolymers.[20-23] Due to the mobility of the redox moieties restricted by covalent linking to the polymer frameworks, D_{ap} in a redox homopolymer film is usually by several orders smaller than the physical diffusion coefficient of the molecular counterpart in solution.[24,25] In addition, ion migration associated with charge compensation in the films is known to give significant influences on the charge transport properties of ferrocene-containing homopolymer films.[26,27] Importantly, these electrochemical measurements are carried out in solution, and thus these redox polymers should be, to some extent, swollen by solvent. It was shown that the swelling of films of redox homopolymers such as poly(vinylferrocene) (PVFc) regulates D_{ap} through an increase in the mobility of redox moieties, the facilitation of ion migration, and a decrease in redox moiety concentration.[28,29] The redox processes of ferrocene moieties further manipulate the swellability

of a redox homopolymer film as a result of changes in solvent compatibility,[30,31] as postulated from the modulated shapes of their voltammograms.[26-29]

Previously, the influences of solvent-induced swelling on the electrochemical behavior of ferrocene-containing block copolymer films were investigated for poly(ferrocenyldimethylsilane)-*block*-poly(dimethylsiloxane) (PFDMS-*b*-PDMS)[13] and polystyrene-*block*-poly(2-(acryloyloxy)ethyl ferrocenecarboxylate) (PS-*b*-PAEFc; **Figure 1.3b**).[17] In the former,[13] the crucial roles of polymer swelling in the redox properties of the PFDMS microdomains were suggested through a series of cyclic voltammetry (CV) measurements in different solvents. In the latter (**Chapter 3**),[17] the effects of PAEFc microdomain morphologies on their redox properties were investigated using CV and CC in an acetonitrile (MeCN) solution. Atomic force microscopy (AFM) images suggested the formation of lamellar, cylindrical and spherical PAEFc microdomains in thin films of PS-*b*-PAEFc with PAEFc volume fractions (f_{PAEFc}) of 0.47, 0.30 and 0.17, respectively. Similar D_{ap} was obtained in MeCN-swollen PS-*b*-PAEFc films with lamellar and cylindrical microdomains, suggesting the comparable concentration and dynamic properties of the ferrocene moieties in the PAEFc microdomains. More interestingly, PAEFc microdomains buried within the PS matrix were redox-active as long as they were electrically communicable with the underlying electrode. This observation indicates that the ionic species (PF_6^-) could migrate from the MeCN solution through the MeCN-swellable PS matrix.[32] Unfortunately, a difference in the solvent compatibilities of the two microdomains was not recognized, probably because both PS and PAEFc microdomains were significantly swollen by MeCN.

In this chapter, electrochemical properties of electrode-supported PS-*b*-PAEFc films of different f_{PAEFc} were investigated in an ethanol (EtOH) solution. EtOH is known not to swell

PS,[33] and thus should reduce the permeability of the PS matrix as compared with MeCN. A series of CV and CC measurements were carried out in MeCN and EtOH for each of the PS-*b*-PAEFc films for direct comparison. Furthermore, PS-*b*-PAEFc films were examined as electrochemically-responsive catalysts[34] for Michael addition reactions in an EtOH solution, as demonstrated with PVFc homopolymer layers deposited onto carbon fiber electrodes.[35] Ferrocene-containing block copolymer monoliths based on PVFc-*block*-polyisoprene were explored as heterogeneous catalysts for the Michael addition reaction, but the catalytic ferrocenium moieties were obtained via the oxidation of ferrocene by Ag^+, not by a potential application.[10] These measurements will provide insight into the influences of the ferrocene-containing nanostructures and film permeability on the electrochemical properties and catalytic applications.

4.2 Experimental Procedures

4.2.1 Chemicals and Materials

PS-*b*-PAEFc was synthesized by atom transfer radical polymerization as reported previously.[17] AEFc monomer was synthesized as reported previously.[36] Ferrocene (98%, Aldrich), tetrabutylammonium hexafluorophosphate ($TBAPF_6$; ≥99%, Aldrich), sodium hexafluorophosphate ($NaPF_6$; >98.5%, Acros), acetonitrile (anhydrous, Alfa Aesar), ethanol (>99%, Decon laboratories), ethyl 2-oxocyclopentanecarboxylate (E2OC; Acros), methyl vinyl ketone (MVK; Acros), *trans*-4-phenyl-3-buten-2-one (*trans*-PBO; Acros), deuterated chloroform ($CDCl_3$; Cambridge Isotope laboratories) and toluene (HPLC grade, Acros) were used without further purification. Gold-coated silicon wafers, which were prepared by sputtering 10 nm of Ti followed by 200 nm of Au onto Si (100) wafers, were purchased from LGA Thin Films (Foster City, CA).

4.2.2 Preparation and Characterization of PS-*b*-PAEFc Films

PS-*b*-PAEFc films were prepared via spin-coating from a dilute toluene solution (0.5-2.5%) on cleaned gold substrates according to procedures reported previously.[17] The ellipsometric thicknesses of PS-*b*-PAEFc films were measured in a dry condition using a J.A. Woollam alpha-SE spectroscopic ellipsometer. AFM images of PS-*b*-PAEFc films were obtained by tapping/phase mode in air, using a Digital Instruments Multimode AFM with Nanoscope IIIa electronics. Tapping mode AFM probes (cantilever length, 225 μm; force constant, 50 N/m; resonant frequency, 170 kHz) were purchased from Aspire.

4.2.3 Electrochemical Measurements

CV and CC measurements were performed in a CH Instruments 720C electrochemical analyzer. Electrochemical measurements were carried out under an argon or nitrogen atmosphere in a three-electrode cell (**Figure 4.1**)[17] with a Pt counter electrode and a Ag/Ag^+ reference electrode (CH Instruments). Non-aqueous Ag/Ag^+ reference electrodes were fabricated from silver wires that were dipped into a 10 mM silver nitrate solution in 0.1 M $TBAPF_6$/MeCN or 0.1 M $NaPF_6$/EtOH. The electrodes were then kept airtight and stored in 0.1 M $TBAPF_6$/MeCN or 0.1 M $NaPF_6$/EtOH, respectively. The potential of the reference electrode was obtained from cyclic voltammograms of ferrocene (*ca*. 3 mM, in 0.1 M $TBAPF_6$/MeCN or 0.1 M $NaPF_6$/EtOH). A PS-*b*-PAEFc-coated gold substrate was immobilized at the bottom of a Teflon-based cell with an O-ring (3.3 mm in radius) to serve as the working electrode (**Figure 4.1**).[37,38] Cyclic voltammograms at different potential scan rates (v = 0.01, 0.02, 0.05, 0.08, 0.1, 0.2, 0.5, 0.8 and 1 V/s) and CC data were recorded in 0.1 M $TBAPF_6$/MeCN, and then in 0.1 M $NaPF_6$/EtOH. CC was performed by applying potential steps (60 sec each) from 0 to +0.6 V and then from +0.6 to 0 V (vs Ag/Ag^+) in MeCN or from -0.2 to +0.35 V and then from +0.35 to -0.2

V (vs Ag/Ag^+) in EtOH. The low and high potentials were sufficiently negative and positive with respect to the cathodic and anodic peak potentials in cyclic voltammograms, respectively. The maximum charge ($Q_{a,max}$) and D_{ap} for the oxidation of PAEFc microdomains were determined from the CC data and the ellipsometric thickness of the dry film, as described in **Chapter 3**.[17]

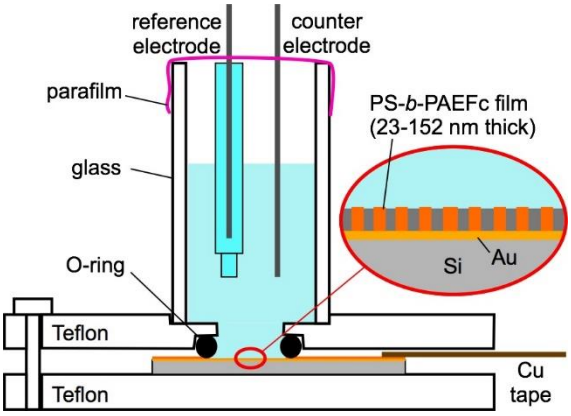

Figure 4.1 Schematic illustration of an electrochemical cell employed in this study. For the catalysis experiments, the upper opening of the glass tube was sealed by parafilm. 2017, Copyright: American Chemical Society.

4.2.4 Michael Addition Reaction

After the completion of the CV and CC measurements in the MeCN and EtOH solutions, PS-*b*-PAEFc films (38-80 nm in thickness) embedded on the electrochemical cells were explored as electrochemically-responsive heterogeneous catalysts for Michael addition reaction. A solution (1 mL) containing 1 M MVK (or 1 M *trans*-PBO) and 0.3 M E2OC in 0.1 M $NaPF_6$/EtOH, which was prepared in a glass vial that was cleaned with concentrated nitric acid to remove any metallic contaminants, was placed into the cell under an argon or nitrogen atmosphere. The cell was completely sealed by parafilm to prevent the evaporation of the reaction mixture. A continuous potential of +0.3 ~ 0.4 V (vs. Ag/Ag^+), which was positive

enough to oxidize the ferrocene moieties in 0.1 M $NaPF_6$/EtOH, was applied to the working electrode without stirring the solution at room temperature (*ca*. 20 °C). An aliquot of 30 µL was taken from the reaction mixture and diluted with 500 µL $CDCl_3$ every 24 hours for 3 days. The ^{1}H-NMR spectra of the solutions were measured on a Varian Mercury 400 MHz Fourier transform NMR spectrometer, and chemical shifts were reported in δ values in ppm downfield of tetramethylsilane. The reaction progress was monitored from the integration of the **5** and **5d** signals of the product and E2OC around 4.1 ppm, respectively (**Scheme 4.1**). The vinyl proton signals of MVK (**2a**, **3a** and **3a'**) around 6.3 ppm could not be used to measure the reaction yield in this study because of the gradual loss of volatile MVK (boiling point: 81.4 °C) during the reaction and sampling. In addition, the signal from the **4d** proton of E2OC was not used because its integration was fairly small (0.6H instead of 1H with respect to 2H from **5d**) in the reaction mixture prior to the potential application (*i.e*., Day 0), possibly reflecting its high acidity. The integrations of these signals, in general, decreased as the reaction proceeded, but were not ideal for the calculation of reaction yield.

Scheme 4.1. Reactions Investigated in This Study. 2017, Copyright: American Chemical Society.

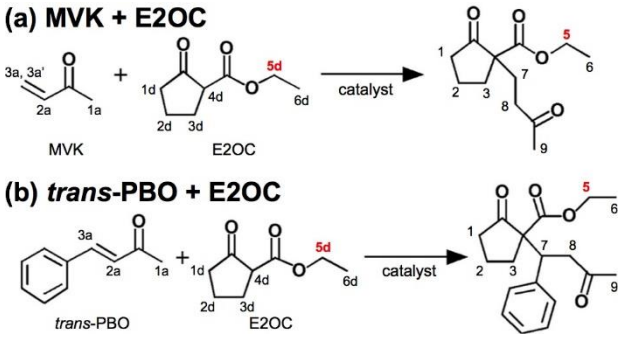

4.3 Results and Discussion

4.3.1 Comparison of Electrochemical Properties of PS-*b*-PAEFc films in the MeCN and EtOH Solutions.

First, the electrochemical behavior of a pristine electrode-supported PS-*b*-PAEFc film (f_{PAEFc} = 0.30) was measured in 0.1 M $NaPF_6$/EtOH. The PS-*b*-PAEFc film did not exhibit faradaic currents (**Figure 4.2a**, blue) except for those (**Figure 4.2b**) attributable to defects in the film (**Figure 4.3a**, white arrow). This result indicates that both PS and PAEFc microdomains were not swollen by EtOH, which prevented the collisional motions of the ferrocene moieties and counter ion migration. In contrast, significantly larger faradaic currents were observed in the EtOH solution at the same PS-*b*-PAEFc film after a series of CV measurements in 0.1 M $TBAPF_6$/MeCN (**Figure 4.2a** (red)). This result shows that a PS-*b*-PAEFc film can be "activated" by applying a potential to induce the redox reaction of the ferrocene moieties in the MeCN solution. The potential application led to the incorporation of the supporting electrolyte into the films, which modulated the permeability of the films. The electrolyte incorporation facilitated the migration of PF_6^- from the EtOH solution into the film, resulting in the enhancement of the redox processes of the ferrocene moieties.

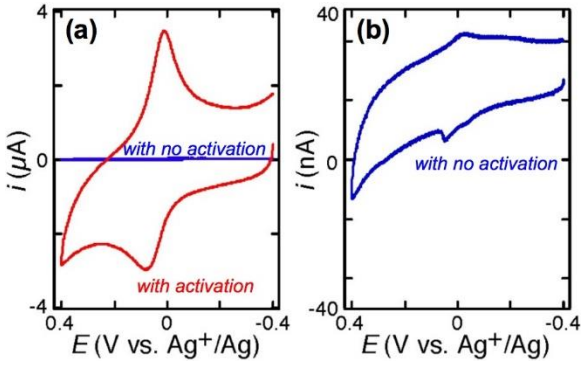

Figure 4.2 (a) Cyclic voltammograms (v = 0.1 V/s) measured at a thin film of PS_{154}-*b*-$PAEFc_{26}$ (f_{PAEFc} = 0.30; 67 nm thick) in 0.1 M $NaPF_6$/EtOH before (blue) and after activation based on CV measurements in 0.1 M $TBAPF_6$/MeCN (red). Note that no CC measurement in 0.1 M $TBAPF_6$/MeCN was conducted prior to the measurement of the latter, which possibly resulted in

the observation of a voltammogram of surface-confined species with smaller faradaic currents than those discussed below. **(b)** The expanded voltammogram for the former. E (V vs. Ag^+/Ag) = +0.106 ± 0.030 V vs. Fc^+/Fc in EtOH (N = 14). 2017, Copyright: American Chemical Society.

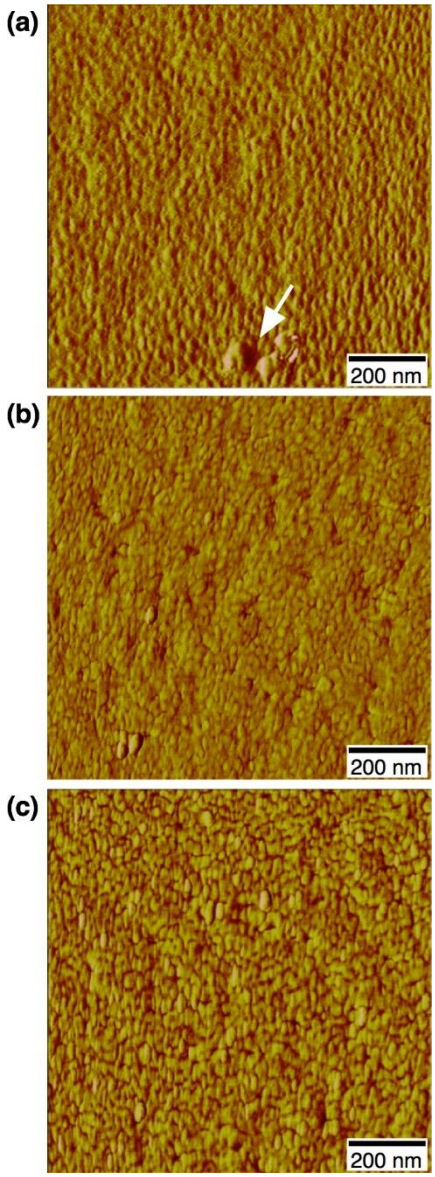

Figure 4.3 AFM phase images (1 x 1 μm^2) of thin films of PS_{154}-*b*-$PAEFc_{26}$ (f_{PAEFc} = 0.30; 29 nm in ellipsometric thickness). **(a)** Pristine, **(b)** after electrochemical experiments in 0.1 M $TBAPF_6$/MeCN, and **(c)** after electrochemical experiments in 0.1 M $NaPF_6$/EtOH. 2017, Copyright: American Chemical Society.

Importantly, the microdomain structures were retained upon electrochemical measurements in these two organic solutions. **Figure 4.3** shows AFM phase images of PS_{154}-*b*-$PAEFc_{26}$ (f_{PAEFc}

= 0.30) films before and after CV and CC measurements in 0.1 M $TBAPF_6$/MeCN, and after the subsequent CV/CC measurements in 0.1 M $NaPF_6$/EtOH. The AFM image of the pristine film (**Figure 4.3a**) showed circular structures with average diameters of *ca*. 22 nm that could be assigned to vertically-oriented cylindrical microdomains exposed to the film surface.[17] Similar structures were observed after the electrochemical measurements in 0.1 M $TBAPF_6$/MeCN (**Figure 4.3b**) and in 0.1 M $NaPF_6$/EtOH (**Figure 4.3c**). AFM phase images of PS_{154}-*b*-$PAEFc_{12}$ (f_{PAEFc} = 0.17) films before and after the electrochemical measurements are shown in **Figure 4.4**, which do not reveal clear microdomain morphology as previously reported for a pristine film.[17] Slight differences in morphology between the images possibly resulted from the solvent swelling-deswelling processes of the films, because similar changes in film morphology were observed after immersing a PS_{154}-*b*-$PAEFc_{26}$ film in the MeCN and EtOH solutions (**Figure 4.5**).

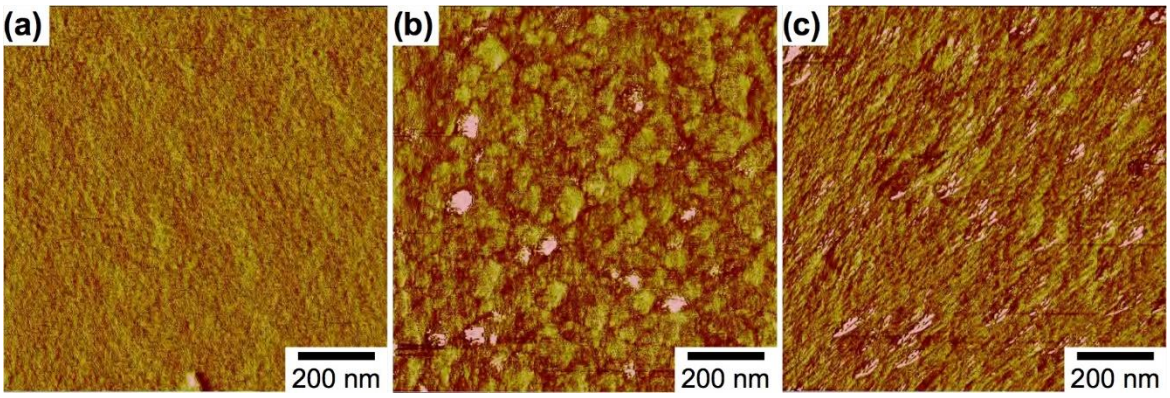

Figure 4.4 AFM phase images (1 x 1 μm^2) of a thin film of PS_{154}-*b*-$PAEFc_{12}$ (f_{PAEFc} = 0.17; 38 nm in ellipsometric thickness). **(a)** Pristine, **(b)** after electrochemical experiments in 0.1 M $TBAPF_6$/acetonitrile, and **(c)** after electrochemical experiments in 0.1 M $NaPF_6$/ethanol. 2017, Copyright: American Chemical Society.

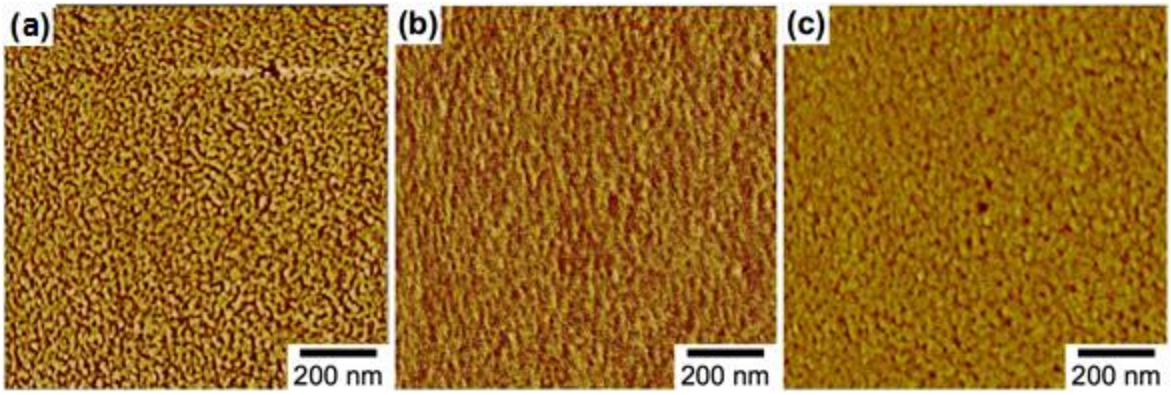

Figure 4.5 AFM phase images (1 x 1 μm^2) of a thin film of PS$_{154}$-*b*-PAEFc$_{26}$ (f_{PAEFc} = 0.30; 38 nm in ellipsometric thickness). **(a)** Pristine, **(b)** after immersion in 0.1 M TBAPF$_6$/MeCN, and **(c)** after subsequent immersion in 0.1 M NaPF$_6$/EtOH with no potential application. 2017, Copyright: American Chemical Society.

Figure 4.6 shows typical cyclic voltammograms measured at PS-*b*-PAEFc films (50-70 nm in thickness) of the three different f_{PAEFc} in (a) 0.1 M TBAPF$_6$/MeCN and (b) 0.1 M NaPF$_6$/EtOH. The faradaic currents were larger for PS-*b*-PAEFc with the larger f_{PAEFc}, as reported previously.[17] These films afforded similar E^0 in each of the solutions regardless of f_{PAEFc} and film thickness (**Figure 4.7a**, **Table 4.1**). In the MeCN solution, the voltammograms were controlled by surface-confined species, which was supported by the relatively narrow peak widths (**Figure 4.6a**)[39] and the slope of log i_p–log v plots close to 1 at the scan rate range of v = 0.01 ~ 0.2 V/s (**Figure 4.8**).[17] In the EtOH solution, the voltammograms appeared to be more diffusion-controlled, as suggested by the wider peak widths (**Figure 4.6b**). The slopes of log i_p–log v plots (**Figure 4.8**) were close to 0.5 for PS-*b*-PAEFc (f_{PAEFc} = 0.47 and 0.30), whereas the slope close to 1 was measured for PS-*b*-PAEFc (f_{PAEFc} = 0.17). The observation of diffusion-controlled voltammograms can be attributed to the reduction of redox moiety mobility and/or counter ion migration in the less-swollen film. It should be noted that voltammograms in the EtOH solution were strongly affected by the activation conditions in 0.1 M TBAPF$_6$/MeCN. A smaller number of CV/CC measurements in the MeCN solution resulted in the observation of

surface-confined voltammograms with smaller faradaic currents, as shown in **Figure 4.6a**. The larger number of CV/CC measurements in the MeCN solution often led to the observation of voltammograms with multiple faradaic peaks as reported by Chen *et al.*,[13] possibly reflecting the heterogeneous swelling of the film.[24]

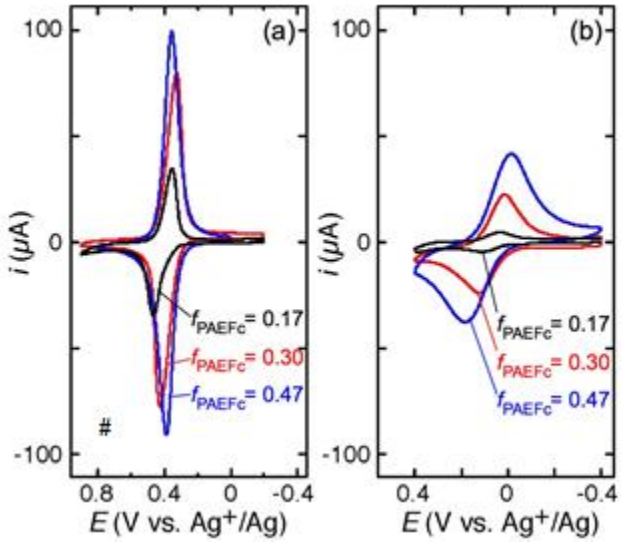

Figure 4.6 Cyclic voltammograms (v = 0.1 V/s) measured in **(a)** 0.1 M $TBAPF_6$/MeCN and **(b)** 0.1 M $NaPF_6$/EtOH for thin films of PS_{154}-*b*-$PAEFc_{51}$ (f_{PAEFc} = 0.47; 56 nm thick; blue), PS_{154}-*b*-$PAEFc_{26}$ (f_{PAEFc} = 0.30; 67 nm thick; red), and PS_{154}-*b*-$PAEFc_{12}$ (f_{PAEFc} = 0.17; 67 nm; black). Note that the potential was plotted with respect to a Ag^+/Ag reference electrode: *E* (V vs. Ag^+/Ag) = -0.087 ± 0.009 V vs. Fc^+/Fc (*N* = 14) in $TBAPF_6$/MeCN and *E* (V vs. Ag^+/Ag) = +0.106 ± 0.030 V vs. Fc^+/Fc (*N* = 14) in $NaPF_6$/EtOH. # Data taken from Chapter 3. 2017, Copyright: American Chemical Society.

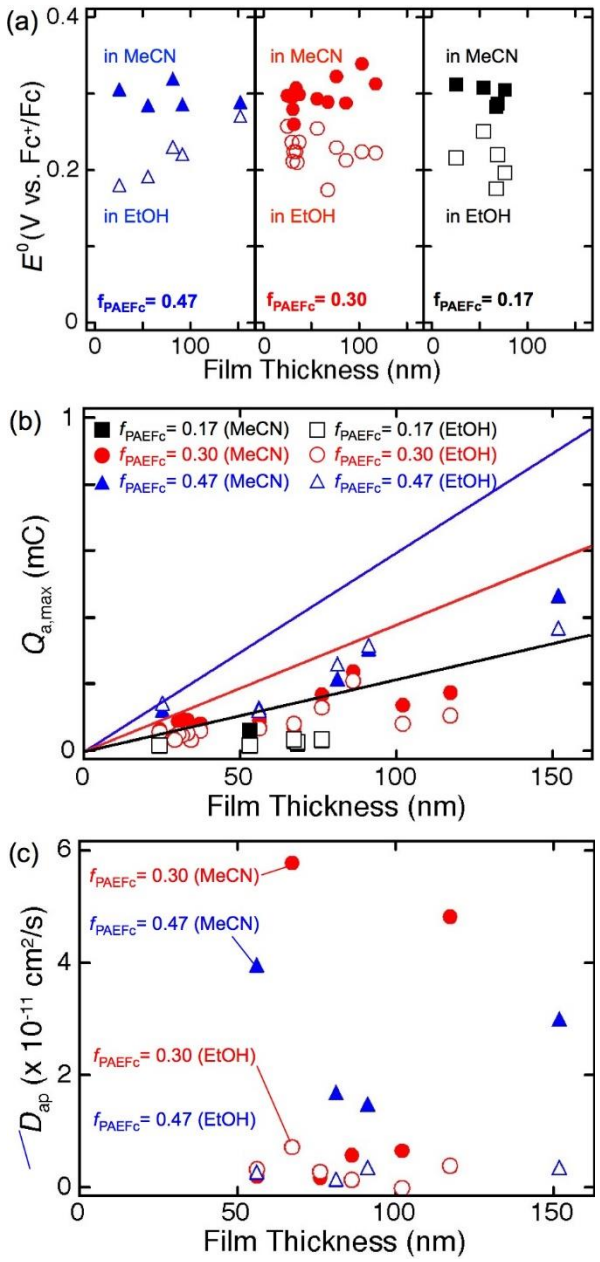

Figure 4.7 Effects of film thickness on **(a)** E^0 (V vs. Fc^+/Fc), **(b)** $Q_{a,max}$ (mC) and **(c)** D_{ap} (cm^2/s) measured in 0.1 M $TBAPF_6/CH_3CN$ (filled symbols) and 0.1 M $NaPF_6$/EtOH (open symbols) for PS_{154}-*b*-$PAEFc_{51}$ (f_{PAEFc} = 0.47; blue triangles), PS_{154}-*b*-$PAEFc_{26}$ (f_{PAEFc} = 0.30; red circles), and PS_{154}-*b*-$PAEFc_{12}$ (f_{PAEFc} = 0.17; black squares). The E_0 values were determined from CVs at 0.1 V/s (the second or third sweep), and the $Q_{a,max}$ and D_{ap} values were measured from CC data. The solid lines in **(b)** indicate anodic charges that should be obtained when all the ferrocene moieties in the films were oxidized (Q_{theo}). 2017, Copyright: American Chemical Society.

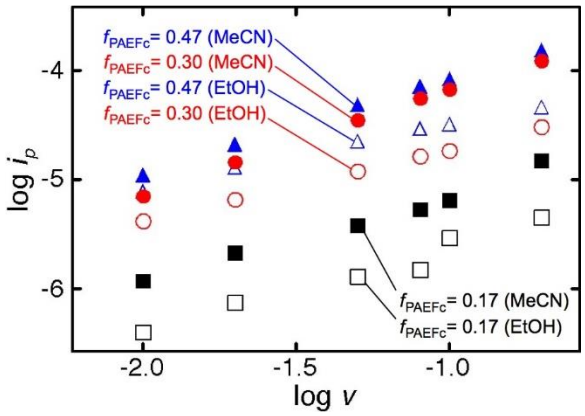

Figure 4.8 Plots of logi_p vs log$v$ (i_p: anodic peak current; v = 0.01 ~ 0.2 V/s, where voltammograms of surface-confined species were observed in 0.1 M $TBAPF_6$/MeCN) obtained from the voltammograms shown in **Figure 4.6**. The slopes were 0.88 (in MeCN; filled blue triangles) and 0.58 (in EtOH; open blue triangles) for PS_{154}-*b*-$PAEFc_{51}$ (f_{PAEFc} = 0.47), 0.96 (in MeCN; filled red circles) and 0.66 (in EtOH; open red circles) for PS_{154}-*b*-$PAEFc_{26}$ (f_{PAEFc} = 0.30), and 0.79 (in MeCN; filled black squares) and 0.78 (in EtOH; open black squares) for PS_{154}-*b*-$PAEFc_{12}$ (f_{PAEFc} = 0.17). 2017, Copyright: American Chemical Society.

Table 4.1 E^0 and D_{ap} Obtained for Gold-Supported PS-*b*-PAEFc Films in 0.1 M $TBAPF_6$/MeCN and 0.1 M $NaPF_6$/EtOH. 2017, Copyright: American Chemical Society.

Polymer	f_{PAEFc}[a]	Solvent	E^0 (V vs. Fc^+/Fc)[b]	D_{ap} ($\mu m^2/s$)[c]
PS_{154}-*b*-$PAEFc_{51}$	0.47	MeCN	0.297 ± 0.015 (5)	$(2.5_3 \pm 1.1_7) \times 10^{-3}$ (4)
		EtOH	0.219 ± 0.036 (5)	$(2.7_8 \pm 0.9_6) \times 10^{-4}$ (4)
PS_{154}-*b*-$PAEFc_{26}$	0.30	MeCN	0.300 ± 0.019 (13)	$(2.0_5 \pm 2.5_6) \times 10^{-3}$ (6)
		EtOH	0.225 ± 0.021 (13)	$(3.1_8 \pm 2.4_4) \times 10^{-4}$ (6)
PS_{154}-*b*-$PAEFc_{12}$	0.17	MeCN	0.299 ± 0.013 (5)	–[d]
		EtOH	0.213 ± 0.028 (5)	–[d]

[a] Calculated from ρ_{PS} = 1.05 (g/cm^3) and ρ_{PAEFc} = 1.25 (g/cm^3).[40] The latter was estimated from the density of polyvinylferrocene. [b] Average ± standard deviation of E^0 (V vs. Fc^+/Fc) measured for the second or third sweep (v = 0.1 V/s) at PS-*b*-PAEFc films (23-152 nm in ellipsometric thickness) using a Ag^+/Ag reference electrode. The number of measurements (N) is shown in parenthesis. The potentials of the reference electrodes (E (V vs. Ag^+/Ag)) were (–0.087 ± 0.009) and (+0.106 ± 0.030) V vs. Fc^+/Fc (N = 14) in MeCN and EtOH, respectively. [c] Average ± standard deviation of D_{ap} obtained from CC data for PS-*b*-PAEFc films with ellipsometric thicknesses of ≥ 50 nm at t = 0.1 ~ 0.15 sec. The number of samples examined is shown in parenthesis. [d] Not calculated because diffusion-controlled CVs were not obtained.

The fraction of active ferrocene moieties in the films and D_{ap} within the PAEFc microdomains were quantified using CC according to procedures reported previously.[17] PS_{154}-*b*-$PAEFc_{51}$ (f_{PAEFc} = 0.47) afforded the larger $Q_{a,max}$ for the thicker films in both the solutions, whereas PS_{154}-*b*-$PAEFc_{12}$ (f_{PAEFc} = 0.17) offered $Q_{a,max}$ almost independent of film thickness (**Figure 4.7b**). PS_{154}-*b*-$PAEFc_{26}$ (f_{PAEFc} = 0.30) exhibited the intermediate thickness dependence of $Q_{a,max}$. These observations could be explained by a difference in microdomain morphology: The two PS-*b*-PAEFc with the larger f_{PAEFc} afforded possibly lamellar or cylindrical PAEFc microdomains that could be extended from the underlying substrates to the film surface, in contrast to the spherical microdomains formed from the PS-*b*-PAEFc (f_{PAEFc} = 0.17).[17] In addition, the $Q_{a,max}$ was significantly smaller than Q_{theo}, suggesting that the faradaic currents were measured from ferrocene moieties that could electrically communicate with the underlying substrate.[17] Interestingly, $Q_{a,max}$ in the EtOH solution was fairly close to that in the MeCN solution, indicating that the redox activity of the ferrocene moieties retained in the less-swollen films.

D_{ap} was determined in both the solutions for PS-*b*-PAEFc films (f_{PAEFc} = 0.47 and 0.30) thicker than 50 nm. These films gave diffusion-controlled voltammograms that were based on electron hopping at the faster v ($\geq$ 0.2 V/s) in the MeCN solution[17] and also at the entire v examined in the EtOH solution (**Figure 4.8**). D_{ap} values ($\approx 10^{-3}$~10^{-4} $\mu m^2/s$) were significantly smaller than the physical diffusion coefficient of ferrocene in solution (*ca*. 10^3 $\mu m^2/s$) due to the restricted motions of the ferrocene moieties and limited counter ion migration, as with PVFc films.[24,25] D_{ap} did not depend on film thickness for both the solutions (**Figure 4.7c**), and instead was largely different among the films. In comparison of D_{ap} values in the two solutions for each of the films, D_{ap} in the EtOH solution was significantly smaller than that in the MeCN solution.

On average, the former was by one order of magnitude smaller than the latter (**Table 4.1**). The smaller D_{ap} values in the EtOH solution reflected the poorer swelling of the films in the EtOH solution that led to the limited electron hopping and/or counter ion migration. Negligible difference in D_{ap} between the two PS-*b*-PAEFc suggests that the PAEFc microdomains were swollen to the similar extents.

4.3.2 Electrode-Supported PS-*b*-PAEFc Films as Electrochemically-Responsive Catalysts for Michael Addition Reaction

Immediately after the series of CV and CC measurements, some of these PS-*b*-PAEFc films were explored for the catalysis of the Michael addition reaction of a 1,3-dicarbonyl compound with an activated alkene on the basis of the Fe(III) produced by the PAEFc oxidation. Fe(III) has been shown to be a good catalyst for the Michael addition reaction,[41] and ferrocenium ions generated from ferrocene-containing polymers via chemical[10] and electrochemical[35] oxidation were previously explored for the catalysis of the reaction. In this study, the effects of microdomain morphology on the reaction were first investigated for PS-*b*-PAEFc that were anticipated to give cylindrical (f_{PAEFc} = 0.30) and spherical (f_{PAEFc} = 0.17) microdomains. E2OC and MVK were employed as a 1,3-dicarbonyl compound with an activated alkene, respectively (**Figure 1.3b**). Subsequently, the reaction was explored for a different activated alkene, *trans*-PBO.

Figure 4.9 shows ^{1}H-NMR spectra of the reaction mixtures taken after different durations of potential application for the electrochemical oxidation of the ferrocene moieties in electrode-supported PS-*b*-PAEFc films. The ^{1}H-NMR measurements were carried out by diluting an aliquot of the reaction mixture containing 0.1 M $NaPF_6$/EtOH by $CDCl_3$. Prior to the potential application (Day 0 in **Figure 4.9ab**), the vinyl proton signals of MVK (**2a**, **3a** and **3a'** in **Scheme**

4.1a) around 6.3 ppm and the quartet from **5d** of E2OC (**Scheme 4.1a**) around 4.15 ppm were clearly observed. Upon applying the potential (Day 1-3), the vinyl proton signals decreased and another quartet around 4.11 ppm, which could be assigned to **5** of the product (2-(3-oxobutyl)cyclopentanone-2-carboxylic acid ethyl ester),[41] appeared for both the PS-*b*-PAEFc films. It should be pointed out that the two upfield peaks of the quartet from **5d** and the two downfield peaks of the quartet from **5** overlapped. In contrast, no reaction proceeded at PS-*b*-PAEFc films without the potential application after 3 days (**Figure 4.10**), indicating the involvement of the oxidized PAEFc microdomains in the reaction. These changes were more remarkable for longer reaction time, as supported by the reaction progress that was monitored from the **5d** and **5** proton signals of E2OC and the product (**Figure 4.11**), respectively. Interestingly, the reaction was noticed for both the two types of PS-*b*-PAEFc. In particular, the reaction with PS-*b*-PAEFc (f_{PAEFc} = 0.17) was unexpected, considering that its spherical PAEFc microdomains should be buried within the PS matrix.[17] The similar reaction yields suggests that the reaction took place between MVK and E2OC that penetrated through the partially-swollen PS matrix and reacted at the PAEFc microdomains directly contact to the underlying electrode. The catalytic reaction could be regulated by controlling applied potentials (**Figure 4.12**), as with a PVFc-coated electrode.[35] An increase in the product was observed while an oxidative potential (E = +0.31 V) was applied (Day 1 and Day 3), but not while a reductive potential (E = -0.20 V) was applied (Day 2). The relatively slow reaction was attributable to the absence of solution stirring, the small effective surface area of the film, and also the requirement of the reactant permeation through the film. The maximum reaction may partly be limited by the gradual evaporation of MVK during the reaction, as suggested by the very small vinyl proton signals at Day 3.

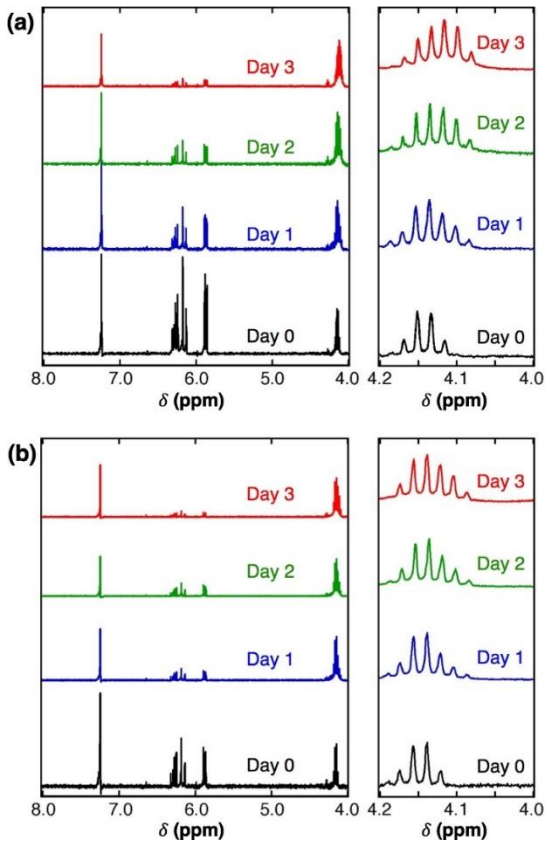

Figure 4.9 ^{1}H-NMR spectra (4.0–8.0 ppm) of the reaction mixtures of MVK and E2OC sampled after different periods of reaction time with potential application (+0.37 V vs Ag/Ag^{+}) for thin films of **(a)** PS_{154}-*b*-$PAEFc_{26}$ (f_{PAEFc} = 0.30; 64 nm thick) and **(b)** PS_{154}-*b*-$PAEFc_{12}$ (f_{PAEFc} = 0.17; 65 nm thick). The reaction solutions initially consisted of **(a)** 1.1 M MVK and 0.36 M E2OC in 0.1 M $NaPF_6$/EtOH and **(b)** 1.0 M MVK and 0.35 M E2OC in 0.1 M $NaPF_6$/EtOH. The magnified spectra at 4.0–4.2 ppm were also shown (right). The NMR spectra were collected by Herman Coceancigh. 2017, Copyright: American Chemical Society.

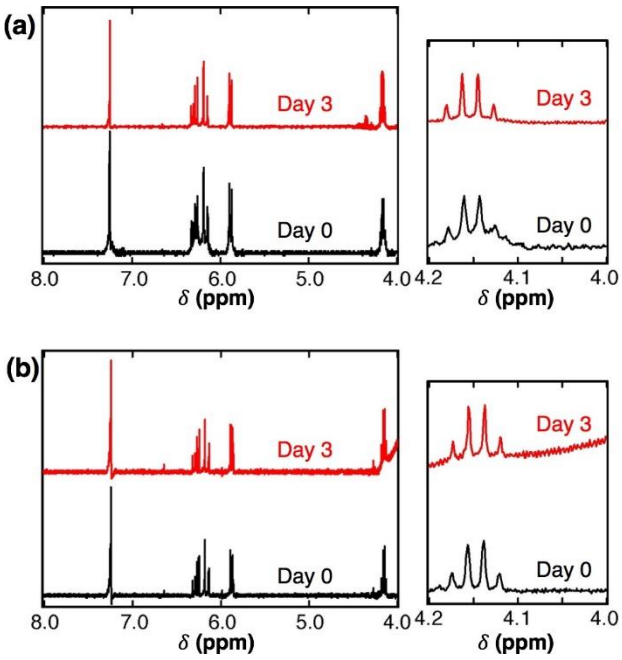

Figure 4.10. ^{1}H-NMR spectra (4.0–8.0 ppm) of the reaction mixtures of MVK and E2OC upon no potential application to electrodes coated with activated thin films of **(a)** PS_{154}-*b*-$PAEFc_{26}$ (fPAEFc = 0.30; 64 nm thick) and **(b)** PS_{154}-*b*-$PAEFc_{12}$ (f_{PAEFc} = 0.17; 65 nm thick) at Day 0 and Day 3. The solutions consisted of **(a)** 1.1 M MVK and 0.36 M E2OC in 0.1 M $NaPF_6$/EtOH and **(b)** 1.0 M MVK and 0.35 M E2OC in 0.1 M $NaPF_6$/EtOH. The magnified spectra at 4.0–4.2 ppm were also shown (right). The NMR spectra were collected by Herman Coceancigh. 2017, Copyright: American Chemical Society.

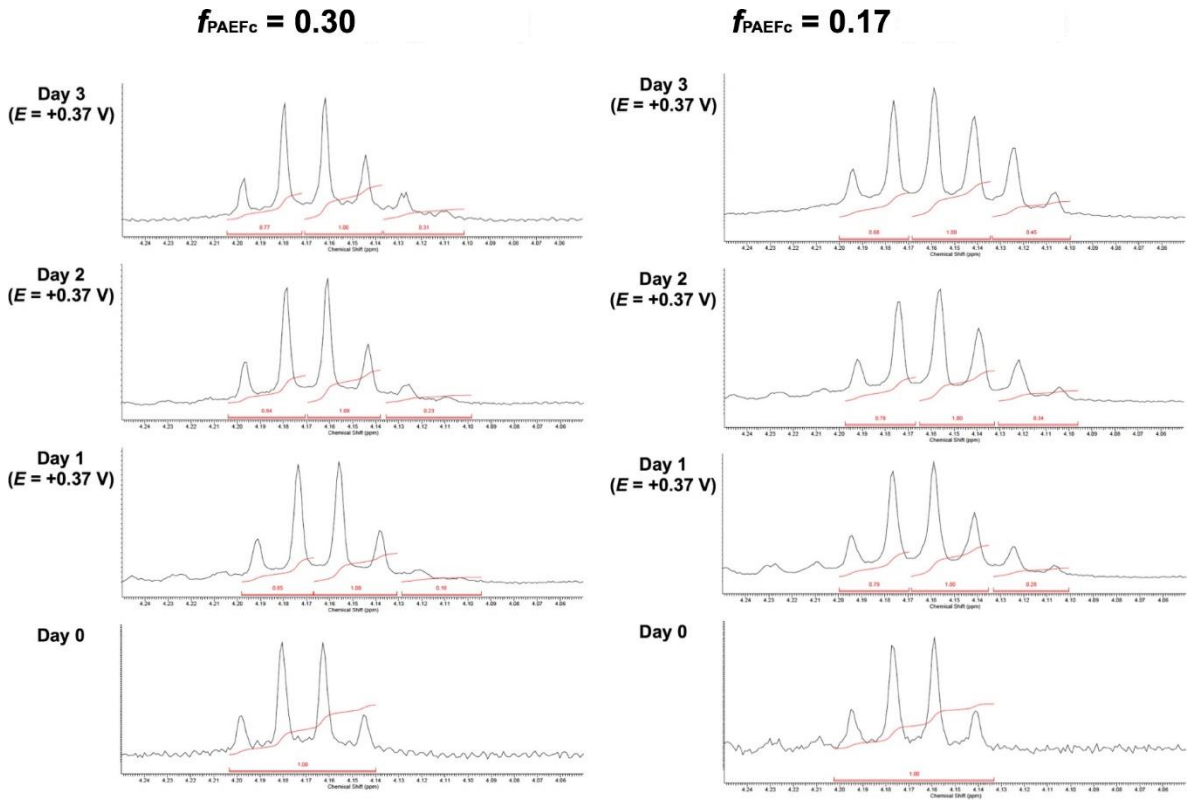

Figure 4.11 ^{1}H-NMR spectra (4.05–4.25 ppm) shown in **Figure 4.9** with the integrations of the peak areas for **5d** and **5** protons. The NMR spectra were collected by Herman Coceancigh. 2017, Copyright: American Chemical Society.

Interestingly, the reaction did not proceed between E2OC and *trans*-PBO (**Scheme 4.1b**) at electrode-supported PS-*b*-PAEFc films (**Figure 4.13**) in contrast to electrochemically-oxidized PVFc films.[35] This result could be explained by the low permeability of *trans*-PBO through the partially-swollen PS matrix. MVK, which is present as a liquid reagent at room temperature in contrast to *trans*-PBO, at the relatively high concentration (≈ 1 M) may contribute to the swelling of the PS-*b*-PAEFc film to further enhance their penetration into the film and also the release of the reaction product from the film. These results suggest a possibility to design electrochemically-responsive heterogeneous catalysts based on ferrocene-containing block copolymers with a selectivity controlled by the microdomain permeability.

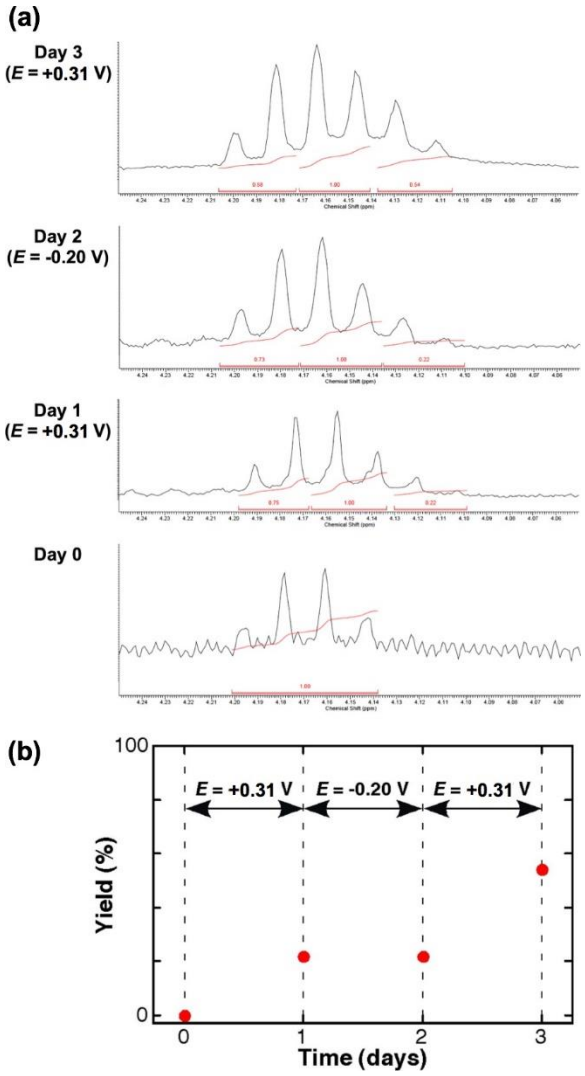

Figure 4.12 (a) ^{1}H-NMR spectra of the reaction mixtures of MVK and E2OC before and after potential application of +0.31 V (Day 1), -0.20 V (Day 2) and +0.31 V (Day 3) to a gold electrode coated with an activated thin film of PS_{154}-*b*-$PAEFc_{26}$ (f_{PAEFc} = 0.30; 38 nm thick). **(b)** The reaction yield as a function of reaction time obtained from the ^{1}H-NMR spectra shown in **(a)**. The NMR spectra were collected by Herman Coceancigh. 2017, Copyright: American Chemical Society.

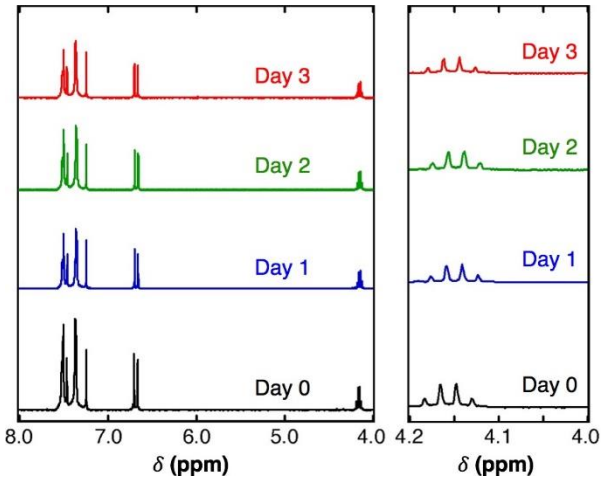

Figure 4.13 ^{1}H-NMR spectra (4.0–8.0 ppm) of the reaction mixtures of *trans*-PBO and E2OC sampled after different periods of reaction time with potential application (+0.37 V vs Ag/Ag^{+}) for thin films of PS_{154}-*b*-$PAEFc_{26}$ (f_{PAEFc} = 0.30; 64 nm thick). The reaction solutions initially consisted of 1.0 M *trans*-PBO and 0.33 M E2OC in 0.1 M $NaPF_6$/EtOH. The magnified spectra at 4.0–4.2 ppm were also shown (right). The NMR spectra were collected by Herman Coceancigh. 2017, Copyright: American Chemical Society.

4.4 Conclusion

This study showed the permeability-based control of the electrochemical properties and catalytic activity of ferrocene-containing block copolymer films. A pristine PS-*b*-PAEFc film was redox-inactive in 0.1 M $NaPF_6$/EtOH due to its negligible compatibility with PS and PAEFc. In contrast, these films could be converted to be redox-active by oxidizing the ferrocene moieties in 0.1 M $TBAPF_6$/MeCN prior to the electrochemical measurements in the EtOH solution. The fraction of redox-active ferrocene moieties measured for the activated PS-*b*-PAEFc films in the EtOH solution was similar to that in the MeCN solution. However, the charge transport efficiency of the activated PS-*b*-PAEFc in the EtOH solution was significantly lower than that in the MeCN solution, reflecting the reduced mobility of the redox moieties and limited counter ion migration in the less-swollen films. The activated PS-*b*-PAEFc films were used as electrochemically-responsive heterogeneous catalysts for Michael addition reaction in the EtOH solution. Interestingly, the reaction selectivity could be controlled by the permeability of the

redox-inactive PS matrix. We believe the reaction can be accelerated by the use of a porous electrode with a high surface area as the support of a PS-*b*-PAEFc film. This work opens opportunities to develop redox-active block copolymers as electrochemically-responsive catalysts with a selectivity based on the microdomain permeability.

4.5 References

(1) Rider, D. A.; Manners, I. Synthesis, Self-Assembly, and Applications of Polyferrocenylsilane Block Copolymers. *Polym. Rev.* **2007**, *47*, 165-195.

(2) Ramanathan, M.; Tseng, Y.-C.; Ariga, K.; Darling, S. B. Emerging Trends in Metal-Containing Block Copolymers: Synthesis, Self-Assembly, and Nanomanufacturing Applications. *J. Mater. Chem. C* **2013**, *1*, 2080-2091.

(3) Zhou, J.; Whittell, G. R.; Manners, I. Metalloblock Copolymers: New Functional Nanomaterials. *Macromolecules* **2014**, *47*, 3529-3543.

(4) Hardy, C. G.; Zhang, J.; Yan, Y.; Ren, L.; Tang, C. Metallopolymers with Transition Metals in the Side-Chain by Living and Controlled Polymerization Techniques. *Prog. Polym. Sci.* **2014**, *39*, 1742-1796.

(5) Gallei, M. The Renaissance of Side-Chain Ferrocene-Containing Polymers: Scope and Limitations of Vinylferrocene and Ferrocenyl Methacrylates. *Macromol. Chem. Phys.* **2014**, *215*, 699-704.

(6) Pietschnig, R. Polymers with Pendant Ferrocenes. *Chem. Soc. Rev.* **2016**, *45*, 5216-5231.

(7) Park, C.; Yoon, J.; Thomas, E. L. Enabling Nanotechnology with Self Assembled Block Copolymer Patterns. *Polymer* **2003**, *44*, 6725-6760.

(8) Meuler, A. J.; Hillmyer, M. A.; Bates, F. S. Ordered Network Mesostructures in Block Polymer Materials. *Macromolecules* **2009**, *42*, 7221-7250.

(9) Ito, T. Block Copolymer-Derived Monolithic Polymer Films and Membranes Comprising Self-Organized Cylindrical Nanopores for Chemical Sensing and Separations. *Chem.– Asian J.* **2014**, *9*, 2708-2718.

(10) Durkee, D. A.; Eitouni, H. B.; Gomez, E. D.; Ellsworth, M. W.; Bell, A. T.; Balsara, N. P. Catalysts from Self-Assembled Organometallic Block Copolymers. *Adv. Mater.* **2005**, *17*, 2003-2006.

(11) Rüttiger, C.; Appold, M.; Didzoleit, H.; Eils, A.; Dietz, C.; Stark, R. W.; Stühn, B. Gallei, M. Structure Formation of Metallopolymer-Grafted Block Copolymers. *Macromolecules.* **2016**. *49*, 3415-3426.

(12) Behzadi, S.; Gallei, M.; Elbert, J.; Appold, M.; Glasser, G.; Landfester, K.; Crespy, D. A Triblock Terpolymer vs. Blends of Diblock Copolymers for Nanocapsules Addressed by Three Independent Stimuli. *Polym. Chem.* **2016**, *7*, 3434-3443.

(13) Chen, T.; Wang, L.; Jiang, G.; Wang, J.; Dong, X.; Wang, X.; Zhou, J.; Wang, C.; Wang, W. Electrochemical Behavior of Poly(ferrocenyldimethylsilane-*b*-dimethylsiloxane) Films. *J. Phys. Chem. B* **2005**, *109*, 4624-4630.

(14) Garcia Armada, M. P.; Losada, J.; Lopez-Villanueva, F. J.; Frey, H.; Alonso, B.; Casado, C. M. Electrochemical and Bioelectrocatalytical Properties of Novel Block-Copolymers Containing Interacting Ferrocenyl Units. *J. Organomet. Chem.* **2008**, *693*, 2803-2811.

(15) Lee, J.; Ahn, H.; Choi, I.; Boese, M.; Park, M. J. Enhanced Charge Transport in Enzyme-Wired Organometallic Block Copolymers for Bioenergy and Biosensors. *Macromolecules* **2012**, *45*, 3121-3128.

(16) Eloi, J.-C.; Jones, S. E. W.; Poor, V.; Okuda, M.; Gwyther, J.; Schwarzacher, W. Electrochemically Triggered Selective Adsorption of Biotemplated Nanoparticles on Self-Assembled Organometallic Diblock Copolymer Thin Films. *Adv. Funct. Mater.* **2012**, *22*, 3273-3278.

(17) Ghimire, G.; Yi, Y.; Derylo, M. A.; Baker, L. A.; Ito, T. Electron Propagation within Redox-Active Microdomains in Thin Films of Ferrocene-Containing Diblock Copolymers. *Langmuir* **2015**, *31*, 12307-12314.

(18) Oyama, N.; Anson, F. C. Factors Affecting the Electrochemical Responses of Metal-Complexes at Pyrolytic-Graphite Electrodes Coated with Films of Poly(4-Vinylpyridine). *J. Electrochem. Soc.* **1980**, *127*, 640-647.

(19) Blauch, D. N.; Saveant, J.-M. Dynamics of Electron Hopping in Assemblies of Redox Centers - Percolation and Diffusion. *J. Am. Chem. Soc.* **1992**, *114*, 3323-3332.

(20) Murray, R. W. Polymer Modification of Electrodes. *Annu. Rev. Mater. Sci.* **1984**, *14*, 145-169.

(21) Heller, A. Electrical Connection of Enzyme Redox Centers to Electrodes. *J. Phys. Chem.* **1992**, *96*, 3579-3587.

(22) Majda, M.: Dynamics of Electron Transport in Polymeric Assemblies of Redox Centers. In *Molecular Design of Electrode Surfaces*; Murray, R. W., Ed.; John Wiley & Sons: New York, 1992; pp 159-206.

(23) Terrill, R. H.; Murray, R. W.: Electron Hopping Transport in Electrochemically Active, Molecular Mixed Valent Materials. In *Molecular Electronics: A 'Chemistry for the 21st Century' Monograph*; Jortner, J., Ratner, M., Eds.; Blackwell Science: Malden, MA, 1997; pp 215-239.

(24) Peerce, P. J.; Bard, A. J. Polymer-Films on Electrodes. Part III. Digital-Simulation Model for Cyclic Voltammetry of Electroactive Polymer Film and Electrochemistry of Poly(Vinylferrocene) on Platinum. *J. Electroanal. Chem.* **1980**, *114*, 89-115.

(25) Hunter, T. B.; Tyler, P. S.; Smyrl, W. H.; White, H. S. Impedance Analysis of Poly(Vinylferrocene) Films - The Dependence of Diffusional Charge Transport and Exchange Current-Density on Polymer Oxidation-State. *J. Electrochem. Soc.* **1987**, *134*, 2198-2204.

(26) Inzelt, G.; Szabo, L. The Effect of the Nature and the Concentration of Counter Ions on the Electrochemistry of Poly(Vinylferrocene) Polymer Film Electrodes. *Electrochim. Acta* **1986**, *31*, 1381-1387.

(27) Varineau, P. T.; Buttry, D. A. Applications of the Quartz Crystal Microbalance to Electrochemistry - Measurement of Ion and Solvent Populations in Thin-Films of Poly(Vinylferrocene) as Functions of Redox State. *J. Phys. Chem.* **1987**, *91*, 1292-1295.

(28) Daum, P.; Murray, R. W. Chemically Modified Electrodes. Part XXII. Solvent Effects on the Electrochemistry of Thin-Films of Plasma Polymerized Vinylferrocene. *J. Electroanal. Chem.* **1979**, *103*, 289-294.

(29) Daum, P.; Murray, R. W. Charge-Transfer Diffusion Rates and Activity Relationships during Oxidation and Reduction of Plasma-Polymerized Vinylferrocene Films. *J. Phys. Chem.* **1981**, *85*, 389-396.

(30) Kim, B. Y.; Ratcliff, E. L.; Armstrong, N. R.; Kowalewski, T.; Pyun, J. Ferrocene Functional Polymer Brushes on Indium Tin Oxide via Surface-Initiated Atom Transfer Radical Polymerization. *Langmuir* **2010**, *26*, 2083-2092.

(31) Plamper, F. A. Changing Polymer Solvation by Electrochemical Means: Basics and Applications. *Adv. Polym. Sci.* **2015**, *266*, 125-212.

(32) Bridges, T. E.; Uibel, R. H.; Harris, J. M. Measuring Diffusion of Molecules into Individual Polymer Particles by Confocal Raman Microscopy. *Anal. Chem.* **2006**, *78*, 2121-2129.

(33) Errede, L. A. Polymer Swelling. 7. A Molecular Interpretation of Polymer Swelling. *J. Phys. Chem.* **1989**, *93*, 2668-2671.

(34) Elbert, J.; Mersini, J.; Vilbrandt, N.; Lederle, C.; Kraska, M.; Gallei, M.; Stühn, B. Plenio, H.; Rehahn, M. Reversible Activity Modulation of Surface-Attached Grubbs Second Generation Type Catalysts Using Redox-Responsive Polymers. *Macromolecules.* **2013.** *46*, 4255-4267.

(35) Mao, X.; Tian, W.; Wu, J.; Rutledge, G. C.; Hatton, T. A. Electrochemically Responsive Heterogeneous Catalysis for Controlling Reaction Kinetics. *J. Am. Chem. Soc.* **2015**, *137*, 1348-1355.

(36) Hardy, C. G.; Ren, L.; Tamboue, T. C.; Tang, C. Side-Chain Ferrocene-Containing (Meth)acrylate Polymers: Synthesis and Properties. *J. Polym. Sci. Part A: Polym. Chem.* **2011**, *49*, 1409-1420.

(37) Li, F.; Pandey, B.; Ito, T. Linker-Based Control of Electron Propagation through Ferrocene Moieties Covalently Anchored onto Insulator-Based Nanopores Derived from a Polystyrene-Poly(methylmethacrylate) Diblock Copolymer. *Langmuir* **2012**, *28*, 16496-16500.

(38) Li, F.; Ito, T. Complexation-Induced Control of Electron Propagation Based on Bounded Diffusion through Nanopore-Tethered Ferrocenes. *J. Am. Chem. Soc.* **2013**, *135*, 16260-16263.

(39) Bard, A. J.; Faulkner, L. R.: *Electrochemical Methods, Fundamentals and Applications*; Second Edition ed.; Wiley: New York, 2001.

(40) Ju, H.; Leech, D. Electrochemistry of Poly(vinylferrocene) Formed by Direct Electrochemical Reduction at a Glassy Carbon Electrode. *J. Chem. Soc., Faraday Trans.* **1997**, *93*, 1371-1375.

(41) Christoffer, J. 2-(3-Oxobutyl)cyclopentanone-2-carboxylic Acid Ethyl Ester. *Org. Synth.* **2002**, *78*, 249.

Chapter 5 - Diffusion Behavior of Differently Charged Molecules in Self-Assembled Organic Nanotubes Studied Using Imaging Fluorescence Correlation Spectroscopy

Reproduced with permission from American Chemical Society.

Published as: G. Ghimire, R. Espinoza, H. Xu, S. Nagasaka, N. Kameta, M. Masuda, D.A. Higgins, T.Ito, *Langmuir*, **2019**, *35*, 7783-7790.

Contribution of the Authors

DAH and TI designed this project. NK and MM synthesized the bolaamphiphile and characterized its ONTs using transmission electron microscopy (TEM). RE collected some of the preliminary data which was not used in this chapter. HX mentored me how to use the wide-field fluorescence microscope. SN prepared the dispersed ONT samples. DAH wrote the LabView and Igor Pro programs where autocorrelation and data fitting were conducted. GG collected all the imaging-FCS and UV-Vis data, and GG and TI analyzed the data.

5.1 Introduction

Nanotubes based on inorganic[1-4] and organic materials[1,5-8] have recently been explored for use as drug delivery vehicles and contaminant adsorbents because of their ability to encapsulate solute molecules into their cylindrical hollow spaces. In addition, these materials have high loading capacity due to their large effective surface area. For drug delivery applications, these materials exhibit the slower release of loaded solutes from the open ends of the tubes. The efficiency of the loading/release of solutes into/from these materials is regulated by steric, electrostatic, and chemical interactions with the openings and inner wall surface. In particular,

these molecular interactions with the inner surface play key roles in controlling the rate and selectivity of molecular release.[1,3,7] Interestingly, it has been reported that nanoscale cavities afford unique environments that enhance molecular interactions owing to the nanoconfinement of solute species.[9,10] Thus, a thorough understanding of solute-nanotube interactions is crucial to the design of nanotube-based materials optimized for the aforementioned applications. In addition, the precise control of molecular loading/release requires the use of multiple nanotubes having identical molecular transport properties. Thus, it is important to fully understand the level of heterogeneity exhibited by the nanotubes, which is best studied one nanotube at a time rather than by probing the ensemble-averaged properties of multiple nanotubes.

Among nanotubular materials, organic nanotubes (ONTs) consisting of asymmetrical bolaamphiphiles have attracted considerable interest as drug delivery vehicles.[7,8] Rationally-designed bolaamphiphiles can self-assemble to form uniform cylindrical tubular structures with a very narrow size distribution on the basis of rolled bolaamphiphile layer(s). The inner and outer tube diameters are controllable in the range of 2 – 100 nm and 6 – 120 nm, respectively, by adjusting the chemical structure(s) of the constituent bolaamphiphile(s) and their arrangement in the rolled layer(s). More uniquely, these ONTs have distinct chemical compositions on their inner and outer surfaces that reflect the terminal functional groups of the asymmetrical bolaamphiphile(s),[11] in contrast to many other organic,[1,5] inorganic,[1-4] and lipid bilayer[6] nanotubes that have identical inner and outer surface compositions. The distinct surface compositions permit the functionalization of the inner surface for efficient loading and controlled release, independently of the outer surface, which can be modified for improved biocompatibility and selective target recognition. Owing to their structural and chemical characteristics, these ONTs exhibit a number of unique properties that make them suitable for drug delivery

applications, including low toxicity,[12] stimulus-responsive molecular release,[13-15] sustained molecular release,[15] the loading/release of poorly water-soluble molecules,[16,17] and the stabilization of proteins.[18] Among these properties, the loading properties of ONTs were evaluated by the visualization of species encapsulated within individual ONTs using transmission electron microscopy,[19] small-angle X-ray scattering,[20] and by solid-state NMR measurements of molecule-nanotube interactions.[17] However, these results provide negligible information on the dynamic behavior of solutes loaded into ONTs. The release properties of ONTs were assessed by spectrometric measurements of different solute molecules released from a batch of ONTs.[13-15,17] The release properties were controlled by interactions between solutes and the ONT inner surfaces, and thus could be tuned by adjusting the diameter and surface functionality of the ONTs as well as solution conditions such as pH. However, the release rates measured represent the ensemble-averaged properties of multiple ONTs, and thus do not reveal whether the individual ONTs have homogeneous release characteristics.

At the molecular level, the loading/release of molecules is controlled by their diffusion and adsorption/desorption under the influence of steric, electrostatic, and chemical interactions within the ONTs. The apparent diffusion coefficient of molecules within single tubular materials has been measured using fluorescence techniques,[21,22] including fluorescence resonance energy transfer (FRET) imaging,[13,19,23] fluorescence recovery after photobleaching (FRAP),[24-26] confocal fluorescence correlation spectroscopy (FCS),[25] and imaging FCS.[27,28] FRET imaging successfully revealed the slow diffusion of fluorescently-labeled biomolecules and nanoparticles within ONTs that was attributable to steric and electrostatic interactions.[13,19,23] However, this method cannot be used to investigate the molecular permeability of native ONTs, because the nanotube inner surface needs be modified with a donor or acceptor chromophore to visualize the

diffusion of fluorescent species. FRAP was used to quantify molecular diffusion along the long axis of tubular materials.[24-26] However, FRAP is applicable only for relatively long tubes (> 10 μm) due to the requirement that a μm-scale area be photobleached. Such long tubular materials may not be suitable as drug delivery vehicles or contaminant adsorbents. Confocal FCS showed the involvement of multiple processes in molecular diffusion within sub-μm-scale regions of a lipid tubule.[25] These processes were represented by multiple diffusion coefficients that were obtained by autocorrelation of temporal fluorescence intensity fluctuations that originated from molecular diffusion across the focal volume of a laser beam.[29] This method can measure fast moving species due to the high temporal resolution of the single point detector employed (~ μsec), but requires a long time to map local diffusion coefficients in a single tubule. In contrast to these methods, imaging FCS provides a quicker means to simultaneously measure the local apparent diffusion coefficients (D_{local}) of fluorescent molecules along the full length of individual nanotubes.[29] This method employs a wide-field fluorescence microscope to record videos of individual nanotubes. Temporal fluorescence intensity fluctuations at each of the pixels are autocorrelated to obtain D_{local} at all the pixels on a nanotube, though fast diffusion processes cannot be detected due to the limited temporal resolution (~ msec) of a CCD camera. Previously, we employed imaging FCS to measure the effects of electrostatic interactions on the diffusion of anionic sulforhodamine B (SRB; **Figure 5.1a**)[27] and the diffusion and distribution of solvatochromic fluorescent probes[28] within 10-nm diameter ONTs having inner surface amine groups with pK_a of ~ 7.27[13] (NH_2-ONT_{10nm}; **Figure 5.1b** and **Figure 5.2**). In the former,[27] the D_{local} of SRB in the ONTs was measured in aqueous phosphate buffer saline (PBS) solutions of different ionic strengths (I = 1 – 500 mM) and pH (pH 6.4 – 8.4), and was shown to be controlled by electrostatic attraction with protonated amine groups on the inner ONT surface. In the

latter,[28] two-color imaging FCS was used to simultaneously assess the diffusion and distribution of Nile Red (NR) and its hydroxylated derivative (NR-OH) within the ONTs in ethanol. As compared with NR, NR-OH located in more polar environments and diffused more slowly due to hydrogen bonding interactions with the functional groups of the ONTs.

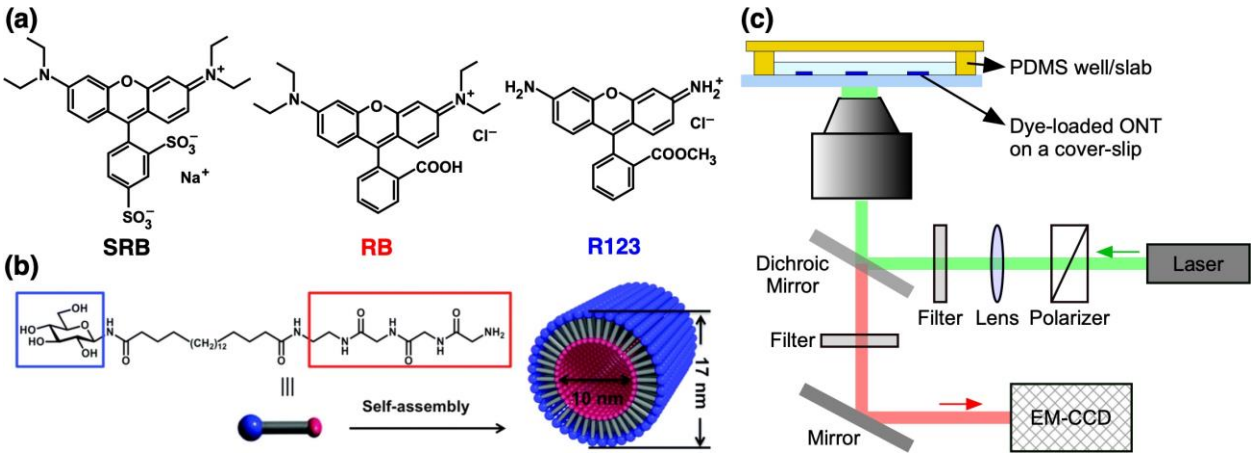

Figure 5.1 (a) Molecular structures of fluorescent dyes employed in this study: sulforhodamine B (SRB), rhodamine B (RB) and rhodamine-123 (R123). (b) Molecular structure of bolaamphiphile monomer and schematic illustration of a bolaamphiphile-based organic nanotube (ONT) formed from the monomer via self-assembly. Reproduced from Xu, H.; Nagasaka, S.; Kameta, N.; Masuda, M.; Ito, T.; Higgins, D. A. *Phys. Chem. Chem. Phys*. **2016**, *18*, 16766-16774 (ref. 27) – Published by the PCCP Owner Societies. 2019. (c) Experimental setup used in this study. Copyright: American Chemical Society.

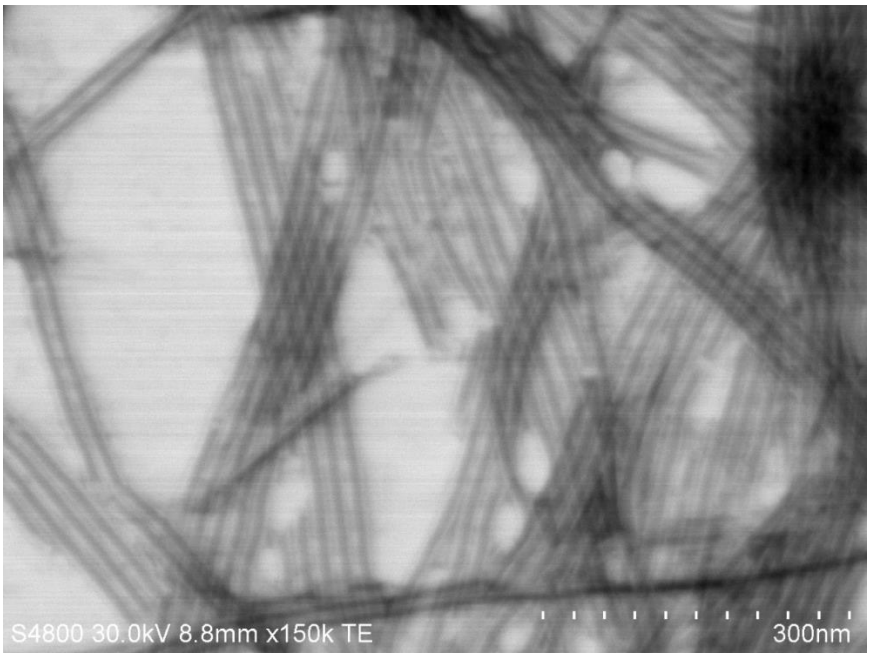

Figure 5.2 Scanning-TEM image of NH_2-$ONTs_{10nm}$ that were negatively stained by 2wt% phosphotungstate. The hollow cylinder space is shown as the relatively darker area compared with the surroundings. The image was collected by Dr. Kameta. 2019, Copyright: American Chemical Society.

This Chapter discussed the diffusion behavior of differently charged fluorescent probes (**Figure 5.1a**) within NH_2-ONT_{10nm} in aqueous PBS solutions of different pH and ionic strengths. Anionic SRB, zwitterionic/cationic rhodamine B (RB), and cationic rhodamine 123 (R123) were employed as probe molecules to understand how the net charge on the probe and its hydrophobicity affect its diffusion behavior within the amine-terminated nanotubes. This study is an extension of our previous work with SRB and NH_2-ONT_{10nm}[27] with the use of multiple fluorescent molecules over a wider pH range (pH 3.4 – 8.4). The measurements at the wider pH range will permit us to assess the influences of the protonation of RB on its diffusion behavior in the ONTs. A thorough diffusion study with the different probe molecules under different solution conditions will provide basic insight into molecule-nanopore interactions controlling the molecular loading/release properties of nanotubular materials with multiple chemical

environments. In addition, this study demonstrates that imaging FCS is a convenient tool to assess the homogeneity of the molecular diffusion properties within individual ONTs.

5.2 Experimental Section

5.2.1 Chemicals and Materials

NH_2-$ONTs_{10nm}$ having lengths of 2-5 μm were formed from *N*-(*β*-D-glucopyranosyl)-N'-(2-glycylglycylglycine-amideethyl)-icosane-diamide, which has terminal amine and glucose headgroups linked by a hydrophobic spacer (**Figure 5.1b**), according to a procedure reported previously.[15,27] TEM image of the ONTs (**Figure 5.2**) reveals their cylindrical hollow structures with a diameter of 10 nm. Rhodamine-123 (R123; Aldrich), rhodamine B (RB; Aldrich), sulforhodamine B (SRB; Acros Organics), phosphate buffered saline (P5368; Aldrich), which yields one liter of 0.01 M phosphate buffered saline containing 0.138 M NaCl and 0.0027 M KCl, 1-octanol (Aldrich) , hydrochloric acid (HCl; Fisher), sodium hydroxide (NaOH; Fisher) and o-phosphoric acid (Fisher Scientific) were used as received. All aqueous solutions were prepared with water having a resistivity of 18 MΩ cm or higher (Barnstead Nanopure Systems).

5.2.2 Determination of the Acid Dissociation Constants (pK_a) and Octanol/Water Partition Coefficients (logP_{oct}) of the Dyes

The pK_a and logP_{oct} values of R123, RB and SRB were determined from their UV-Vis absorption spectra recorded using an Agilent Cary 60 UV-Vis spectrophotometer. The pK_a values were measured in aqueous solutions of 3.6 μM SRB, 4.8 μM RB or 4.5 μM R123 containing 20 mM o-phosphoric acid at different pH that was adjusted by adding a NaOH solution. The solution pH was measured using a Fisher Accumet pH glass electrode. For determination of the logP_{oct} values,[30] 1-octanol saturated with water and water saturated with 1-octanol (pH ~ 5.4) were employed. Five milliliters of an aqueous dye solution (5 μM) was

mechanically shaken with an equal volume of 1-octanol in a glass test tube wrapped with aluminum foil for ≥ 1 hour at room temperature (ca. 25 °C). The resulting mixture was then centrifuged to obtain the aqueous phase for a UV-Vis spectroscopic measurement.

5.2.3 Sample Preparation for Imaging FCS Experiments

NH_2-ONT_{10nm} was deposited from a turbid aqueous solution (0.1 mg/mL) onto plasma-cleaned glass coverslips (FisherFinest Premium; 25 x 25 μm^2) as reported previously.[27,28] The resulting ONT-coated coverslips were covered with aqueous solution (200 µL) containing 1 µM SRB, 50 nM RB, or 50 nM R123 for 2 hours, rinsed carefully with water, and then dried with Ar or N_2. Fluorescence videos of the ONTs were recorded in PBS solutions of different pH and ionic strengths. These solutions were loaded into a rectangular polydimethylsiloxane (PDMS) well that was attached to the coverslip, and subsequently covered with a PDMS slab (**Figure 5.1c**). The solution pH was adjusted by adding aqueous HCl (~ 0.15 M) or NaOH (~ 0.25 M) solutions. It should be noted that the different dyes required different loading concentrations to observe the fluctuation of fluorescence intensity induced by dye diffusion, because the more hydrophobic RB and R123 were loaded more efficiently into the NH_2-ONT_{10nm} than SRB. We have empirically found that the fluorescence intensity most suitable for imaging FCS measurements was in the range of 120 – 250 cps at each pixel on the ONTs and that was achieved by optimizing the concentration of dye solution used for doping.

5.2.4 Imaging FCS Measurements

Imaging FCS data were recorded using the experimental setup shown in **Figure 5.1c**. An inverted epi-illumination microscope (Nikon TiE) was used for the acquisition of fluorescence videos, as described previously.[31] An argon ion laser (514 nm) was used for SRB- and RB-doped ONTs, and a blue diode laser (488 nm) was used for R123-doped ONTs. Total internal

reflection fluorescence (TIRF) mode was employed to reduce background fluorescence. A dichroic beam splitter (555 DCLP for SRB and RB, and 505 DCLP for R123) was used to introduce ca. 0.01 mW of laser light to the back aperture of an oil immersion objective lens (Nikon Apo TIRF 100x, 1.49 NA). Fluorescence collected by the objective lens was directed through the appropriate dichroic beam splitter and emission filter (Chroma 580/40 for RB and SRB, and 535/50 HQ for R123). Fluorescence videos of individual ONTs (25,000 frames; ~ 2.5 x 2.5 μm^2) were acquired using an EM-CCD camera (Andor iXon DU-897) with 2 ms exposure time, ~ 6.5 ms cycle time, 10 MHz readout rate, 3 x 3 binning, and an EM gain of 30.

The video files were analyzed using a program written in LabView (National Instruments). This software provided for background correction, autocorrelation, and pixel by pixel fitting of the data, as reported previously.[27] Specifically, time transient data at individual pixels were autocorrelated using **Equation 2.9.** The autocorrelation function was fitted to **Equation 2.10**, incorporating two decay components associated with 1D Fickian diffusion and photobleaching.[27,32]

5.3 Results and Discussion

5.3.1 Fluorescent Molecules Loaded into NH_2-ONT_{10nm}

In this study, the diffusion of anionic SRB, zwitterionic/cationic RB, and cationic R123 in NH_2-ONT_{10nm} (pK_a ~ 7.27 for the amine groups on the inner surface)[13] was measured at different pH and ionic strengths using imaging FCS. **Table 5.1** summarizes the pK_a and logP_{oct} values of these fluorescent dyes, as determined using UV-Vis absorption spectrometry (**Figures 5.3** and **5.4**).

Table 5.1 Acid Dissociation Constants (pK_a)[a] and 1-Octanol/Water Partition Coefficients ($\log P_{oct}$)[b] of the Fluorescent Molecules Used in This Study. 2019, Copyright: American Chemical Society.

Fluorescent Dyes	pK_a	$\log P_{oct}$
SRB	< 2.1	$-1.9_0 \pm 0.8_0$
RB	~ 3.2	$1.5_8 \pm 0.0_1$
R123	> 8.7	$0.20_6 \pm 0.20_8$

[a] Measured in aqueous phosphate solutions (20 mM) of pH 2 – 9 at room temperature (ca. 25 °C) using UV-Vis absorption spectrometry (**Figure 5.3**). [b] The 95% confidence intervals obtained from 3-4 measurements (**Figure 5.4**) at room temperature (ca. 25 °C). The pH of the water was ~ 5.4.

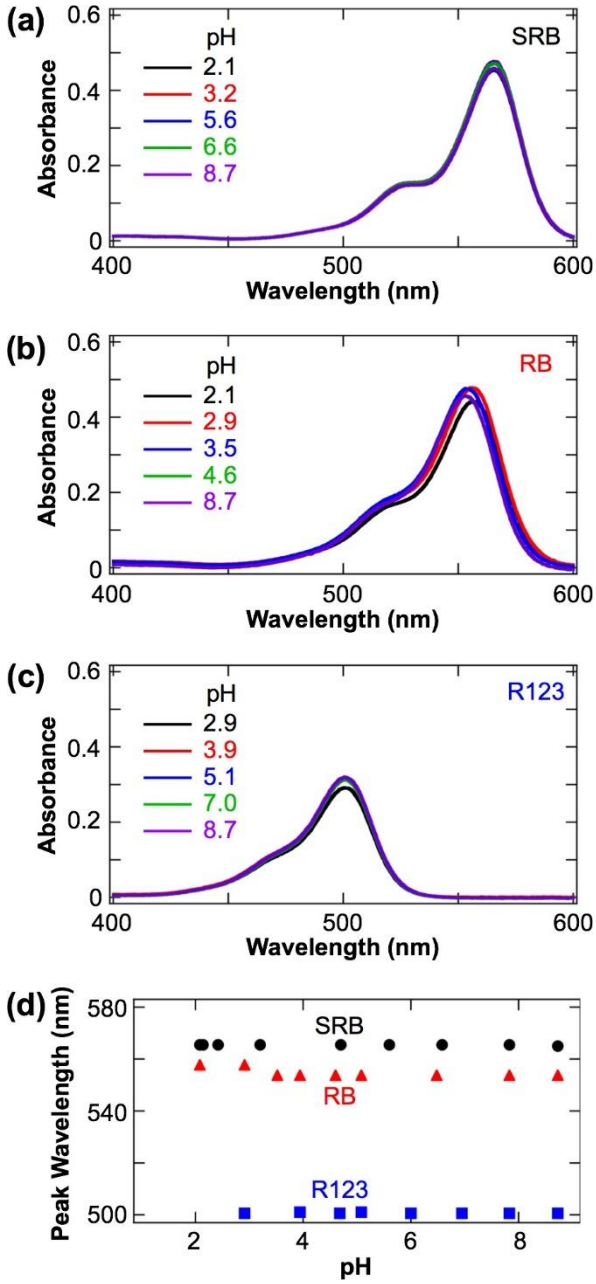

Figure 5.3 UV-Vis absorption spectra of **(a)** SRB, **(b)** RB and **(c)** R123 in aqueous phosphate solutions of different pH at room temperature (ca. 25 °C). **(d)** pH dependence of the absorption peak wavelengths of SRB (black circles), RB (red triangles) and R123 (blue squares). 2019, Copyright: American Chemical Society.

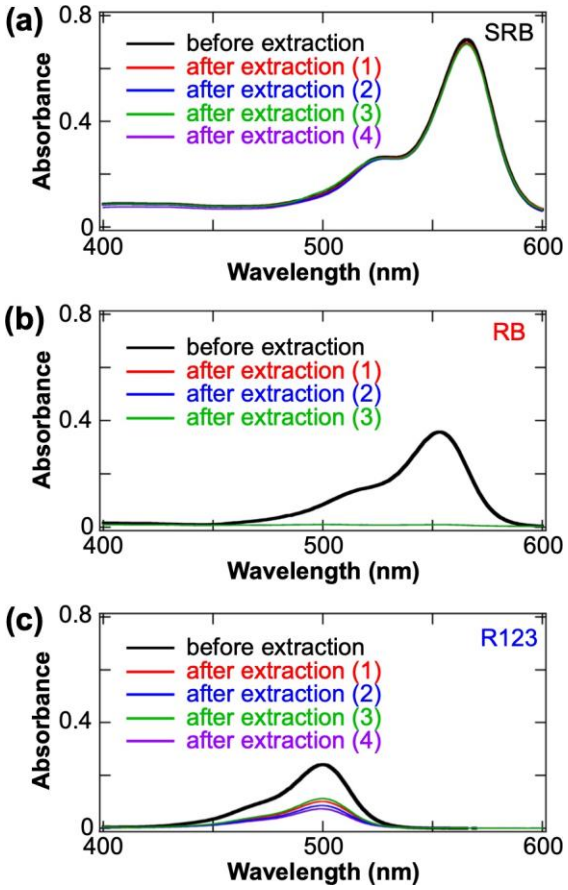

Figure 5.4 UV-Vis absorption spectra of **(a)** SRB, **(b)** RB and **(c)** R123 in water before (black) and after extraction. Results of 3 – 4 different solutions are shown. 2019, Copyright: American Chemical Society.

The pK_a values were determined from pH-dependent changes in the absorption peak wavelengths λ_{max}) of the dyes (**Figure 5.3**). SRB and R123 are anionic and cationic, respectively, in aqueous solution at pH 2 – 9, as indicated by negligible pH-induced change in λ_{max} (**Figure 5.3acd**). In contrast, RB exhibited a slight shift in λ_{max} from pH 2.9 (557 nm) to pH 3.5 (553 nm) (**Figure 5.3bd**), attributable to the deprotonation of the -COOH group. The pK_a of RB is estimated to be ~ 3.2, which is very close to its literature value,[36] indicating that RB is in the uncharged zwitterionic form at neutral to basic pH and protonates to its cationic form at lower pH.

The logP_{oct} values were spectrometrically estimated from the dye concentrations in the aqueous phase before and after extraction with 1-octanol (**Figure 5.4**). As summarized in **Table 5.1**, the hydrophobicity of the three dyes decreases in the order of RB > R123 > SRB. Of note, the extraction experiments were performed with water (pH ~ 5.4), and thus the logP_{oct} value of RB represents the hydrophobicity of its uncharged, zwitterionic form. The logP_{oct} value of protonated RB may be significantly smaller due to its positive net charge.

5.3.2 Imaging FCS Measurements of Dye-Doped ONTs

Imaging FCS provides a simple means to measure D_{local} on individual ONTs from single fluorescence videos. **Figure 5.5a** shows representative fluorescence microscopy images of NH_2-$ONTs_{10nm}$ doped by SRB, RB, or R123 that were measured in a PBS solution (I ~ 160 mM) at pH 7.4. These images are obtained by averaging the fluorescence across the 25,000 frames of the videos. The widths of these ONTs were significantly larger than the actual width (17 nm) owing to the pixel size (187.5 nm) and the diffraction-limited spatial resolution (220 – 240 nm at λ_{em} = 535 – 580 nm). Spatial variations in the fluorescence intensity from the ONTs implies a non-uniform distribution of the relatively small number of dye molecules in the ONTs. More importantly, each pixel over the ONTs exhibited temporal fluctuations in the fluorescence intensity attributable to the diffusion of individual dye molecules in and out of the detection volume, in addition to a gradual decrease in fluorescence intensity due to photobleaching (**Figure 5.5b**). **Equation 2.9** was used to obtain an autocorrelation function (**Figure 5.5c**) from the time transient data, which was fitted by **Equation 2.10** to obtain A and D_{local}. It is important to note that choice of the time lag (τ) played an important role in data analyses to calculate D_{local}. We found that D_{local} peaks at certain time lag (τ_{peak}) and that was determined by plotting maximum time lag (τ_{max}) of 100 – 600 frames against D_{local} as shown in **Figure 5.6** for pixels

highlighted in **Figure 5.5a**. Optimized τ of 320 frames was obtained from the averages of τ_{peak} from about 10 pixels of respective dye doped ONTs. These values obtained at each of the pixels were plotted to obtain composite images of the ONTs, in which the normalized *A* was shown as height and D_{local} was depicted by the color scale (**Figure 5.5d**). D_{local} varied in the range of 0.01 – 0.12 $\mu m^2/s$ with negligible position dependence along the ONTs, reflecting the random variation of local environment for molecular diffusion.[27] There was no clear correlation between *A* and D_{local}, suggesting the random distribution of mobile molecules within the ONTs. Most importantly, the D_{local} values of these dyes in the ONTs were significantly smaller than those in aqueous solution (~ 4 x 10^2 $\mu m^2/s$)[37] and those estimated using the hindered diffusion models,[38,39] reflecting the involvement of short-timescale adsorption and partition processes in molecular transport within the ONTs.[27]

5.3.3 Effects of NH_2-ONT_{10nm} Length on Molecular Transport

Fluorescence microscopy videos also afforded the lengths of individual ONTs, and thus permitted us to investigate a possible relationship between the length and molecular transport properties of individual ONTs. The apparent diffusion coefficient of the dye within each ONT (D_{ONT}) was calculated from D_{local} values obtained at ten different pixels along the ONT. **Figures 5.7** and **5.8** reveal that D_{ONT} was independent of ONT length for each of the dyes and solution conditions examined in this study. For example, **Figure 6e** shows similar D_{ONT} values for five SRB-doped ONTs (black circles) that were significantly larger than those for five RB-doped ONTs (red triangles) and four R123-doped ONTs (blue squares). The negligible dependence of D_{ONT} on ONT length was also found for the other pH and *I* conditions (**Figures 5.7 and 5.8**). D_{ONT} tended to be larger in the order of RB ≥ R123 ≥ SRB at pH 3.4 (**Figure 5.7a-d**) and SRB > RB ~ R123 at pH 7.4 (**Figure 5.7e-h**). Most importantly, the similarity in D_{ONT}, in spite of the

variation of D_{local} as represented by the error bars of D_{ONT}, suggested that the ONTs in each batch were homogeneous in terms of their solute loading and release properties. These results clarified the unique capability of imaging FCS to measure the detailed properties of individual nanotubular materials.

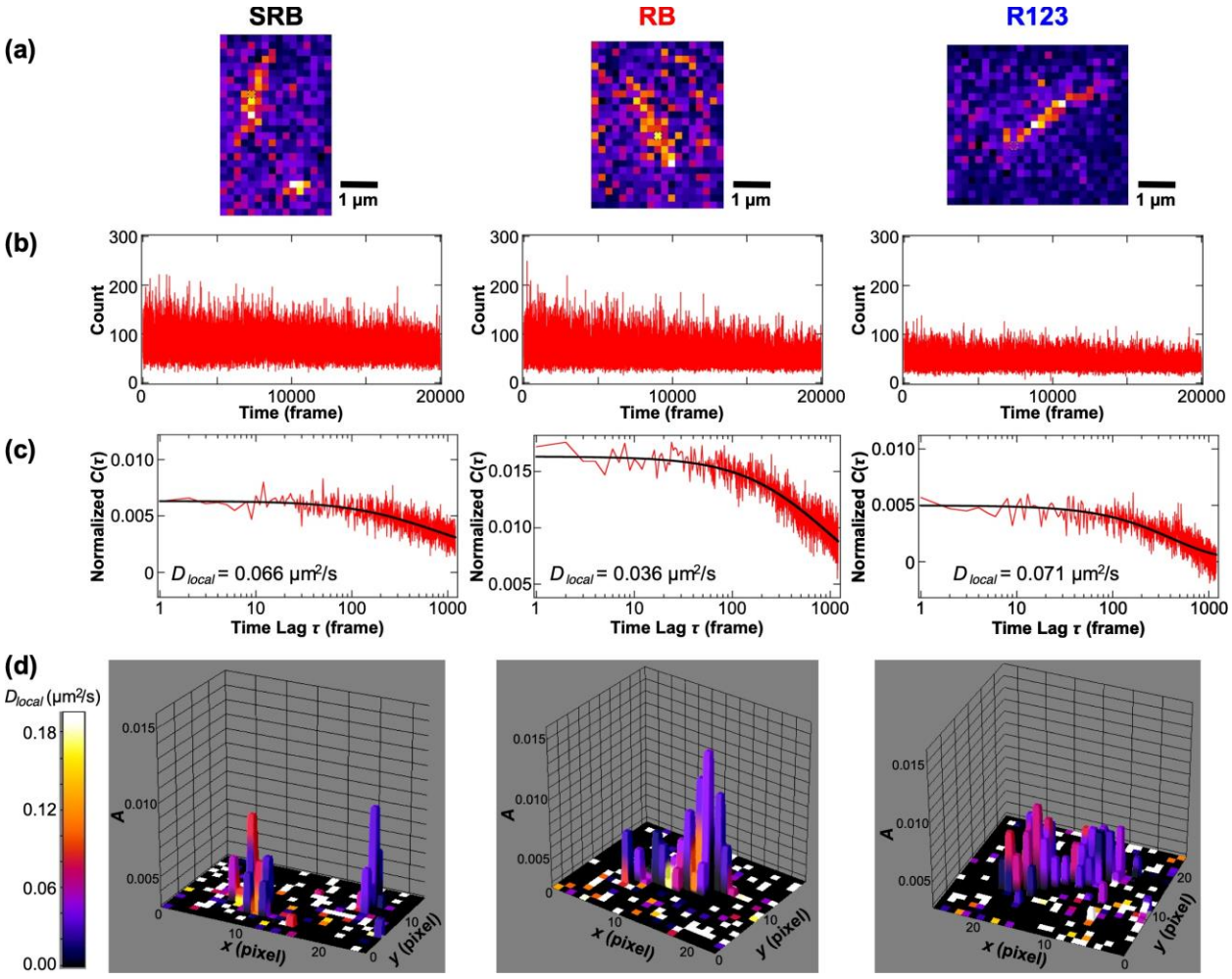

Figure 5.5 (a) Representative fluorescence images of ONTs doped by SRB, RB and R123 that were measured at pH 7.4 and the ionic strength of 160 mM. The images were obtained by averaging the fluorescence across the 25,000 frames of the videos. **(b)** Time transient data from pixels highlighted in each of the fluorescence images shown in **(a)**. **(c)** Autocorrelation functions obtained from the time transient data shown in **(b)**. The black solid lines depict the fitted curves that gave the autocorrelation amplitude, A, and D_{local} in **Equation 2.10**. D_{local} values obtained by the fitting are shown. **(d)** 3D plots for each of the ONTs, indicating A shown as height and D_{local} depicted by the color scale. 2019, Copyright: American Chemical Society.

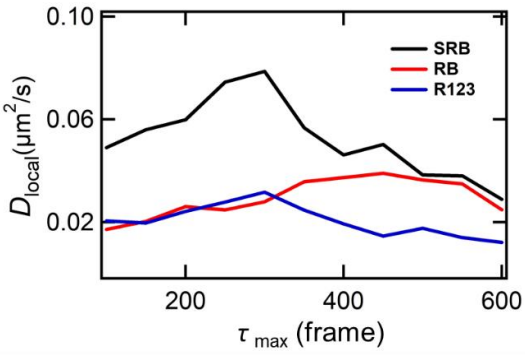

Figure 5.6 Relation between τ_{max} and D_{local} for highlighted pixels in **Figure 5.5a** for SRB (black), RB (red) and R123 (blue), respectively. 2019, Copyright: American Chemical Society.

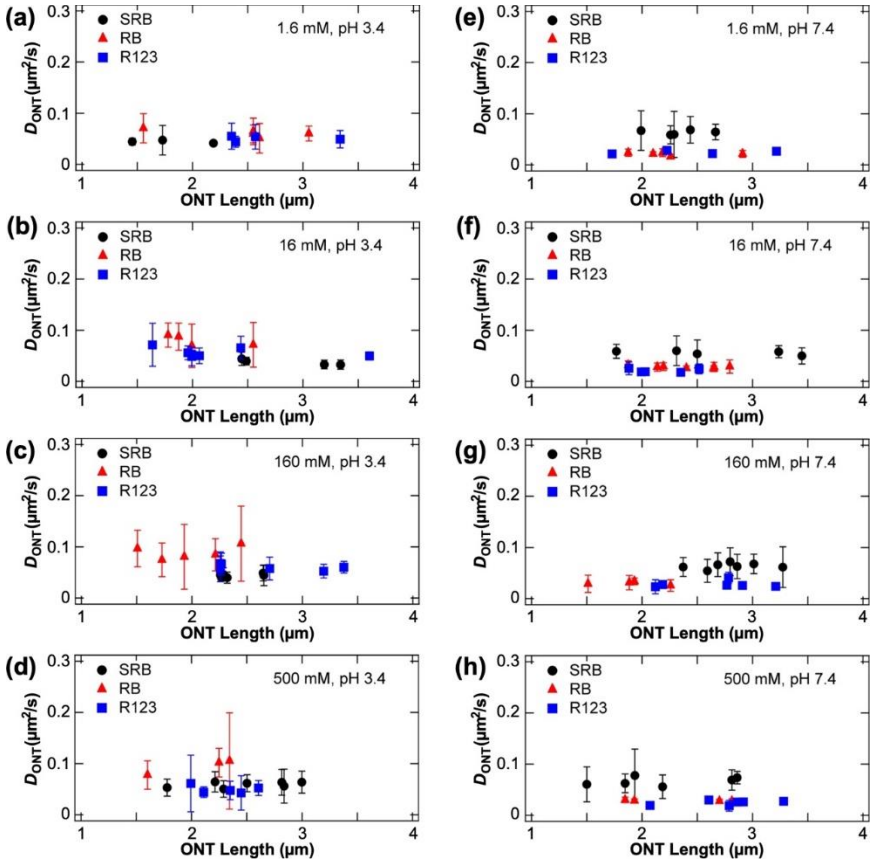

Figure 5.7 Relationship between D_{ONT} and ONT length obtained for SRB (black circles), RB (red triangles) and R123 (blue squares) at **(a-d)** pH 3.4 and **(e-h)** pH 7.4 with the ionic strengths of **(a, e)** ca. 1.6 mM, **(b, f)** ca. 16 mM, **(c, g)** ca. 160 mM and **(d, h)** ca. 500 mM. Data at the other pH conditions are shown in **Figure 5.8**. Error bars represent the 95% confidence interval of D_{local} obtained at ten different positions (pixels) for each ONT. 2019, Copyright: American Chemical Society.

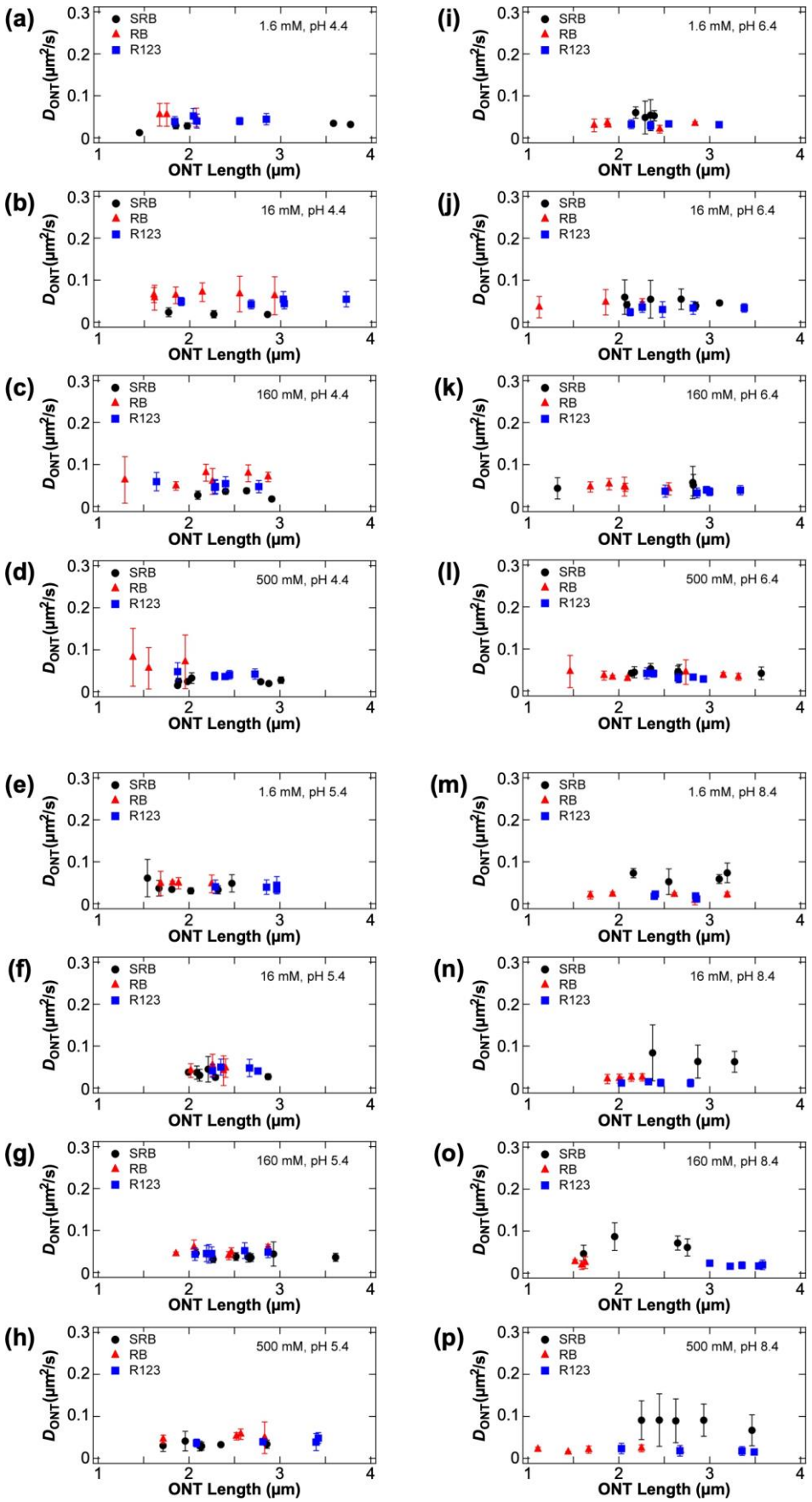
(a)
1.6 mM, pH 4.4
(b)
16 mM, pH 4.4
(c)
160 mM, pH 4.4
(d)
500 mM, pH 4.4
(e)
1.6 mM, pH 5.4
(f)
16 mM, pH 5.4
(g)
160 mM, pH 5.4
(h)
500 mM, pH 5.4
(i)
1.6 mM, pH 6.4
(j)
16 mM, pH 6.4
(k)
160 mM, pH 6.4
(l)
500 mM, pH 6.4
(m)
1.6 mM, pH 8.4
(n)
16 mM, pH 8.4
(o)
160 mM, pH 8.4
(p)
500 mM, pH 8.4
SRB
RB
R123
D_{ONT}(μm²/s)
ONT Length (μm)

Figure 5.8 Relationship between D_{ONT} and ONT length obtained for SRB (black circles), RB (red triangles) and R123 (blue squares) at **(a-d)** pH 4.4, **(e-h)** pH 5.4, **(i-l)** pH 6.4 and **(m-p)** pH 8.4 with the ionic strengths of **(a, e, i, m)** *ca*. 1.6 mM, **(b, f, j, n)** *ca*. 16 mM, **(c, g, k, o)** *ca*. 160 mM and **(d, h, l, p)** *ca*. 500 mM. Note that **Figure 5.8o** does not include a D_{ONT} data (= 0.088 ± 0.036 $\mu m^2/s$) obtained from a 4.8 μm-long, SRB-doped ONT. An error bar represents the 95% confidence interval of D_{local} values obtained at the ten different positions (pixels) of each ONT. 2019, Copyright: American Chemical Society.

5.3.4 Effects of pH on Apparent Diffusion Coefficient in NH_2-$ONTs_{10nm}$

The D_{ONT} values for individual ONTs were compiled to calculate ensemble-averaged diffusion coefficients (D). **Figure 5.9** shows a relationship between D and pH for the three dyes at the four different I. The error bars in these plots represent the variations of D_{ONT} values measured from multiple ONTs under identical solution conditions. The plots in **Figure 5.9** indicate that the D of the dyes was primarily controlled by electrostatic interaction with the nanotube surface: The diffusion of anionic SRB was mainly controlled by electrostatic attraction to the protonated amine groups[40] on the ONT inner surface ($pK_a \sim 7.27$),[13] as indicated by a decrease in D with decreasing pH from 8.4 to 4.4 (**Figure 5.9a**), as with previously reported results at pH 8.4 – 6.4.[27] An increase in D was unexpectedly observed from pH 4.4 to 3.4, which might be due to the protonation of the sulfonate groups ($pK_a < 2.1$ in aqueous solution; **Table 5.1**) enhanced by protonated amines on the ONT inner surface. The protonation converted SRB from its anionic to zwitterionic/uncharged forms, resulting in the reduction of electrostatic attraction to the protonated ONT surface. In contrast, cationic R123 exhibited the opposite trend: D increased with decreasing pH (**Figure 5.9c**) owing to the enhanced electrostatic repulsion of the cationic dye by the protonated amine groups. RB also showed an increase in D with decreasing pH (**Figure 5.9b**), which was attributable to electrostatic repulsion of its protonated, cationic form by the positive charge on the ONT inner surface. The continuous changes in D across a wide pH range (pH 3.4 – 8.4) could reflect the gradual protonation of the surface-

localized amine groups, as observed on self-assembled monolayers (SAMs).[41] Meanwhile, the higher *D* of RB as compared with R123 at all pH conditions investigated (see also **Figures 5.7** and **5.8**), might be associated with the reduced adsorption of the zwitterionic species onto the nanotube surface, as reported on SAMs.[42,43] These results verify the essential role of the ONT surface amine groups in their pH-dependent molecular loading and release for drug delivery applications.[13,14]

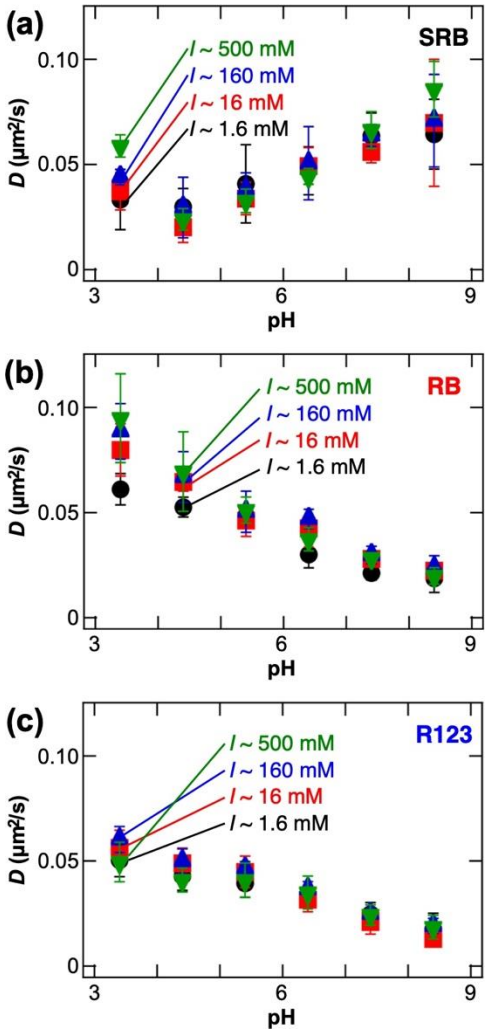

Figure 5.9 Apparent diffusion coefficients (*D*) of **(a)** SRB, **(b)** RB and **(c)** R123 as a function of pH (3.4 – 8.4) at the ionic strengths of ca. 1.6 (black circles), ca. 16 (red squares), ca. 160 (blue triangles) and ca. 500 mM (green inverse triangles). Error bars represent 95% confidence intervals obtained from 3 – 7 different ONTs. 2019, Copyright: American Chemical Society.

5.3.5 Effects of Ionic Strength on Apparent Diffusion Coefficient in NH_2-$ONTs_{10nm}$

The data shown in **Figure 5.9** were replotted in **Figures 5.10** and **5.11** to allow for the effects of ionic strength on *D* to be better visualized. **Figure 5.10** shows data obtained at pH 3.4, 6.4 and 8.4, and **Figure 5.11** depicts those obtained at the other pH conditions. These data show that *D* seems to increase with increasing *I* under some conditions, but not in others. The slight *I*-dependent increase in *D* could be explained by the screening of the dye charges and those of the ONT surface,[27] as is consistent with the pH dependence in *D* indicating the key role of electrostatic interactions in the molecular transport within NH_2-$ONTs_{10nm}$ (vide supra). However, the *I*-dependence of *D* was very small at most of the pH conditions. The weak dependence of *D* on *I* suggests the involvement of non-coulombic (hydrogen bonding and hydrophobic) interactions between the dye molecules and nanotube surfaces. Such interactions may enhance the adsorption and/or partitioning of the dyes to the ONT surfaces and/or walls on short timescales, resulting in the small diffusion coefficients obtained in this study (vide supra).

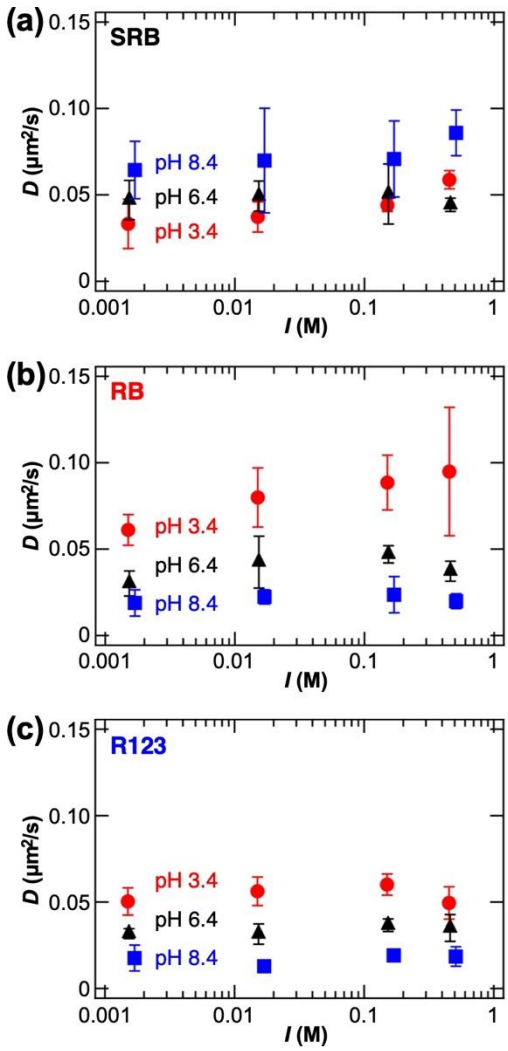

Figure 5.10 Apparent diffusion coefficients (*D*) of **(a)** SRB, **(b)** RB and **(c)** R123 as a function of ionic strength at pH 3.4 (red circles), 6.4 (black squares) and 8.4 (blue squares). Error bars represent 95% confidence intervals obtained from 3 – 7 different ONTs. 2019, Copyright: American Chemical Society.

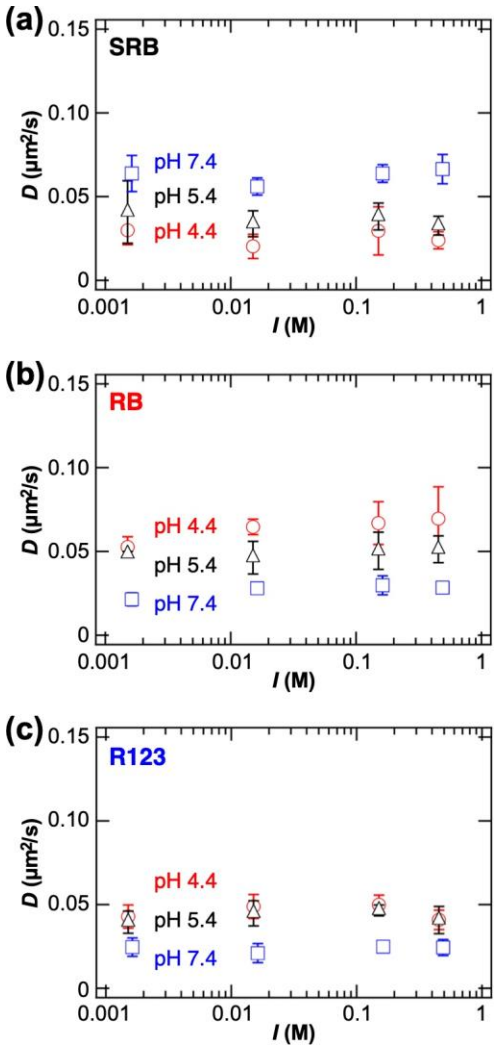

Figure 5.11 Apparent diffusion coefficients (*D*) of **(a)** SRB, **(b)** RB and **(c)** R123 as a function of ionic strength, *I*, at pH 4.4 (red open circles), 5.4 (black open squares) and 7.4 (blue open squares). Error bars represent 95% confidence intervals obtained from 3 – 7 different ONTs. 2019, Copyright: American Chemical Society.

5.6 Conclusion

In this study, we systematically investigated the effects of pH and *I* on the diffusion of three fluorescent dyes within NH_2-$ONTs_{10nm}$ using imaging FCS. Molecular diffusion within the ONT was mainly controlled by electrostatic interactions with the protonated amine groups on the inner ONT surfaces, as shown by the pH dependence of *D*. The continuous change in *D* over a wide pH range originated from the gradual protonation of the surface-localized amine groups as

well as the protonation of the acidic groups of the dyes within ONTs. The pH-dependent diffusion behavior could lead to the pH-responsive loading and release capability of NH_2-$ONTs_{10nm}$ for charged molecules.[13,14] The negligible influence of I on D suggested the involvement of non-coulombic interactions in molecular transport processes within the ONTs. These interactions may enhance dye adsorption to the ONT surface and/or dye partitioning to the ONT wall, resulting in the observation of the small apparent diffusion coefficients. Most importantly, the imaging FCS results revealed the heterogeneous nature of D_{local} in the ONTs, and also the fairly uniform D_{ONT} for a batch of ONTs. The homogeneity of the diffusion properties of individual ONTs could originate from the well-defined cylindrical hollow structures and the uniform diameters of the ONTs. An improved understanding of the fundamental properties of NH_2-$ONTs_{10nm}$, which incorporate multiple chemically distinct environments, will provide valuable insight into the future design of organic nanotubes as highly efficient drug delivery vehicles and contaminant adsorbents.

5.7 References

(1) Perry, J. L.; Martin, C. R.; Stewart, J. D. Drug-Delivery Strategies by Using Template-Synthesized Nanotubes. *Chem. Eur. J.* **2011**, *17*, 6296-6302.

(2) Wong, B. S.; Yoong, S. L.; Jagusiak, A.; Panczyk, T.; Ho, H. K.; Ang, W. H.; Pastorin, G. Carbon Nanotubes for Delivery of Small Molecule Drugs. *Adv. Drug Deliv. Rev.* **2013**, *65*, 1964-2015.

(3) Lvov, Y.; Aerov, A.; Fakhrullin, R. Clay Nanotube Encapsulation for Functional Biocomposites. *Adv. Colloid Interface Sci.* **2014**, *207*, 189-198.

(4) Ray, P. Z.; Shipley, H. J. Inorganic Nano-Adsorbents for the Removal of Heavy Metals and Arsenic: A Review. *RSC Adv.* **2015**, *5*, 29885-29907.

(5) Bong, D. T.; Clark, T. D.; Granja, J. R.; Ghadiri, M. R. Self-Assembling Organic Nanotubes. *Angew. Chem. Int. Ed.* **2001**, *40*, 988-1011.

(6) Barclay, T. G.; Constantopoulos, K.; Matisons, J. Nanotubes Self-Assembled from Amphiphilic Molecules via Helical Intermediates. *Chem. Rev.* **2014**, *114*, 10217-10291.

(7) Shimizu, T.; Kameta, N.; Ding, W.; Masuda, M. Supramolecular Self-Assembly into Biofunctional Soft Nanotubes: From Bilayers to Monolayers. *Langmuir* **2016**, *32*, 12242-12264.

(8) Shimizu, T. Self-Assembly of Discrete Organic Nanotubes. *Bull. Chem. Soc. Jpn.* **2018**, *91*, 623-668.

(9) Baker, L. A.; Jin, P.; Martin, C. R. Biomaterials and Biotechnologies Based on Nanotube Membranes. *Crit.l Rev. Solid State Mater. Sci.* **2005**, *30*, 183-205.

(10) Bohn, P. W. Nanoscale Control and Manipulation of Molecular Transport in Chemical Analysis. *Annu. Rev. Anal. Chem.* **2009**, *2*, 279-296.

(11) Yoshida, K.; Takahashi, R.; Fujii, S.; Kameta, N.; Shimizu, T.; Sakurai, K. Cross-Sectional Structures of a Molecular Monolayer Nanotube Explored with SAXS: Evidence for the Parallel Orientation of the Headgroups in Asymmetric Bolaamphiphiles. *Phys. Chem. Chem. Phys.* **2017**, *19*, 24445-24447.

(12) Wakasugi, A.; Asakawa, M.; Kogiso, M.; Shimizu, T.; Sato, M.; Maitani, Y. Organic Nanotubes for Drug Loading and Cellular Delivery. *Int. J. Pharm.* **2011**, *413*, 271-278.

(13) Kameta, N.; Minamikawa, H.; Masuda, M.; Mizuno, G.; Shimizu, T. Controllable Biomolecule Release from Self-Assembled Organic Nanotubes with Asymmetric Surfaces: pH and Temperature Dependence. *Soft Matter* **2008**, *4*, 1681-1687.

(14) Ding, W.; Kameta, N.; Minamikawa, H.; Wada, M.; Shimizu, T.; Masuda, M. Hybrid Organic Nanotubes with Dual Functionalities Localized on Cylindrical Nanochannels Control the Release of Doxorubicin. *Adv. Healthc. Mater.* **2012**, *1*, 699-706.

(15) Kameta, N.; Lee, S. J.; Masuda, M.; Shimizu, T. Biologically Responsive, Sustainable Release from Metallo-Drug Coordinated 1D Nanostructures. *J. Mater. Chem. B* **2013**, *1*, 276-283.

(16) Moribe, K.; Makishima, T.; Higashi, K.; Liu, N.; Limwikrant, W.; Ding, W.; Masuda, M.; Shimizu, T.; Yamamoto, K. Encapsulation of Poorly Water-Soluble Drugs into Organic Nanotubes for Improving Drug Dissolution. *Int. J. Pharm.* **2014**, *469*, 190-196.

(17) Liu, N.; Higashi, K.; Kikuchi, J.; Ando, S.; Kameta, N.; Ding, W.; Masuda, M.; Shimizu, T.; Ueda, K.; Yamamoto, K.; Moribe, K. Molecular-Level Understanding of the Encapsulation and Dissolution of Poorly Water-Soluble Ibuprofen by Functionalized Organic Nanotubes Using Solid-State NMR Spectroscopy. *J. Phys. Chem. B* **2016**, *120*, 4496-4507.

(18) Kameta, N.; Yoshida, K.; Masuda, M.; Shimizu, T. Supramolecular Nanotube Hydrogels: Remarkable Resistance Effect of Confined Proteins to Denaturants. *Chem. Mater.* **2009**, *21*, 5892-5898.

(19) Kameta, N.; Masuda, M.; Minamikawa, H.; Mishima, Y.; Yamashita, I.; Shimizu, T. Functionalizable Organic Nanochannels Based on Lipid Nanotubes: Encapsulation and Nanofluidic Behavior of Biomacromolecules. *Chem. Mater.* **2007**, *19*, 3553-3560.

(20) Kawauchi, H.; Takahashi, R.; Kameta, N.; Fujii, S.; Lee, J. H.; Shimizu, T.; Sakurai, K. Encapsulation of Albumin in Organic Nanotube Channel: Structural Investigation by Small-Angle X-ray Scattering. *ACS Appl. Bio Mater.*, DOI: 10.1021/acsabm.1029b00047.

(21) Higgins, D. A.; Park, S. C.; Tran-Ba, K.-H.; Ito, T. Single-Molecule Investigations of Morphology and Mass Transport Dynamics in Nanostructured Materials. *Annu. Rev. Anal. Chem.* **2015**, *8*, 193-216.

(22) Coceancigh, H.; Higgins, D. A.; Ito, T. Optical Microscopic Techniques for Synthetic Polymer Characterization. *Anal. Chem.* **2019**, *91*, 405-424.

(23) Kameta, N.; Minamikawa, H.; Someya, Y.; Yui, H.; Masuda, M.; Shimizu, T. Confinement Effect of Organic Nanotubes Toward Green Fluorescent Protein (GFP) Depending on the Inner Diameter Size. *Chem. Eur. J.* **2010**, *16*, 4217-4223.

(24) Okamoto, K.; Shook, C. J.; Bivona, L.; Lee, S. B.; English, D. S. Direct Observation of Wetting and Diffusion in the Hydrophobic Interior of Silica Nanotubes. *Nano Lett.* **2004**, *4*, 233-239.

(25) Guo, L.; Chowdhury, P.; Fang, J.; Gai, F. Heterogeneous and Anomalous Diffusion inside Lipid Tubules. *J. Phys. Chem. B* **2007**, *111*, 14244-14249.

(26) Lu, Q.; Kim, Y.; Bassim, N.; Collins, G. E. Impact of Confinement on Proteins Concentrated in Lithocholic Acid Based Organic Nanotubes. *J. Colloid Interface Sci.* **2015**, *454*, 97-104.

(27) Xu, H.; Nagasaka, S.; Kameta, N.; Masuda, M.; Ito, T.; Higgins, D. A. Imaging Fluorescence Correlation Spectroscopy Studies of Dye Diffusion in Self-Assembled Organic Nanotubes. *Phys. Chem. Chem. Phys.* **2016**, *18*, 16766-16774.

(28) Xu, H.; Nagasaka, S.; Kameta, N.; Masuda, M.; Ito, T.; Higgins, D. A. Spectroscopic Imaging Studies of Nanoscale Polarity and Mass Transport Phenomena in Self-Assembled Organic Nanotubes. *Phys. Chem. Chem. Phys.* **2017**, *19*, 20040-20048.

(29) Bag, N.; Wohland, T. Imaging Fluorescence Fluctuation Spectroscopy: New Tools for Quantitative Bioimaging. *Annu. Rev. Phys. Chem.* **2014**, *65*, 225-248.

(30) Leo, A. J. Calculating Log P_{OCT} from Structures. *Chem. Rev.* **1993**, *93*, 1281-1306.

(31) Tran Ba, K. H.; Everett, T. A.; Ito, T.; Higgins, D. A. Trajectory Angle Determination in One Dimensional Single Molecule Tracking Data by Orthogonal Regression Analysis. *Phys. Chem. Chem. Phys.* **2011**, *13*, 1827-1835.

(32) Kolin, D. L.; Costantino, S.; Wiseman, P. W. Sampling Effects, Noise, and Photobleaching in Temporal Image Correlation Spectroscopy. *Biophys. J.* **2006**, *90*, 628-639.

(33) Elson, E. L.; Magde, D. Fluorescence Correlation Spectroscopy. 1. Conceptual Basis and Theory. *Biopolymers* **1974**, *13*, 1-27.

(34) Ye, F.; Collinson, M. M.; Higgins, D. A. Molecular Orientation and Its Influence on Autocorrelation Amplitudes in Single-Molecule Imaging Experiments. *Anal. Chem.* **2007**, *79*, 6465-6472.

(35) Tcherniak, A.; Reznik, C.; Link, S.; Landes, C. F. Fluorescence Correlation Spectroscopy: Criteria for Analysis in Complex Systems. *Anal. Chem.* **2009**, *81*, 746-754.

(36) Ramette, R. W.; Sandell, E. B. Rhodamine B Equilibria. *J. Am. Chem. Soc.* **1956**, *78*, 4872-4878.

(37) Gendron, P.-O.; Avaltroni, F.; Wilkinson, K. J. Diffusion Coefficients of Several Rhodamine Derivatives as Determined by Pulsed Field Gradient-Nuclear Magnetic Resonance and Fluorescence Correlation Spectroscopy. *J. Fluores.* **2008**, *18*, 1093-1101.

(38) Deen, W. M. Hindered Transport of Large Molecules in Liquid-Filled Pores. *AIChE J.* **1987**, *33*, 1409-1425.

(39) Conlisk, A. T.: Modeling Biomolecular Transport at the Nanoscale. In *BioMEMS and Biomedical Nanotechnology*; Ferrari, M., Ed.; Springer: New York, 2006; Vol. 1; pp 399-434.

(40) Ray, K.; Nakahara, H. Adsorption of Sulforhodamine Dyes in Cationic Langmuir-Blodgett Films: Spectroscopic and Structural Studies. *J. Phys. Chem. B* **2002**, *106*, 92-100.

(41) Chechik, V.; Crooks, R. M.; Stirling, C. J. M. Reactions and Reactivity in Self-Assembled Monolayers. *Adv. Mater.* **2000**, *12*, 1161-1171.

(42) Holmlin, R. E.; Chen, X.; Chapman, R. G.; Takayama, S.; Whitesides, G. M. Zwitterionic SAMs that Resist Nonspecific Adsorption of Protein from Aqueous Buffer. *Langmuir* **2001**, *17*, 2841-2850.

(43) Schlenoff, J. B. Zwitteration: Coating Surfaces with Zwitterionic Functionality to Reduce Nonspecific Adsorption. *Langmuir* **2014**, *30*, 9625-9636.

Chapter 6 - Effect of Surface Charge and Inner Diameter on the Diffusion Behavior of Ionic and Zwitterionic Molecules in Self-Assembled Organic Nanotubes

G. Ghimire, M.M. Moore, R. Leuschen, S. Nagasaka, N. Kameta, M. Masuda, D.A. Higgins, T. Ito, manuscript in preparation.

Contribution of Authors

This is an extension of **Chapter 5**. DAH and TI designed the experiments. NK and MM synthesized the bolaamphiphiles and the characterized bolaamphiphile-based ONTs using TEM. SN prepared the dispersed ONT sample on coverslips. GG and MM collected and analyzed most of the imaging FCS data, whereas RL collected a part of the data at the early stage of the experiments.

6.1 Introduction

Self-assembled organic nanotubes (ONTs) derived from asymmetric bolaamphiphiles have distinct functional advantages over other symmetrical counterparts, owing to their tunable inner diameters and surface functionalization for biocompatibility, secure encapsulation, selective target recognition and controlled molecular cargo delivery.[1-5] These unique properties arise from the capability of asymmetric bolaamphiphiles for parallelly packed head-to-tail polytype self-assembly.[6,7] The resulting ONTs have cylindrical tubular structures with an homogenous inner diameter of 2 – 100 nm, which can be adjusted by controlling spacer lengths, terminal head-group size and their arrangement in the rolled layer(s) as discussed in **Chapter 1.2.2**.[1] X-ray

diffraction (XRD) results suggest that the inner diameters of these ONTs depend upon molecular packing within the monolayer lipid membrane (MLM). Asymmetrical ONTs are very suitable for selective functionalization of inner and outer surfaces with anionic, cationic, neutral or hydrophobic groups.[4,8,9] The surface functionalization can be categorized to postmodification and prefunctionalization. Postmodification refers to the modification of the ONT surface after successful self-assembly. For example, amine-terminated asymmetrical ONTs were covalently modified with a fluorescent moiety, 4-fluoro-7nitrobenzofuran. In prefunctionalization, a functional group of interest is conjugated with ONT-forming precursors prior to the formation of ONTs.[10] Selective functionalization of the inner surface of ONTs will enhance interactions with encapsulated molecules and thus promote their secure encapsulation, and that of the outer surface will improve the selectivity and efficiency of ONT delivery.

Molecular encapsulation and release with ONTs are affected by several factors like the concentration, distribution, size and chemical properties of encapsulated species as well as the length, inner diameter and surface chemical properties of ONTs. Guo et al. reported the effects of concentration and position of encapsulated molecules on their diffusion behavior inside lipid-based ONTs.[11] Meliander et al. reported the facilitated encapsulation and release of protein molecules with lower molecular weights with lipid-based ONTs.[12] Ding et al. showed that ONTs with lengths of 400 – 800 nm could easily reach to a target cell and deliver loaded plasmid DNA while ONTs longer than 1 μm struggled.[13] More relevantly, Kameta et al. extensively studied the behavior of molecular encapsulation and release with asymmetrical ONTs of different inner diameters using TEM and spectroscopic methods.[3-5,10,14] They investigated the encapsulation of different kinds of species ranging from biomacromolecules to small dye molecules, and found that the rational control of the inner diameter and surface functionalities was essentially required.

For example, they investigated the effects of inner diameter on the encapsulation of DNA using 20- and 80-nm diameters ONTs formed from *N*-(2-amino-ethyl)-*N*'-(*β*-D-glucopyranosyl)-alkanediamide.[10] They showed that the YOYO-1-labelled T4GT7-DNA, which is 56 μm in extended length, 2 nm in width and 50 nm in persistence length, could be encapsulated only in the 80-nm ONTs. They also demonstrated the electrostatic, pH-controlled encapsulation of anionic ferritin and cationic starvation-induced DNA-binding protein (Dps) in ONTs with inner amine and carboxyl groups.[10]

Kameta et al. also assessed the diffusion of ferritin and green fluorescent protein (GFP) within ONTs with different inner diameters.[15] The inner amine groups of asymmetric ONTs with inner diameters of 10, 20 and 80 nm were covalently modified with Alexa Fluor 546 to trigger fluorescence resonance energy transfer (FRET) with GFP in close proximity to the nanotube inner surface. Analyses of time-lapse fluorescence microscopy images showed a clear decrease in diffusion coefficient (*D*) for both GFP and ferritin with decreasing inner diameters, because of the restricted nanospace. *D* was obtained by plotting the square of diffusion distance (X^2) that was measured from the FRET-induced quenching of Alexa Fluor 546 fluorescence as a function of time (**Chapter 1.2.4**). They further studied protein refolding within hydrogels of asymmetric ONT with different inner diameter and surface properties.[16] Hydrogels based on 10-nm diameter ONTs gave first and second GFP refolding ratio of 49% with further enhancement to 85% upon partial introduction of hydrophobic moiety. In contrast, GFP refolding was absent in hydrogels of 20-nm diameter ONTs. These observations suggest that the GFP refolding could be assisted by the nanospace of the ONTs.

Although there are several reports that claim the effects of ONT inner diameter and surface properties on molecular encapsulation, diffusion or biochemical function, these studies were

either limited to investigations for macromolecules or to ensemble measurements from multiple ONTs. A thorough and systematic study of the local diffusion of small molecules in individual ONTs with different inner diameter and surface properties is crucial to develop ONTs suitable for various applications. **Chapter 5** described the diffusion behavior of anionic sulforhodamine B (SRB), zwitterionic/cationic rhodamine B (RB) and cationic rhodamine 123 (R123) within amine-terminated asymmetrical ONTs of diameter 10 nm (NH_2-ONT_{10nm}). Electrostatic interactions with the ONT inner surface played an important role in molecular diffusion behavior. Anionic SRB ($pK_a < 1$) exhibited a decrease in D at lower pH conditions (8.4 – 4.4) due to the enhancement of electrostatic attraction induced by the protonation of the inner amine groups ($pK_a \sim 7.28$).[17,18] In contrast, cationic RB ($pK_a \sim 3.2$) and R123 ($pK_a > 8.7$) showed an increase in D with decreasing pH due to the protonation-induced enhancement of electrostatic repulsion. The molecular diffusion would take place near the ONT surface, as suggested by the two-color imaging FCS results with solvatochromic Nile red and hydroxylated Nile red.[19] In this chapter, diffusion of SRB, RB and R123 within carboxyl-terminated asymmetrical ONTs with inner diameters of 10 and 20 nm (COOH-ONT_{10nm} and COOH-ONT_{20nm}) was measured in pH 6.4 ~ 8.4 solutions having different ionic strengths using imaging FCS. Results with these ONTs were subsequently compared with those with NH_2-ONT_{10nm} (**Chapter 5**). Imaging FCS was used because of its capability to probe local diffusion behavior at sub-μm-scale detection regions of an entire ONT. Other methods used for the measurements of D, including FRET, fluorescence recovery after photobleaching (FRAP) and fluorescence correlation spectroscopy (FCS), are not suitable for simultaneous assessment of local permeability of intact ONTs with relatively short lengths (≤ 10 μm).[10,14,20-23]

6.2 Experimental Section

6.2.1 Chemicals and Materials

Bolaamphiphiles that form COOH-ONTs$_{10nm}$ and COOH-ONTs$_{20nm}$ with terminal carboxyl and glucose head groups (**Figures 6.1a** and **b**) were synthesized according to a procedure reported previously.[4,8] TEM images of NH_2-ONTs$_{10nm}$, COOH-ONT$_{10nm}$ and COOH-ONT$_{20nm}$ are given in **Figure 6.2**.[5,8,18] Sulforhodamine B (SRB; Acros Organics), rhodamine B (RB; Aldrich), rhodamine-123 (R123; Aldrich), phosphate buffered saline (P5368; Aldrich), which yields one liter of 0.01 M phosphate buffered saline containing 0.138 M NaCl and 0.0027 M KCl, hydrochloric acid (HCl; Fisher), sodium hydroxide (NaOH; Fisher) and *o*-phosphoric acid (Fisher Scientific) were used as received. All aqueous solutions were prepared with water having a resistivity of 18 MΩ cm or higher (Barnstead Nanopure Systems).

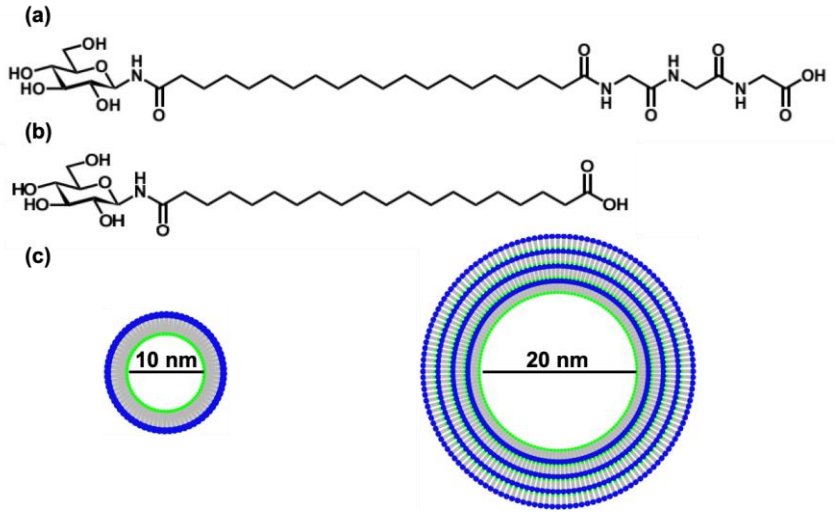

Figure 6.1 Molecular structures of bolaamphiphiles used to obtain **(a)** COOH-ONT$_{10nm}$ and **(b)** COOH-ONT$_{20nm}$. (c) Schematic illustrations of the cross-sectional views of COOH-ONT$_{10nm}$ and COOH-ONT$_{20nm}$.

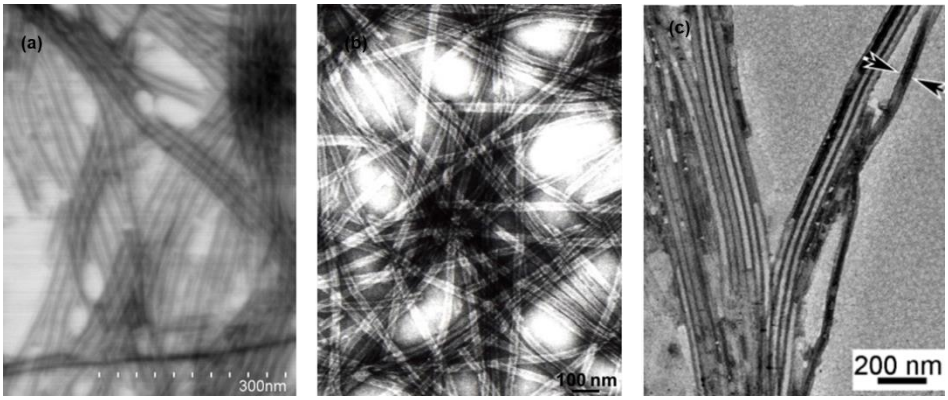

Figure 6.2 (a) Scanning-TEM images of NH_2-ONT_{10nm}, and TEM images of **(b)** COOH-ONT_{10nm}, and **(c)** COOH-ONT_{20nm}. The figures were reproduced with permission from references 5, 8, and 18 for **(a)**, **(b)**, and **(c)** respectively. **(a)** 2019, Copyright: American Chemical Society, **(b)** 2012, Copyright: Royal Society of Chemistry, and **(c)** 2004, Copyright: American Chemical Society.

6.2.2 Sample Preparation for Imaging FCS Experiments

COOH-ONT_{10nm} and COOH-ONT_{20nm} were prepared from the precursor bolaamphiphiles according to a procedure reported previously.[4]The bolaamphiphile was dissolved in DMSO at 70 °C, and then cooled to room temperature to obtain a DMSO gel. The gel was transferred into deionized water, dispersed, and then the resulting solution was filtrated to collect ONTs. ONTs were then deposited onto plasma-cleaned glass coverslips from a turbid aqueous solution, and dried. An aqueous dye solution (500 nM, 200 μL) was deposited onto the coverslips for 2-24 hours to ensure sufficient loading of the dye, washed with ultra-pure water, and then dried by N_2 blowing. Acquisition of wide-field fluorescence images and their analysis were carried out in a procedure described in **Chapter 5.2.4**.[18] LabView software gave a D_{local}/σ^2 value from each pixel along an ONT, which was further analyzed using imageJ to obtain D_{local} and D_{ONTs}.

6.3 Result and Discussion

6.3.1 COOH-ONTs and Fluorescent Molecules

This chapter focuses on describing the diffusion of three differently charged fluorescent molecules *viz.* anionic SRB, zwitterionic/cationic RB and cationic R123 within COOH-ONT$_{10nm}$ and COOH-ONT$_{20nm}$. The three dye molecules have different pK_a and log P_{oct} in aqueous solution as summarized in **Table 5.1**.[18]

COOH-ONT$_{10nm}$ and COOH-ONT$_{20nm}$ have glucose and carboxyl groups on their exterior and interior surfaces. The inner carboxyl groups of the ONTs were verified by FT-IR while their pK_a (~ 6.0) was measured using pH titration.[3,5,8] The inner diameters of the ONTs were previously measured using TEM (**Figure 6.2**).[5,8,18] The TEM images suggest that COOH-ONT$_{10nm}$ consists of a single monolayer like NH_2-ONTs$_{10nm}$ with a wall thickness of 3-4 nm, whereas COOH-ONT$_{20nm}$ is based on four layers with a wall thickness of 12.2 nm. The molecular packing of the wall of COOH-ONT$_{20nm}$ may not be perfect due to the absence of polyglycine-II-type hydrogen bonding, in contrast to COOH-ONT$_{10nm}$ with three glycine moieties, possibly allowing molecular permeation through the nanotube wall.

6.3.2 Imaging FCS Data Analysis

Fluorescence videos of 25000 frames were collected for each selected ONT with exposure time (frame time) of 0.002 sec and cycle time (time between each frames) of 0.0065 sec at the laser power of ≈ 0.01 mW. The video data was then loaded to the LabView built software for the truncation of the initial 5000 frames, background correction, autocorrelation and theoretical fitting to obtain D_{local}. Autocorrelation of the time trace was done for each pixel using the **Equation 2.9**. The resulting autocorrelation function was fitted with one-dimensional Fickian diffusion model described by **Equation 2.10**, considering the high aspect ratio of the ONTs, i.e., the length of 1-5 μm and the inner diameter of 10 or 20 nm. It should be noted that τ_{max} of 320

frames was used for the fitting because empirically, the largest *D* was obtained around this time lag due to the limited signal averaging at the longer τ_{max}.

Representative images of COOH-ONT_{10nm} and COOH-ONT_{20nm} as collected from the wide-field microscope, after background subtraction and after autocorrelation are shown in **Figures 6.3** and **6.4**, respectively. The images after autocorrelation show that the ONTs could be visualized at sub-diffraction limited resolution. For example, SRB-doped COOH-ONT_{10nm} is barely recognized in raw images from the microscope (**Figure 6.3a**) but is distinctly clear after background subtraction and autocorrelation (**Figure 6.3c**). In addition, these images show the variation of ONT length: **Figure 6.3b** shows a 2 μm-long COOH-ONT_{10nm} and **Figure 6.4b** shows ≥ 5 μm-long COOH-ONT_{20nm}. Furthermore, fluorescence intensity was different among individual ONTs and also varied from pixel to pixel, possibly reflecting different loading concentration of the dye. Empirically, COOH-ONT_{20nm} could be doped more easily, and usually gave fluorescence images of higher S/N, than COOH-ONT_{10nm}.

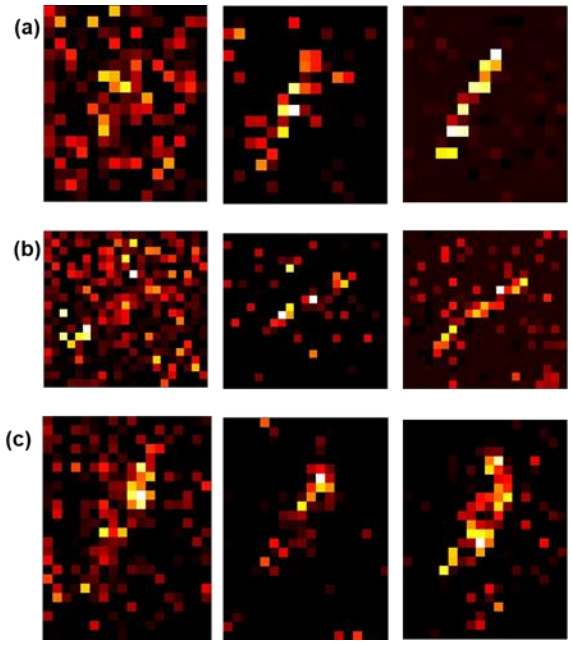

Figure 6.3 Representative images of COOH-ONT$_{10nm}$ doped by **(a)** SRB, **(b)** RB, and **(c)** R123: Left: raw fluorescence image; Middle: image after background subtraction; Right: autocorrelation amplitude image.

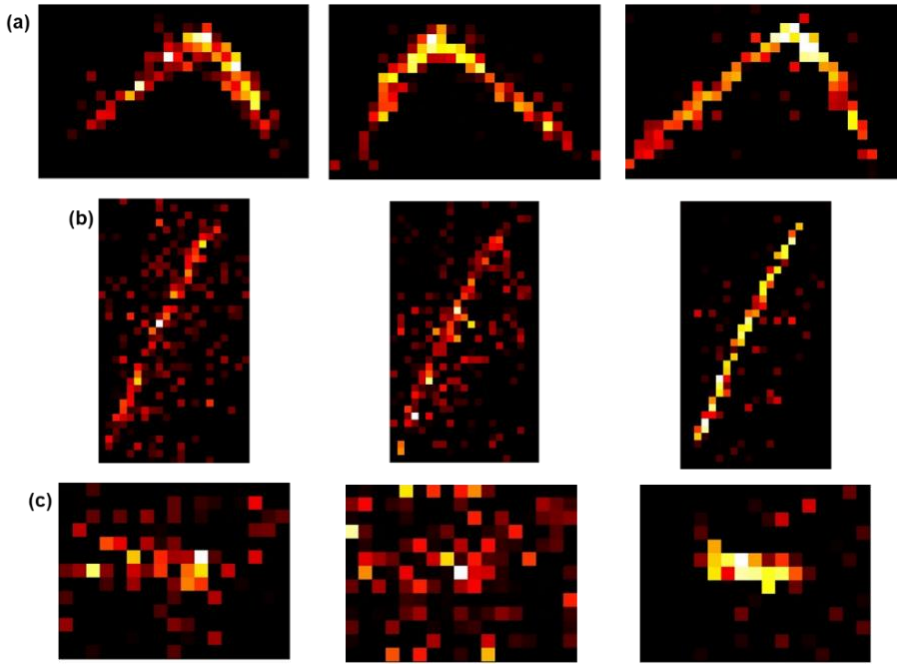

Figure 6.4 Representative images of COOH-ONT$_{20nm}$ doped by **(a)** SRB, **(b)** RB, and **(c)** R123: Left: raw fluorescence image; Middle: image after background subtraction; Right: autocorrelation amplitude image.

6.3.3 Effect of ONT Length on D_{ONT}

It was reported that filamentous nanostructures as found with asymmetric ONTs could be beneficial for drug delivery applications due to their sustained retention in blood.[24-26] Furthermore, such nanostructures are suitable for such applications because they can gradually release molecules from the two open ends. The release rate of encapsulated molecules is controlled by molecular diffusion along the nanostructures, and thus it is important to quantify local diffusion behavior in such structure. In **Chapter 5**, we showed that D_{ONT} was independent of the length of NH_2-ONT_{10nm} in the range of 1 – 5 μm.[18] In this chapter, the effects of ONT length on D_{ONT} was investigated for COOH-ONT_{10nm} and COOH-ONT_{20nm}. **Figures 6.5** and **6.6** show that, as with NH_2-ONT_{10nm}, D_{ONT} negligibly depends on the length of COOH-ONT_{10nm} and COOH-ONT_{20nm}, leading to homogeneous encapsulation and release for the batch of the ONTs.

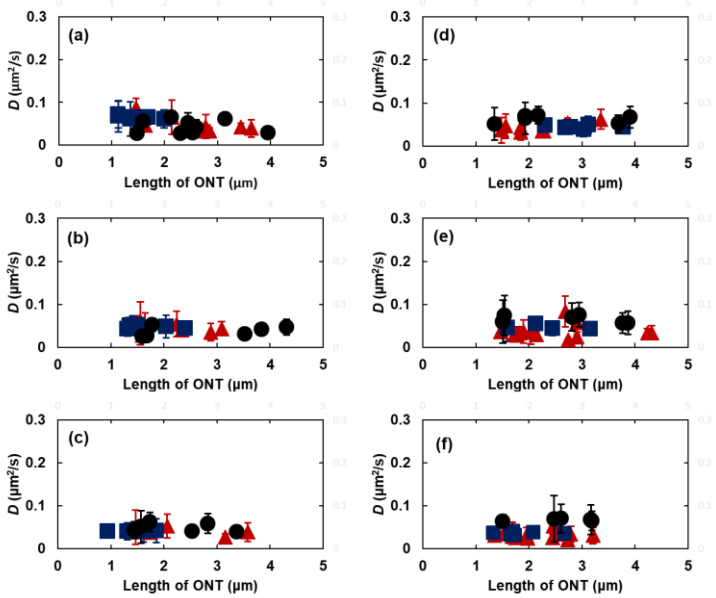

Figure 6.5 Relationship between the length of COOH-ONT_{10nm} and D_{ONT} for SRB (black spheres), RB (red triangles) and R123 (blue squares). D_{ONT} was measured in PBS solutions at pH **(a)** 3.4 **(b)** 4.4 **(c)** 5.4 **(d)** 6.4 **(e)** 7.4 and **(f)** 8.4 with the ionic strength of 160 mM. Error bars indicate 95% confidence interval from D_{local} values obtained at ~10 pixels along each ONT. Several data were collected and analyzed by Mikaela Moore and Rebecca Leuschen.

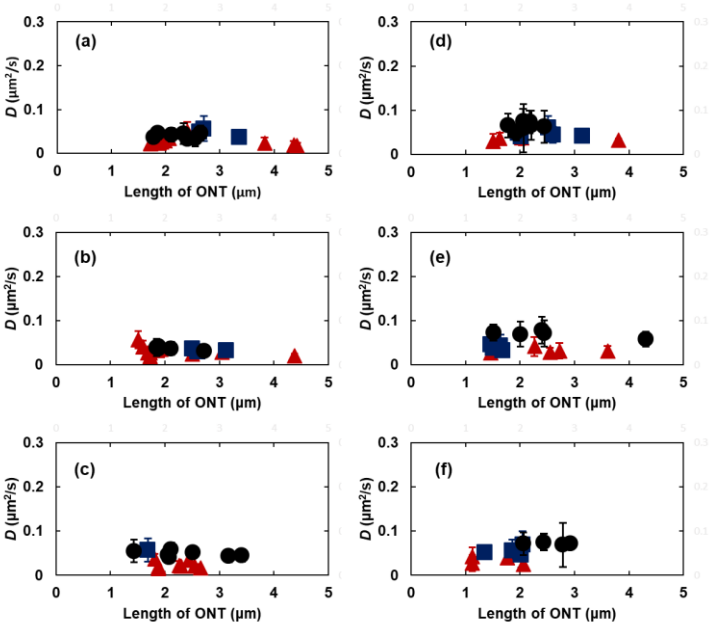

Figure 6.6 Relationship between the length of COOH-ONT$_{20nm}$ and D_{ONT} for SRB (black spheres), RB (red triangles) and R123 (blue squares). D_{ONT} was measured in PBS solutions at pH **(a)** 3.4 **(b)** 4.4 **(c)** 5.4 **(d)** 6.4 **(e)** 7.4 and **(f)** 8.4 with the ionic strength of 160 mM. Error bars indicate 95% confidence interval from D_{local} values obtained at ~10 pixels along each ONT. Several data were collected and analyzed by Mikaela Moore and Rebecca Leuschen

6.3.4 Effects of Inner Diameter

The effects of ONT inner diameter on molecular diffusion can be discussed from the *D* data for COOH-ONT$_{10nm}$ and COOH-ONT$_{20nm}$. **Figures 6.5** and **6.6** suggest that there was not so significant difference in pH-dependent D_{ONT} for each of the dyes within these ONTs. **Figure 6.7** summarized the *D* values of the three dyes for COOH-ONT$_{10nm}$ and COOH-ONT$_{20nm}$, which were obtained from the data shown in **Figures 6.5** and **6.6**. There is no clear difference in *D* for these ONTs, except the observation of slightly smaller *D* values for RB in COOH-ONT$_{20nm}$ at acidic pH conditions. The comparable *D* values suggest negligible difference in electrostatic interactions with small molecules within 10 and 20 nm nanotubes. In contrast, Kameta et al. reported the diffusion of fluorescently-labeled amino acids within 4-nm diameter ONTs was

more strongly affected by electrostatic or hydrogen bonding interactions than that within 8-nm diameter ONTs.[16]

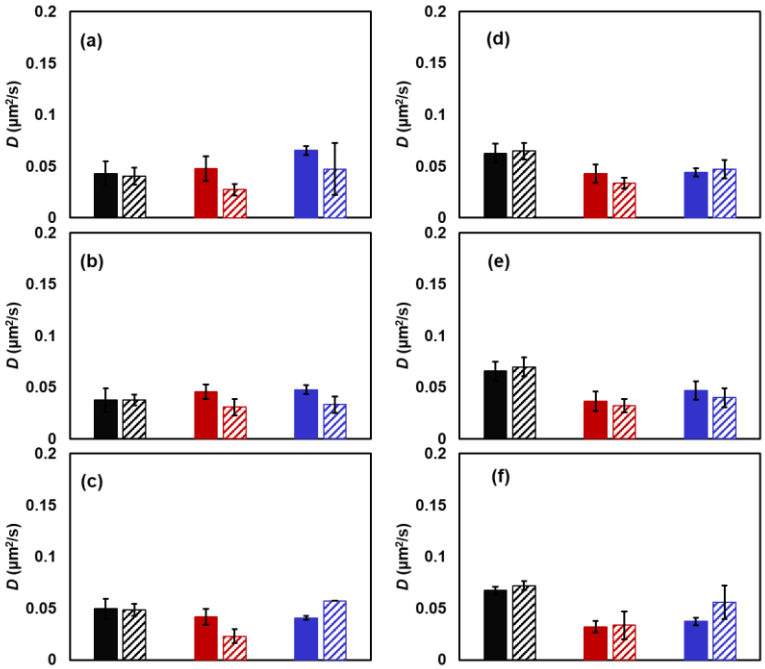

Figure 6.7 *D* values obtained with the ONTs (solid-bars: COOH-ONT$_{10nm}$, striped-bars: COOH-ONT$_{20nm}$) for SRB (black), RB (red), and R123 (blue) in 160 mM PBS solutions of **(a)** pH 3.4 **(b)** pH 4.4 **(c)** pH 5.4 **(d)** pH 6.4 **(e)** pH 7.4 and **(f)** pH 8.4. Error bars indicate 95% confidence interval calculated from D_{ONT} values obtained from 4 - 15 ONTs.

6.3.5 Effects of Surface Charge

As described in **Chapter 5**, the *D* values of the three dye molecules in NH_2-ONT$_{10nm}$ were strongly affected by solution pH on the basis of electrostatic interactions controlled by the protonation of the inner amine groups: Attractive interactions reduced *D* due to the adsorption of the molecules onto the ONT walls while repulsive interactions increased *D*. Here, the data in **Figure 6.7**, together with data at 160 mM ionic strength in **Figure 5.9**, were replotted in **Figure 6.8** to discuss the effects of pH on *D* for the three dye molecules.

For anionic SRB (**Figure 6.8a**), all the ONTs showed very similar pH-dependent changes in *D*, which would be basically regulated by electrostatic interactions. The decrease in *D* at the lower pH could be explained by the reduction of electrostatic repulsion dye to the protonation of the inner carboxyl groups of COOH-ONT_{10nm} and COOH-ONT_{20nm}. At higher pH, amine- and carboxyl-terminated ONTs undergo less attractive and more repulsive interactions with SRB, respectively, resulting in increase in *D*.

Figure 6.8b shows the effect of pH on *D* for zwitterionic/cationic RB. In contrast to NH_2-ONT_{10nm}, COOH-ONT_{10nm} and COOH-ONT_{20nm} exhibited negligible pH-dependent change in *D*. This observation can be explained as follows: At the lower pH, the carboxyl groups of RB and ONT surface are protonated to give cationic RB and uncharged ONT surface, resulting in negligible electrostatic interactions. At the higher pH, the deprotonation of carboxyl groups afford uncharged, zwitterionic RB and anionic ONT surface, again resulting in in negligible electrostatic interactions. In contrast, NH_2-ONT_{10nm} exhibited the higher *D* at the lower pH due to repulsive interactions between the cationic RB and positively-charged ONT inner surface.

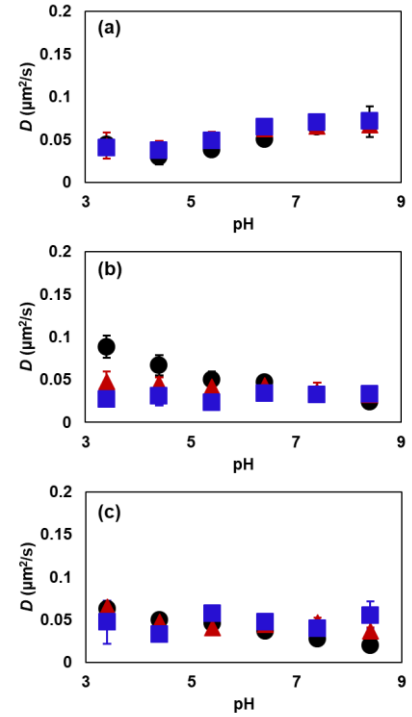

Figure 6.8 Plots showing the effect of pH on *D* of **(a)** SRB, **(b)** RB, and **(c)** R123 for NH_2-ONT_{10nm} (black spheres), COOH-ONT_{10nm} (red triangles), and COOH-ONT_{20nm} (blue squares). Errors indicated 95% confidence interval obtained from D_{ONT} values from 4-15 ONTs.

Cationic R123 showed higher *D* at acidic pH for COOH-ONT_{10nm} (**Figure 6.8c**). At basic pH, pH effect on *D* was negligible. In contrast, NH_2-ONT_{10nm} exhibited an increase in *D* with decreasing pH over the entire pH range, which was rationalized by electrostatic repulsion due to the protonation of the inner amine groups. Of note, at this point, results for COOH-ONT_{20nm} could not be discussed due to the limited number of data.

The surface charge effects were further assessed by measuring *D* in pH 7.4 PBS solutions at different ionic strengths. An increase in the PBS concentration from 1.60 to 500 mM leads to a decrease in the Debye length from 7.6 to 0.43 nm, leading to the stronger screening of the electrostatic interactions. As a result, both electrostatic attraction and repulsion are expected to mitigate at the higher ionic strength and thus to observe larger and smaller *D*. However,

experimental results were somewhat different. For SRB, both COOH-ONT$_{10nm}$ and COOH-ONT$_{20nm}$ gave the highest *D* at 160 mM and similar *D* at the other ionic strengths (**Figure 6.9a**). For RB, ionic strength effect was negligible (**Figure 6.9b**), as anticipated from the negligible involvement of electrostatic interactions with the ONT surface (*vide supra*). Cationic R123 on the other hand shows somewhat larger *D* for COOH-ONT$_{10nm}$ at 160 and 500 mM (**Figure 6.9c**), attributable to the screening of the electrostatic attraction with the ONT surface. Again, the results for COOH-ONT$_{20nm}$ cannot be discussed in this chapter due to the limited number of data.

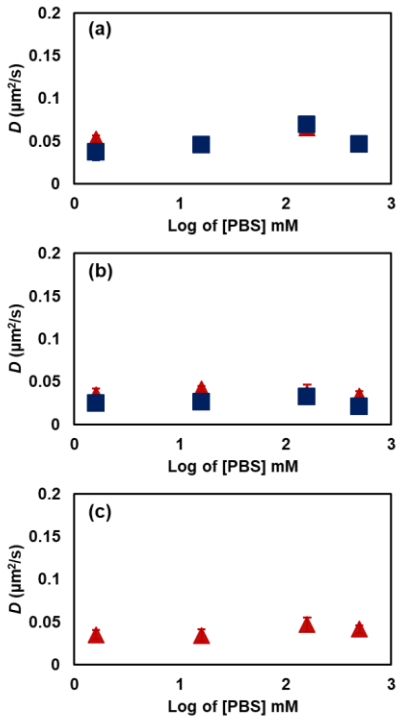

Figure 6.9 Plots showing the effect of ionic strength (1.60, 16.0, 160 and 520 mM) on *D* of **(a)** SRB, **(b)** RB, and **(c)** R123 for NH$_2$-ONT$_{10nm}$ (black spheres), COOH-ONT$_{10nm}$ (red triangles), and COOH-ONT$_{20nm}$ (blue squares). Errors indicate 95% confidence interval obtained from D_{ONT} values from 4-15 ONTs.

6.4 Conclusions

In this chapter, the diffusion behavior of three differently charged dyes was discussed within three types of ONTs having different surface functional groups and inner diameters () in

pH 3.4 – 8.4 solutions of different ionic strengths (1.6, 16, 160 and 500 mM). ONT length did not affect diffusion behavior of any of the dye molecules for the three ONTs, indicating the homogeneity of the properties of ONTs in the batch. COOH-ONT_{10nm} and COOH-ONT_{20nm} exhibited similar diffusion behavior except RB molecules at acidic pH. Most importantly, electrostatic interactions played the most significant role in molecular diffusion also in these COOH-terminated ONTs. Attractive interactions hindered the diffusion of molecules due to their adsorption onto the ONT inner surface, while repulsive interactions enhanced the diffusion. The negligible effect of ionic strength might be due to involvement of hydrophobic and hydrogen bonding interactions in molecular diffusion in these ONTs. These findings may help design ONTs with appropriate surface properties and inner diameter for drug-delivery applications in the future.

6.5 References

(1) Kameta, N., Minamikawa, H. and Masuda, M., 2011. Supramolecular organic nanotubes: how to utilize the inner nanospace and the outer space. *Soft Matter, 7*(10), pp.4539-4561.

(2) Wakasugi, A., Asakawa, M., Kogiso, M., Shimizu, T., Sato, M. and Maitani, Y., 2011. Organic nanotubes for drug loading and cellular delivery. *International journal of pharmaceutics, 413*(1-2), pp.271-278.

(3) Kameta, N.; Minamikawa, H.; Masuda, M.; Mizuno, G.; Shimizu, T. Controllable Biomolecule Release from Self-Assembled Organic Nanotubes with Asymmetric Surfaces: pH and Temperature Dependence. *Soft Matter* **2008**, *4*, 1681-1687.

(4) Ding, W.; Kameta, N.; Minamikawa, H.; Wada, M.; Shimizu, T.; Masuda, M. Hybrid Organic Nanotubes with Dual Functionalities Localized on Cylindrical Nanochannels Control the Release of Doxorubicin. *Adv. Healthc. Mater.* **2012**, *1*, 699-706.

(5) Kameta, N.; Lee, S. J.; Masuda, M.; Shimizu, T. Biologically Responsive, Sustainable Release from Metallo-Drug Coordinated 1D Nanostructures. *J. Mater. Chem. B* **2013**, *1*, 276-283.

(6) Shimizu, T.; Kameta, N.; Ding, W.; Masuda, M. Supramolecular Self-Assembly into Biofunctional Soft Nanotubes: From Bilayers to Monolayers. *Langmuir* 2016, 32, 12242-12264.

(7) Shimizu, T.; Minamikawa, H.; Kogiso, M.; Aoyagi, M.; Kameta, N.; Ding, W. X.; Masuda, M. Self-Organized Nanotube Materials and Their Application in Bioengineering. Polym. J. 2014, 46, 831-858.

(8) Masuda, M.; Shimizu, T. Lipid Nanotubes and Microtubes: Experimental Evidence for Unsymmetrical Monolayer Membrane Formation from Unsymmetrical Bolaamphiphiles. *Langmuir*. **2004**, *20*, 5969-5977.

(9) Kameta, N.; Masuda, M.; Minamikawa, H.; Goutev, N. V.; Rim, J. A.; Jung, J. H.; Shimizu, T. Selective Construction of Supramolecular Nanotube Hosts with Cationic Inner Surfaces. *Adv. Mater*. **2005**, *17*, 2732-2736.

(10) Kameta, N.; Masuda, M.; Minamikawa, H.; Mishima, Y.; Yamashita, I.; Shimizu, T. Functionalizable Organic Nanochannels Based on Lipid Nanotubes: Encapsulation and Nanofluidic Behavior of Biomacromolecules. *Chem. Mater.* **2007**, *19*, 3553-3560.

(11) Guo, L.; Chowdhury, P.; Fang, J.; Gai, F. Heterogeneous and Anomalous Diffusion inside Lipid Tubules. *J. Phys. Chem. B* **2007**, *111*, 14244-14249.

(12) Meilander, N.J.; Yu, X.; Ziats, N.P.; Bellamkonda, R.V. Lipid-based microtubular drug delivery vehicles. *Journal of Controlled Release*. **2001**, *71*, pp.141-152.

(13) Ding, W.; Wada, M.; Kameta, N.; Minamikawa, H.; Shimizu, T.; Masuda, M. Functionalized organic nanotubes as tubular nonviral gene transfer vector. *Journal of controlled release*. **2011**, *156*, 70-75.

(14) Liu, N.; Higashi, K.; Kikuchi, J.; Ando, S.; Kameta, N.; Ding, W.; Masuda, M.; Shimizu, T.; Ueda, K.; Yamamoto, K.; Moribe, K. Molecular-Level Understanding of the Encapsulation and Dissolution of Poorly Water-Soluble Ibuprofen by Functionalized Organic Nanotubes Using Solid-State NMR Spectroscopy. *J. Phys. Chem. B* **2016**, *120*, 4496-4507.

(15) Kameta, N.; Minamikawa, H.; Someya, Y.; Yui, H.; Masuda, M; Shimizu, T. Confinement effect of organic nanotubes toward green fluorescent protein (GFP) depending on the inner diameter size. *Chem. Eur. J*. **2010**, 16, 4217–4223.

(16) Kameta, N.; Masuda, M.; Shimizu, T. Soft nanotube hydrogels functioning as artificial chaperones. *ACS nano*. **2012**, *6*, 5249-5258.

(17) Xu, H.; Nagasaka, S.; Kameta, N.; Masuda, M.; Ito, T.; Higgins, D. A. Imaging Fluorescence Correlation Spectroscopy Studies of Dye Diffusion in Self-Assembled Organic Nanotubes. *Phys. Chem. Chem. Phys.* **2016**, *18*, 16766-16774.

(18) Ghimire, G.; Espinoza, R.; Xu, H.; Nagasaka, S.; Kameta, N.; Masuda, M.; Higgins, D. A.; Ito, T. Diffusion Behavior of Differently Charged Molecules in Self-Assembled Organic Nanotubes Studied Using Imaging Fluorescence Correlation Spectroscopy. *Langmuir*. **2019,** *35*, 7783-7790.

(19) Xu, H.; Nagasaka, S.; Kameta, N.; Masuda, M.; Ito, T.; Higgins, D. A. Spectroscopic Imaging Studies of Nanoscale Polarity and Mass Transport Phenomena in Self-Assembled Organic Nanotubes. *Phys. Chem. Chem. Phys.* **2017**, *19*, 20040-20048.

(20) Higgins, D. A.; Park, S. C.; Tran-Ba, K.-H.; Ito, T. Single-Molecule Investigations of Morphology and Mass Transport Dynamics in Nanostructured Materials. *Annu. Rev. Anal. Chem.* **2015**, *8*, 193-216.

(21) Coceancigh, H.; Higgins, D. A.; Ito, T. Optical Microscopic Techniques for Synthetic Polymer Characterization. *Anal. Chem.* **2019**, *91*, 405-424.

(22) Okamoto, K.; Shook, C. J.; Bivona, L.; Lee, S. B.; English, D. S. Direct Observation of Wetting and Diffusion in the Hydrophobic Interior of Silica Nanotubes. *Nano Lett.* **2004**, *4*, 233-239.

(23) Lu, Q.; Kim, Y.; Bassim, N.; Collins, G. E. Impact of Confinement on Proteins Concentrated in Lithocholic Acid Based Organic Nanotubes. *J. Colloid Interface Sci.* **2015**, *454*, 97-104.

(24) D. Pantarotto , R. Singh , D. McCarthy , M. Erhard , J. P. Briand , M. Prato , K. Kostarelos , A. Bianco , *Angew. Chem. Int. Ed.* **2004**, *43*, 5242.

(25) Z. Liu , A. C. Fan , K. Rakhra , S. Sherlock , A. Goodwin , X. Chen , Q. Yang , D. W. Felsher , H. Dai , *Angew. Chem. Int. Ed.* **2009**, *48*, 7668 .

(26) Y. Geng, P. Dalhaimer, S. Cai, R. Tsai, M. Tewari, T. Minko, D.E. Discher, Shape effects of filaments versus spherical particles in flow and drug delivery, Nat. Nanotechnol. 2 (2007) 249–255.

Chapter 7 - General Conclusions and Future Outlook

In this dissertation, we investigated charge transport within self-assembled nanostructures in thin-films of redox block copolymers (BCP) and molecular diffusion in asymmetric ONTs. In-depth understanding of charge transport behavior in redox BCP microdomains of different morphologies is very crucial for their potential applications as catalysts or sensors. Spectroscopic ellipsometry, AFM and electrochemical methods were used to measure the film thickness, microdomain morphologies and charge transport efficiency. Likewise, in-depth knowledge of diffusion behavior of small molecules inside ONTs having different surface functional groups and inner diameters at near-physiological pH and ionic strength conditions is required to utilize them for drug-delivery applications. Imaging FCS provided a very convenient tool to study molecular diffusion within the very small regions of a single ONT.

In **Chapter 3**, we successfully assessed the electrochemical properties of PS-*b*-PAEFc thin-films in 0.1 M $TBAPF_6$/acetonitrile. We showed that electron hopping assisted by counterion migration was the charge transport mechanism within the thin PS_{154}-*b*-$PAEFc_{26}$ and PS_{154}-*b*-$PAEFc_{51}$ films with possible lamellar and cylindrical microdomains, respectively. Because of the higher electrochemical stability as a result of scaffold forming redox-inert PS matrix, thin films comprising cylindrical microdomains were considered to be promising candidates for electrochemical applications. PS_{154}-*b*-$PAEFc_{12}$ showed thickness-independent, adsorption-controlled charge transport behavior due to the formation of spherical microdomains that were buried within PS matrix. Most importantly, we found that D_{ap} was independent of microdomain morphology or film thickness, reflecting comparable concentration, electron transfer properties and dynamic properties of the redox moieties within the microdomains.

In **Chapter 4**, we studied the electrochemical properties of the same PS-*b*-PAEFc thin-films on gold electrodes in 0.1 M $NaPF_6$/ethanol. We showed that a pristine PS-*b*-PAEFc film was redox-inactive in $NaPF_6$/ethanol but rendered redox-active once its redox moieties were electrochemically oxidized in $TBAPF_6$/acetonitrile possibly due to the incorporation of counter ions into the film. Although the fraction of redox active ferrocene moieties in $TBAPF_6$/acetonitrile and $NaPF_6$/ethanol were comparable, charge transport efficiency represented by D_{ap} was significantly lower for the latter. The low charge transport efficiency may reflect the restricted mobility of the redox moieties and limited counterion migration in the less swollen films. AFM images showed that microdomain morphologies on the thin films were retained even after a series of electrochemical measurements. Most interestingly, $TBAPF_6$/acetonitrile-activated PS-*b*-PAEFc films with cylindrical and spherical PAEFc microdomains could be used as electrochemically responsive heterogenous catalysts for Michael addition reaction in $NaPF_6$/ethanol. We found that the reaction selectivity was controlled by permeability of the reactants into redox-inactive PS matrix, and the overall reaction yield was not affected by microdomain morphology.

In **Chapter 5**, we studied the diffusion behavior of three differently charged dye molecules within self-assembled asymmetric ONTs (NH_2-ONT_{10nm}) in pH 3.4 – 8.4 PBS solutions having ionic strength of 1.60 – 500 mM. These bolaamphiphilic ONTs had glucose and amine groups on the exterior and interior surfaces, an inner diameter of 10 nm, a wall thickness of 3.5 nm and lengths of 1 – 5 μm. A laser-based, wide-field fluorescence microscope was used to collect fluorescence videos for imaging FCS measurements. Autocorrelation and subsequent theoretical fitting of the data at each pixel across an ONT yielded local diffusion coefficient (D_{local}). D_{local} values from the multiple pixels were later averaged to calculate overall D_{ONT} for each ONT.

D_{ONT} values from multiple ONTs were compiled to assess the effects of pH and ionic strength on molecular diffusion behavior. pH effects on *D* showed that electrostatic interaction between the dye molecules and ONT inner surface plays an important role in determining molecular diffusion behavior: Electrostatic attraction between cationic ONT inner surface and anionic SRB resulted in a decrease in *D*, while electrostatic repulsion for zwitterionic/cationic RB or cationic R123 with the protonated amine-terminated surface increased *D*. However, the effects of ionic strength on *D* were negligible possibly due to the involvement of other non-coulombic interactions in the molecular diffusion.

In **Chapter 6**, we further investigated the effects of surface charge and inner diameter on the diffusion behavior of SRB, RB and R123 molecules using ONTs with inner carboxyl groups, COOH-ONT_{10nm} and COOH-ONT_{20nm}. As with **Chapter 5**, imaging FCS measurements were carried out in pH 3.4 – 8.4 PBS solutions having different ionic strengths (1.60 – 500 mM). As with NH_2-ONT_{10nm} in **Chapter 5**, ONT length gave no influence on the D_{ONT} of molecules studied. Inner diameters of the carboxyl-terminated ONTs (10 and 20 nm) gave no significant effect on the molecular diffusion. Anionic SRB showed a decrease in *D* with decreasing pH due to the reduced electrostatic repulsion as a result of the protonation of the surface carboxyl groups. Ionic strength did not affect *D* except 160 mM. Zwitterionic RB, in contrast, showed similar *D* at pH 3.4 – 8.4 for COOH-ONT_{10nm} and COOH-ONT_{20nm} because either dye molecule or ONT surface was uncharged in the solutions examined. Indeed, ionic strength gave no influence on *D*. R123 showed similar *D* at most of the solution conditions except acidic pH in COOH-ONT_{10nm}. R123 showed a slight increase in *D* at higher ionic strength, which might be due to the weakening of the electrostatic interactions as a result of charge screening.

Unfortunately, we did not have enough data for R123 in COOH-ONT$_{10nm}$ and COOH-ONT$_{20nm}$, and thus we could not discuss its diffusion in these ONTs.

This dissertation discussed charge transport behavior in nanostructures self-assembled from redox diblock copolymers (**Chapters 3** and **4**) and molecular diffusion behavior within nanostructures self-assembled from asymmetric bolaamphiphiles (**Chapters 5** and **6**). In the former, the charge transport properties of the redox-active nanostructures were assessed using electrochemical methods in TBAPF$_6$/acetonitrile and NaPF$_6$/ethanol and provided a means for a catalysis application. One major problem with this study is that we did not perform any annealing processes for the thin films, and thus the order and orientation of the microdomains may not be good enough to extract the intrinsic charge transport properties of the microdomains. In addition, a planar gold electrode is not ideal for efficient catalytic reaction due to the limited electrode area. The use of a porous electrode as a support of a PS-*b*-PAFEc film will accelerate the catalytic reaction. In the future, a myriad of redox BCPs will be examined for various applications through a collaboration between polymer scientists and electrochemists. In the latter regarding the ONT projects, we could not conclude the actual locations of the dye molecules in ONTs: The dyes may be adsorbed on the outer surface or on the inner surface, or incorporated in the wall, though we could infer that the dyes were mainly near the inner surface from the significant influences of electrostatic interactions. In addition, the limited spatial resolution of the fluorescence microscopic method hindered us from accurately differentiating between a single ONT or a bundle of ONTs. These problems may be solved through the advancement of optical microscopic techniques in the future. Lastly, although imaging FCS is a convenient tool to measure relatively slow diffusion of fluorescent species, this method cannot measure fast diffusion (e.g., > 3 $\mu m^2/s$) due to the limited temporal resolution of the emCCD detector. Future

development of a more sensitive camera will improve the time resolution, and thus will permit the measurements of faster diffusion.